Doctorate Dissertation
博士論文

A spectroscopic study of 229-Th isomer using TES microcalorimeters
（229-Th異性体のTESマイクロカロリメータを用いた分光研究）

A Dissertation Submitted for Degree of Doctor of Philosophy
December 2018

平成 30 年 12 月 博士（理学）申請

Department of Physics, Graduate School of Science,
The University of Tokyo

東京大学大学院 理学系研究科 物理学専攻

Haruka Muramatsu
村松　はるか

Acknowledgments

I have been supported by many people during my 5 years. Without their help, I would never be able to finish my long journey of my thesis.

I am deeply grateful to my advisor Prof. Kazuhisa Mitsuda. He has patiently guided me throughout the journey of my thesis with his depth and breadth of knowledge. I would like to thank Prof. Noriko Y. Yamasaki for her support and encouragement.

I would like to express my gratitude to TES-Thorium projects members, Dr. Atsushi Yamaguchi, Dr. Keisuke Nakamura, Dr. Hidetoshi Kikunaga, Misaki Takimoto, Associate Prof. Keisuke Maehata for valuable comments and support. SQUIDs used in this thesis were fabricated in the CRAVITY at AIST with a great help from Dr. Mutsuo Hidaka, Dr. Shuichi Nagasawa, and Dr. Satoshi Kohjiro. I received generous support at Tohoku University from Dr. Kenji Shirasaki.

Dr. Kazuhiro Sakai taught me all about SQUID and analysis methods of TES waveforms. Without his analysis-program, I could never be able to establish the TES analysis methods. Kenichiro Nagayoshi taught me all about TES fabrication process. Dr. Tasuku Hayashi helped me to conduct the entire research in this thesis and gave me constructive comments. Without his help, I could never be able to finish my thesis. I would also like to thank Keisei Maehisa, Ryouhei Konno, Takehiro Kuroiwa, Dr. Kumi Ishikawa for helping TES fabrication. I would also like to express the deepest appreciation to Naoki Yuasa from Kyshu University for helping all experiments at Tohoku University. A special thanks to my fellow labmates: Dr. Norio Sekiya, Dr. Ryo Yamamoto, Dr. Takahiro Kikuchi, Akira Chiba, Masatoshi Hoshino, Yuki Tsurugasaki, Yuki Nakashima, Takahiro Nakayama, Ryota Takaku, Dr. Tomotake Matsumura, Dr. Shu Koyama, Dr. Hiroaki Imada. I owe my deepest gratitude to Secretary AkikoYokoyama and Noriko Takahashi for all about the daily life in the lab.

Last but not least, I would like to offer my special thanks to my family. I am grateful to my mother and father for their support and encouragement.

Abstract

^{229}Th is believed to have the lowest nuclear energy level at 20 eV or less. By utilizing this level, a nuclear clock may be realized. Furthermore, using this clock, we may be able to obtain the strongest constraint on the time variation of the fine structure constant.

X/γ-ray spectrometer systems were developed for the study of the ^{229}Th isomeric state. Searching for temporal variations of the physical constants is an important subject even nowadays, and measuring the temporal variation of the fine structure constant using a ^{229}Th nuclear clock is belived to achive the highest sensitivity among other searches. For this purpose, first we need to determine the lowest-energy of the ^{229}Th isometric state, which is considered to be the lowest nuclear energy level among all nuclei. One of the methods used to measure the energy level is utilizing the energy difference between decay from 29.19 keV to the isometric state and to the ground state. In this thesis, we developed a high-energy resolution γ-ray measurement using transition edge sensor (TES) microcalorimeters. Our goals for this development are an FWHM energy resolution of about 15 eV at 29 keV, and statistical errors of below 0.5 eV and an estimation of the systematic error exactly. Because of the non-linear energy response of TES microcalorimeters, energy resolution degrades with increasing energy. Thus, these goals are challenging. First, we studied the energy-scale calibration method and developed a new analysis method to improve the energy-scale determination. We used a model fitting where we determined the local energy scale and the energy of the line complex containing fine structures at the same time utilizing the line emission model of the line complex. We also converted current pulses to resistance pulses to improve the non-linear response. With this method, the systematic error for determination of the energy became less than 2 eV.

We developed the detector system and the energy resolution was 20 eV at 26 keV in our laboratory environment. When this was deployed to the site where a ^{233}U source was available, the energy resolution degraded to 40 eV at 26 keV, because of the thermal fluctuation noise induced by γ-ray hits on the Si substrate of the detector. The 29.19 keV line was not separated into a doublet. However, we estimated the energy level using multiple lines from ^{229}Th thorugh resistance pulse analysis -- $E(^{229\mathrm{m}}\mathrm{Th}) = 8.4^{+7.2}_{-5.8} \pm 9.5$ eV – with the statistical error and the systematic error. From this experiment we found that we need to improve the energy resolution of the device, develop a collimator, and place calibration sources close to our target lines.

We then developed the improved detector system. We tried to improve the energy resolution by setting the superconducting temperature of the TES lower. We designed and fabricated a collimator tha blocks γ-rays hitting the Si substrate. We deployed the new detector system to the ^{233}U experiment site. We confirmed an energy resolution of 15-18 eV at 26 keV and a reduction of the thermal fluctuation noise. We also set up new calibration sources using three new materials. Finally we estimated whether we could separate 29.19 keV lines into a doublet with the 18 eV energy resolution.

Contents

List of Figures

List of Tables

Chapter 1

Introduction

In general relativity, the time and space variations of the physical constant are impermissible according to Einstein's equivalence principle because the result of the local non gravitational experiment is unrelated to where and when it was conducted. On the other hand, for example a unified theory, such as M-theory gives no limitation to the time and space variations of the physical constant. The search for the variations of the physical constant is an important subject of study. The fine structure constant, which expresses the interaction between the electromagnetic field and the electric charge, is the one of the physical constants that is indicated to be time variation and the possibility of time variation has been verified by several experiments. One of the improving methods for the time verification is to comparing the frequency of a Thorium nuclear clock which has high sensitivity to the time variation and a different type of atomic clock which has low sensitivity to the time variation over a certain period. A thorium nuclear clock is a laser frequency standard that references the lowest-energy of the ^{229}Th isomeric state. A thorium atomic clock has never put into practice because the exact energy of the ^{229}Th isomeric state has not been obtained. The difference between the ground state and the isomeric state decay from 29.19 keV, lowest-energy of ^{229}Th isomeric state, is widely known to be around 10 eV.

We have started the TES-thorium project to measure the lowest-energy of ^{229}Th isomeric state thorugh γ-ray spectroscopic using a TES microcalorimeter. We set the energy resolution about 15 eV, statistical errors of below 0.5 eV and an estimation of the systematic error exactly. To the non-linear response to energy of the TES device and use the calibration source within fine structures, it is difficult to calibrate the energy. We developed a new analysis method to improve energy-scale determination.

We conducted the lowest-energy of the ^{229}Th isomeric state at JAEA in Oarai using the TES device which energy resolution was 20 eV at 26 keV in our laboratory. However with the ^{233}U source, because of the thermal fluctuation of the deveic, the low-frequency noise got worse, and the energy resolution also got worse up to 40 eV at 26 keV. We found that the systematic error for determing of the energy was uncertain because of the absence of calibration lines close to our target line.

To solve these problems, we designed and fabricated a collimator and added calibration lines close to our target lines. We also improved the energy resolution of the detector itself. We evaluated the performance of the device and the collimator in the ^{233}U radiation environment and confirmed 15-18 eV energy resolution at 26 keV.

In Chapter 2 of thes thesis, we review how the time variation of the fine structure constant is measured, what are the past measurements, and what are the results of the lowest-energy of the ^{229}Th isomeric state. We determine the existing range of the lowest-energy of the ^{229}Th isomeric state. In Chapter 3, we describe the required detector to measure the lowest-energy of the ^{229}Th isomeric state, and in Chapter 4 we review TES microcalorimeters and its read out system. In Chapter 5, we devise a new calibration method by considering the non-linear response and the fine structure and verify this method using the experimental data. In Chapter 6, the lowest-energy of ^{229}Th isomeric state measurement was performed with a ^{233}U using the TES device which was designed and fabricated using the in-house process. From this measurements, we find some issues. Chapter 7

explains how we improve these issues and describe the performance of the device and the collimator. In Chapter 8, we decide how to add the calibration lines and estimate whether we can separate the 29.19 keV doublet using the results of Chapter 7. Finally we conclude our results in Chapter 9.

Chapter 2

Review of Time Variation of Fine Structure Constant

2.1 Time Variation of Fine Structure Constant and Methods of Searching Variation

Physics basically assumes physical constants never change. The constants such as the velocity of light, c, Planck constant, h, and the elementary charge, e are assumed to be the same at any places and times in the universe. In SI units, c is 2.99792458×10^8, h is $6.62606957 \times 10^{-34}$, and e is $1.602176565 \times 10^{-19}$. First of all, Dirac challenged this assumption that these parameters are constant, and he suggested that G might vary as t^{-1} with the cosmic time [9]. However, no evidence that the constants have time-dependence term. The last two decades, M-theory was proposed by Edward Witten[10] and became the leading candidate for theory of everything. The M-theory is mother of all string theories and is self-consistent if the universe has seven more dimensions in addition to four dimensions of space and time. The truly fundamental constants are in the higher-dimensional space, and we observe their three-dimensional shadows. If the size of extra dimensions of space become large/small, the constants that we observe in our three-dimensional space would change with them. The best constants to search for the variations are dimensionless quantities. The famous quantity, $\alpha = e^2/\hbar c$, called the fine structure constant is one of such quantities. The value of α is related to the interaction between electromagnetic field and electric charge. The time and spacial variations of α have been searched for several measurements.

2.1.1 Oklo Phenomenon

A constraint on time variations of the fine structure constant was obtained from the cross section of Sm nucleus reactions[11]. Oklo is a natural fission reactor that was operated two billion years ago. From measured Sm isotopic abundances at Oklo, researchers could calculate the cross section of ^{149}Sm and relate it to the energy of the resonance. By ^{149}Sm, thermal neutron is captured

$$n + {}^{149}_{62}\text{Sm} \rightarrow {}^{150}_{62}\text{Sm} + \gamma, \tag{2.1}$$

and the cross section depends on capture resonance of a neutron energy (E_r)[11]. The effective absorption-cross-section is defined by

$$\hat{\sigma}(E_\text{r}, T) = \frac{1}{v_0} \frac{2}{\sqrt{\pi}} \int \sigma_{(n,\gamma)}(E) \sqrt{\frac{2E}{m_\text{n}}} \frac{e^{-E/k_\text{B}T}}{(k_\text{B}T)^{3/2}} \sqrt{E} dE, \tag{2.2}$$

where the velocity $v_0 = 2200$ m/s relates to the energy of $E_0 = 25.3$meV and $\sigma_{(n,\gamma)}(E)$ is the cross section of the neutron capture Equation (2.1),

$$\sigma_{(n,\gamma)}(E) = \frac{g_0 \pi}{2} \frac{\hbar^2}{m_n E} \frac{\Gamma_n \Gamma_\gamma}{(E - E_r)^2 + \Gamma^2/4}, \tag{2.3}$$

where $g_0 = 9/16$ and $\Gamma \equiv \Gamma_n + \Gamma_\gamma$ is the total width of the neutron partial width Γ_n and of the radiative partial width Γ_γ, the values respectively 0.533 meV and 60.5 meV. The neutron flux is expressed as

$$\hat{\phi} = v_0 \frac{2}{\sqrt{\pi}} \int \sqrt{\frac{2E}{m_n}} \frac{e^{-E/k_B T}}{(k_B T)^{3/2}} \sqrt{E} dE. \tag{2.4}$$

The time dependencies of the number densities N_{147}, N_{148}, N_{149}, and N_{235} of $^{147}_{62}$Sm, $^{148}_{62}$Sm, $^{149}_{62}$Sm, and $^{235}_{92}$Sm is calculated by [12, 13]

$$\frac{dN_{147}}{dt} = -\hat{\sigma}_{147}\hat{\phi}N_{147} + \hat{\sigma}_{235}\hat{\phi}N_{235}, \tag{2.5}$$

$$\frac{dN_{148}}{dt} = \hat{\sigma}_{147}\hat{\phi}N_{147}, \tag{2.6}$$

$$\frac{dN_{149}}{dt} = -\hat{\sigma}_{149}\hat{\phi}N_{149} + \hat{\sigma}_{235}\hat{\phi}N_{235}, \tag{2.7}$$

$$\frac{dN_{235}}{dt} = \sigma_{235}(1 - C)N_{235}. \tag{2.8}$$

Using these equations(Equation (2.5), (2.6), (2.7), (2.8)), assuming that the cross section was constant during the Oklo phenomenon, researchers obtained the cross section of $\hat{\sigma}_{149}$ by comparing the results of natural abundances of the samarium. By estimating the neutron temperature and Equation 2.3, researchers transformed the cross section into the resonance energy E_r. According to a phenomenological Bethe-Weisasäcker formula, the relation between the resonance energy and fine structure was

$$\alpha \frac{\Delta E_r}{\Delta \alpha} \simeq -1.1 \text{ MeV}, \tag{2.9}$$

and researchers calculated the variation of the fine structure constant. An uncertainies of the observation gave an upper limit of the $\hat{\sigma}_{149}$ time variation. Shlyakhter calculated that and obtained $|\dot{\alpha}/\alpha| \lesssim 10^{-17} y^{-1}$[11]. Damour and Dyson [12] reanalyzed samples and reported an upper bound $|\dot{\alpha}/\alpha| \lesssim 5 \times 10^{-17} y^{-1}$. In 2000, Fujii et al.[13] analyzed the data and reached the result of $|\dot{\alpha}/\alpha| \lesssim -(0.2 + 0.8) \times 10^{-17} y^{-1}$. S.K.Lamoreaux [14] also analyzed the data by not using Boltzmann distribution and reached

$$\dot{\alpha}/\alpha = -2.3^{+0.8}_{-0.4} \times 10^{-17} \ y^{-1}. \tag{2.10}$$

2.1.2   Astrophysical Observations

Another way of searching time variation of the fine structure constant is to use absorption lines from the quasar. The quasar is a bright source and the light from the quasar is absorbed by clouds which exists between the quasar and earth. The absorption lines features reflect the chemical abundance of the clouds. The relative line splitting $\delta\lambda/\lambda$ in a doublet absorption ($S_{1/2} \to P_{3/2}$ and $S_{1/2} \to P_{1/2}$) relates to the fine structure and the the energy

splitting δE by the spin-orbit coupling is

$$\delta E \propto \frac{e^2}{m^2 r^3} \mathbf{S} \cdot \mathbf{L} \propto me^8. \tag{2.11}$$

This energy splitting is proportional to the second power of the fine structure constant as $\delta E/E \propto \delta\lambda/\lambda \propto \alpha^2$. Thus, one can search for the time variations of the fine structure constant by measuring relative line splitting and comparing that value to laboratory value. In 1994, Potekhin and Varshalovich studied alkali like atoms absorption lines at $z \sim 3.2$ and compared the wavelengths in laboratory [15]. They obtained

$$\Delta\alpha/\alpha = (2.1 \pm 2.3) \times 10^{-3}, \tag{2.12}$$

from C IV, N V, O VI, Mg II, Al III and Si IV absorption doublets. Si IV is the most sensitive one for a change in fine structure constant. In 1995, Potekhin et al.[15] calculated uncertainty of the fine structure constant using Si IV doublet with redshift $3.0 < z < 3.7$ and obtained the uncertainty at $z = 3.2$

$$\Delta\alpha/\alpha = (2 \pm 7) \times 10^{-5}. \tag{2.13}$$

In [16, 17], Murphy observed Si IV doublet in eight quasars with Keck/HIRES with redshift $z = 2 \sim 3$ and they reported that

$$\Delta\alpha/\alpha = (-0.543 \pm 0.116) \times 10^{-5}. \tag{2.14}$$

They measured the absorption lines at several redshift and obtained the relation between $\Delta\alpha/\alpha$ and z_{abs}, cosmological time. They model fit the $\frac{d\alpha}{dz}\frac{1}{\alpha}$ with fit $\Delta\alpha/\alpha = 0$ at $z_{\mathrm{abs}} = 0$ and the variation for redshift $(d\alpha/dz)/\alpha = (-0.357 \pm 0.079) \times 10^{-5}$. To obtain the time variation of the fine structure constant, they calculated fractional look-back time and fitted the relation of $\Delta\alpha/\alpha$ and the time and deduced as

$$\dot{\alpha}/\alpha = (6.40 \pm 1.35) \times 10^{-16} \text{ yr}^{-1}. \tag{2.15}$$

In those measurements absorption lines of different elements were compared, assuming that all atomic energy levels are affected by time variation of the fine structure constant in the same manners. In this observation, there are several issues to be considered. For example, when one compares wavelengths with different atoms, they have to consider that the velocity difference in the different areas where the atoms are located. It occurs the difference of Doppler redshift. One gives attention to the the presence of a magnetic field which shifts the transition energy by Zeeman effect. One also searches temperature variations during the observation.

2.1.3   Comparison Two Atomic Transition Frequencies

The measurement based on the compression of different atomic clocks is a model independent without any assumptions on variability of other parameters in contrast with astrophysical observations. The electronic transition frequency is shown as

$$f = \mathrm{Ry} \cdot \mathrm{C} \cdot F(\alpha), \tag{2.16}$$

by E.Peik, et al.[1]. Where $\mathrm{Ry} = m_e e^4/(8\epsilon_0^2 h^3) \simeq 3.2898 \times 10^{15}$ Hz is the Rydberg constant, m_e is the electron mass, e is the elementary charge, ϵ_0 is the electric constant, and h is the Planck's constant. In Equation (2.16), C is the numerical constant depending on the quantum numbers and $F(\alpha)$ is the factor that depends on the
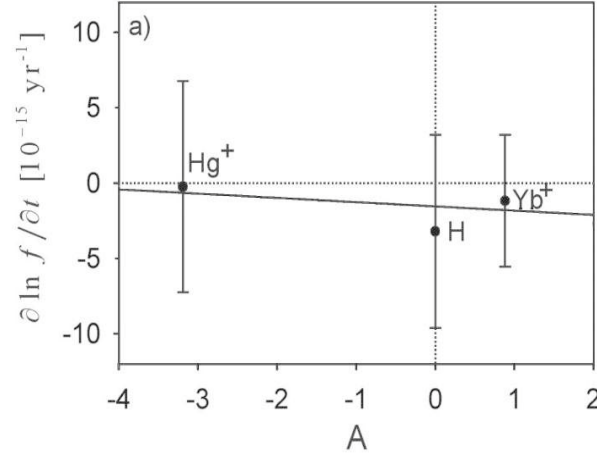
Fig. 2.1   Relative frequency variation and the sensitivity A in the Hg^+ and Yb^+ ions. The solid lines is fitting result and the slope is a time deviation of fine structure [1].

fine structure constant. Atoms with a high atomic number have different sensitivities for each of the transition frequencies and especially heavier atoms have strong dependence. The time derivative of the frequency is expressed as

$$\frac{\partial \ln f}{\partial t} = \frac{\partial \ln Ry}{\partial t} + A\frac{\partial \ln \alpha}{\partial t} \quad A = \frac{\partial \ln F}{\partial \ln \alpha}, \tag{2.17}$$

where $\partial \ln Ry/\partial t$ is the variation rate of the Rydberg constant and would be common to all transition frequencies. The second term in Equation (2.17), A, is the sensitivity factor for the change and was calculated in several cases by Dzuba et al. [18, 19]. Assuming that the drifts of atomic frequencies changed linearly with time over the period, they calculated $\partial \ln \alpha/\partial t$ by using two measured time derivative of frequencies $\partial \ln f/\partial t$. The time derivative of $\partial \ln \alpha/\partial t$ was obtained by the slope of $\partial \ln f/\partial t$ function which is proportional to the sensitivity A. E.Peik [1] measured an optical transition frequency in $^{171}Yb^+$ using cesium atomic clock twice with a interval of 2.8 year. They obtained the variation of the frequency $f_{Yb}/f_{cs} = (-1.2 \pm 4.4) \times 10^{-15}$ yr^{-1}. They combined the measured $^{171}Yb^+$ data and the time derivative of $^{199}Hg^+$ [20] with variation of $f_{Hg}/f_{Cs} = 7 \times 10^{-15}$ yr^{-1}. From the sensitivity of the change, $A_{Yb} = 0.88$ and $A_{Hg} = -3.19$ [18], they plotted the $\partial \ln f/\partial t$ as a function of A and computed the slope by fitting with a linear function (Figure 2.1) with 1σ level confidence

$$\frac{\partial \ln \alpha}{\partial t} = \frac{\dot{\alpha}}{\alpha} = (-0.3 \pm 2.0) \times 10^{-15} \text{ yr}^{-1}. \tag{2.18}$$

M.Fischer measured the transition frequency f_H in hydrogen atom and calculated the ration of $f_{Cs}/f_H = (3.2 \pm 6.3) \times 10^{-15}$ yr^{-1} [21]. Also they used the ration $f_{Cs}/f_{Hg} = (0.2 \pm 7) \times 10^{-15}$ yr^{-1} obtained by[20]. Using both results, they obtained the limits of fine structure constant drift

$$\frac{\dot{\alpha}}{\alpha} = (-0.9 \pm 2.9) \times 10^{-15} \text{ yr}^{-1}. \tag{2.19}$$

In another experiment, S.Blatt et al.[22] measured the doubly forbidden ^{87}Sr using ^{87}Sr optical lattice clock and obtained the derivation of fine structure constant by using ^{87}Sr frequency and $^{199}Hg^+$ frequency. They reported the drift rate as

$$\frac{\dot{\alpha}}{\alpha} = (-3.3 \pm 3.0) \times 10^{-16} \text{ yr}^{-1}. \tag{2.20}$$

2.1.4 ^{229}Th Nuclear Clock

From the results of Oklo phenomena and the quasar observation, the time variation of the fine structure constant was suggested while the results of comparison two atomic transition frequencies did not suggest the time variation of the fine structure constant. In order to search the time variation of the fine structure constant with higher sensitivity, comparison of the frequency of ^{229}Th nuclear clock and other atomic clock was suggested [23, 24]. Xiao-tao He [24] calculated the sensitivity to variation of the fine structure constant considering the correlation between the nuclear strong interaction and the Coulomb force in the relativistic filed theory. The time variation of transition frequency is expressed by the Feynman-Hellmann theorem [25]

$$\dot{\omega} = \sum \left(<f|\frac{\partial H}{\partial \lambda_i}|f> - <g.s.|\frac{\partial H}{\partial \lambda_i}|g.s.> \right) \dot{\lambda}_i, \tag{2.21}$$

where the $|f>$ expresses the excited state, $|g.s.>$ expresses the ground state, and λ_I is the dynamical constants. The nuclear Hamiltonian is defined as

$$H = H_\mathrm{n} + V_c, \tag{2.22}$$

where, H_n represents both the kinetic energy and the nuclear strong interaction and V_c is the Coulomb potential. The relative variation of transition frequency is obtained by using the fact that there is a linear relation between the Coulomb potential and the fine structure constant [12, 25]

$$\dot{\omega} = \ll V_\mathrm{c} \gg \frac{\dot{\alpha}}{\alpha} = (<f|V_\mathrm{c}|f> - <g.s.|V_\mathrm{c}|g.s.>) \frac{\dot{\alpha}}{\alpha}. \tag{2.23}$$

Therefore, the variation of the fine structure constant is related to the frequency variation using the difference of the Coulomb force between two states. Namely,

$$\frac{\dot{\omega}}{\omega} = \left[\frac{\ll V_c \gg}{\omega} \right] \frac{\dot{\alpha}}{\alpha}. \tag{2.24}$$

The sensitivity factor $\kappa_\alpha = \ll V_c \gg /\omega$ depends on the Coulomb-energies-difference and transition frequency. Xiao-tao He et al. calculated the Coulomb energies of ^{229}Th isomer and its ground state by relative field theory and the results was $\ll V_\mathrm{c} \gg \approx -0.698$ MeV [24]. Then, the sensitivity factor is $\kappa_\alpha = \ll V_c \gg /\omega \approx -9.184 \times 10^4$. Here they assumed the lowest-energy of ^{229}Th isomeric state as to be 7.6 ± 0.5 eV [3]. They obtained by about five orders of magnitude enhancement of the sensitivity due to low transition frequency of the ^{229}Th isomeric state.

2.2 Nuclear Structure of ^{229}Th and Methods to Obtain Lowest-energy of ^{229}Th Isomeric State

^{229}Th is produced by α-decay of ^{233}U with the probability, P_α (Table 2.1). A part of the level scheme of ^{229}Th is shown in Figure 2.4. Decay of ^{229}Th occurs by internal conversion (IC) with emission of an electron and γ-ray transition with emission of a phonon. From [26] with γ-ray spectroscopy, the intensity of γ-ray transition I_γ and the conversion coefficient P_e/P_γ (P_e:the probability of internal conversion, P_γ:the probability of γ-ray transition) is given and sum of branching ration $K = P_\gamma + P_\mathrm{e}$ is calculated these values (Table 2.2). Since the lowest-energy of ^{229}Th isomeric state, $E(^{229\mathrm{m}}\mathrm{Th})$, is below 10 eV, the measurement of [26] could not separate two lines of 97.13 keV
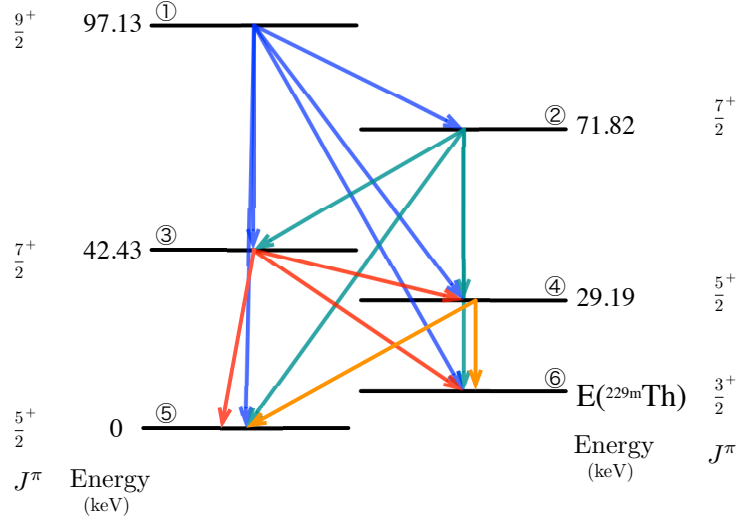
Fig. 2.2   Decay chain of ^{229}Th under 97.13 keV

Table 2.1   Branching rations for α-decay of ^{233}U

	Energy (keV)	Branching rations P_α(%)
①	97.13	1.61
②	71.82	0.163
③	42.43	13
④	29.19	0.28
⑤	0	84

Table 2.2   Internal conversion coefficient and branching rations for each decay channel of ^{229}Th: I_γ is the intensity of γ-ray transition [26], P_e/P_γ is the internal conversion coefficient[27], P_γ and $K = P_\gamma + P_e$ are calculated values (P_γ: a probability of γ-ray transition, P_e : a probability of internal conversion)

	$E_i - E_f$ (keV)	Energy (keV)	I_γ	P_e/P_γ	P_γ	$K = P_\gamma + P_e$
① → ②	97.13–71.82	25.31	2.11	227	0.053	0.278
① → ③	97.13–42.43	54.70	16.8	55	0.425	0.543
① → ④	97.13–29.19	67.94	0.320	71.6	0.008	0.013
① → ⑤	97.13–0	97.13	20.3	13.2	0.514	0.166
① → ⑥	97.13-$E(^{229m}$Th)					
② → ③	71.82–42.43	29.39	0.80	149	0.047	0.12
② → ④	71.82–29.19	42.63	13.2	58	0.78	0.779
② → ⑤	71.82-0	71.82	1.16[1,2]	13.1	0.07	0.987
② → ⑥	71.82—$E(^{229m}$Th)		1.81[1,2]	54.9	0.11	0.102
③ → ④	42.43–29.19	13.24	2.4	380	0.031	0.082
③ → ⑤	42.43–0	42.43	72	140	0.97	0.907
③ → ⑥	42.43—$E(^{229m}$Th)		0.18[1]	694	0.02	0.011
④ → ⑤	29.19–0	29.19	2.7[1]	149	0.26	0.18
④ → ⑥	29.19—$E(^{229m}$Th)		7.8	235	0.74	0.819

[1]Calculated from strong coupling rotational model [2]Calculated from intensity balance

Table 2.3   Decay probability with γ-ray emission of ^{229}Th lines when the isomer ^{229m}Th is not separated and separated

| | Energy (keV) | Decay probability with γ-ray emission | |
		no separation of the doublets	separation of the doublets
④ → ⑤	29.19	6.69×10^{-5}	5.58×10^{-6}
④ → ⑥	29.19—$E(^{229m}$Th$)$		6.69×10^{-5}
② → ③	29.39	4.91×10^{-6}	4.91×10^{-6}
③ → ⑤	42.43	9.02×10^{-4}	9.02×10^{-4}
③ → ⑥	42.43—$E(^{229m}$Th$)$		1.84×10^{-5}
② → ④	42.63	8.20×10^{-5}	8.20×10^{-5}
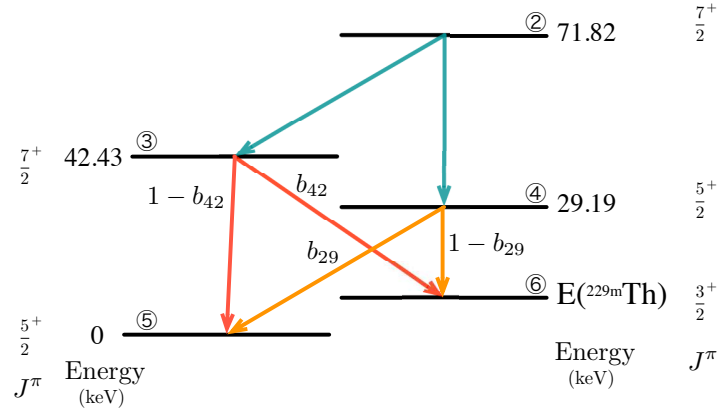
Fig. 2.3   Specific decay scheme of ^{229}Th that is used to calculate the isometric energy ^{229m}Th

to isomer and ground state, of 71.82 keV to isomer and ground state, of 42.43 keV to isomer and to ground state and, of 29.19 keV to isomer and to ground state. In Table 2.2,the values with indices, 1 and 2, are calculated from strong coupling rotational model and intensity balance, respectively. When we calculated the decay probability with 29.19 keV and 29.19 keV $- E(^{229m}$Th$)$ and with 42.43 keV and 42.43 keV $- E(^{229m}$Th$)$, we obtained the total decay probability of 29.19 keVand 29.19 keV $- E(^{229m}$Th$)$, 42.43 keV and 42.43 keV $- E(^{229m}$Th$)$. Then, we calculated the decay probability with γ-ray emission of 29.19, 29.39, 42.43, 42.63 keV. For example, we calculated the intensity of 29.39 keV. In this case, there are two decay paths to radiate 29.39 keV, (1) α-decay of ^{233}U to 71.82 keV and decay to 42.43 keV, (2) α-decay of ^{233}U to 97.13 keV and decay to 71.82 keV and decay to 42.43 keV. The probability in case (1) is calculated by $P_\alpha(②) \times K(② → ③) = 1.96 \times 10^{-4}$ and the probability in case (2) is calculated by $P_\alpha(①) \times K(① → ②) \times K(② → ③) = 5.37 \times 10^{-4}$. Sum of the decay probability with γ-ray emission of 29.39 keV is $(1.96 \times 10^{-4} + 5.37 \times 10^{-4})/(P_e/P_\gamma) = 4.91 \times 10^{-6}$. Another lines were calculated using the same way. From [3, 28], the branching ration b_{29} of 29.19 keV to ground state (④ → ⑤) is 1/13 and the branching ration b_{42} of 42.43 keV to isomer state (③ → ⑥) is 1/50, so we calculated the each decay probability including a doublet of 29.19 keV and 42.43 keV in Table 2.3. In one of the indirect method to obtain the isomer energy ^{229m}Th using the 5 every levels Figure 2.3, we can calculate the $E(^{229m}$Th$)$ as

$$E(^{229m}\text{Th}) = E(② → ③) + E(③ → ⑤) - E(② → ④) - E(④ → ⑥). \tag{2.25}$$

Measured energy $E'(③ → ⑤, ③ → ⑥)$ includes $E(③ → ⑤)$ and $E(③ → ⑥)$ with branching ration $1 - b_{42}$ to b_{42} since we can not separate these lines, we express $E'(③ → ⑤, ③ → ⑥)$ using a weighted averaging to $E(③ → ⑤)$ and $E(③ → ⑥)$

$$E'(③ → ⑤, ③ → ⑥) = E(③ → ⑤) - b_{42} \cdot E(^{229m}\text{Th}). \tag{2.26}$$
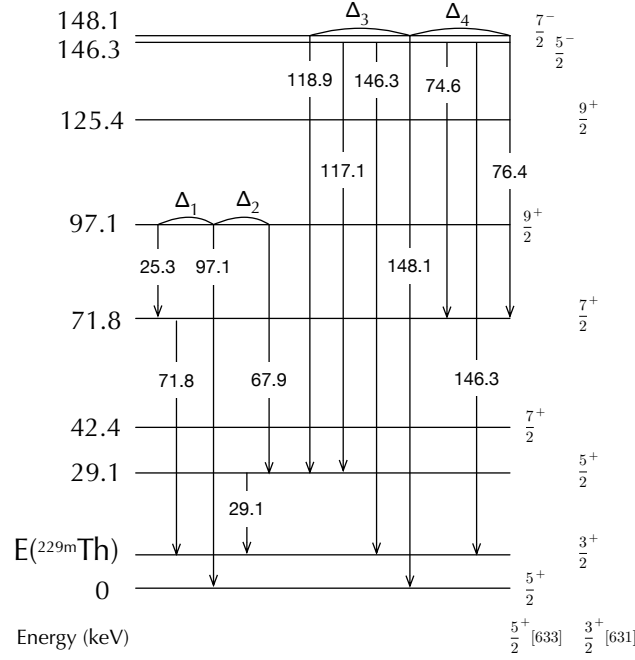
Fig. 2.4　γ-ray transitions in ^{229}Th used to calculate the isomeric energy of ^{229}Th [2]

$E'(④ \to ⑥, ④ \to ⑤)$ is also expressed using a weighted averaging to $E(④ \to ⑤)$ and $E(④ \to ⑥)$ and branching ration b_{29},

$$E'(④ \to ⑥, ④ \to ⑤) = E(④ \to ⑥) + b_{29} \cdot E(^{229m}\text{Th}). \tag{2.27}$$

$E(^{229m}\text{Th})$ is calculated by substituting Equation (2.26) and (2.27) for Equation (2.25),

$$E(^{229m}\text{Th}) = \frac{[E(② \to ③) - E'(④ \to ⑥, ④ \to ⑤)] - [E(② \to ④) - E'(③ \to ⑤, ③ \to ⑥)]}{1 - b_{42} - b_{29}} \tag{2.28}$$

where, both E and E' use the values obtained from the measurement. On the other hand, there is a direct measurement to estimate the lowest-energy of ^{229}Thisomeric state by detecting and separating two lines of 29.19 keV. In this case, the difference of these two lines gives an estimate of that energy level:

$$E(^{229m}\text{Th}) = E(④ \to ⑤) - E(④ \to ⑥). \tag{2.29}$$

2.3　Past Measurements of Lowest-energy of ^{229}Th Isomeric State

There are two ways to obtain the lowest energy of ^{229}Th isomeric state, indirect measurement and direct measurement. We explain the several past measurements in those two ways.

2.3.1　γ-ray Spectroscopies with Conventional Detectors and Microcalorimeters

In 1976, Kroger and Reich suggested that ^{229}Th had a lowest lying excited state below 100 eV above the ground state [29]. They studied the γ-ray of ^{229}Th from the alpha decay of ^{233}U with Ge and Si detectors and reported that there are specific energy and parity of emission lines not compatible with the known rotational band of the
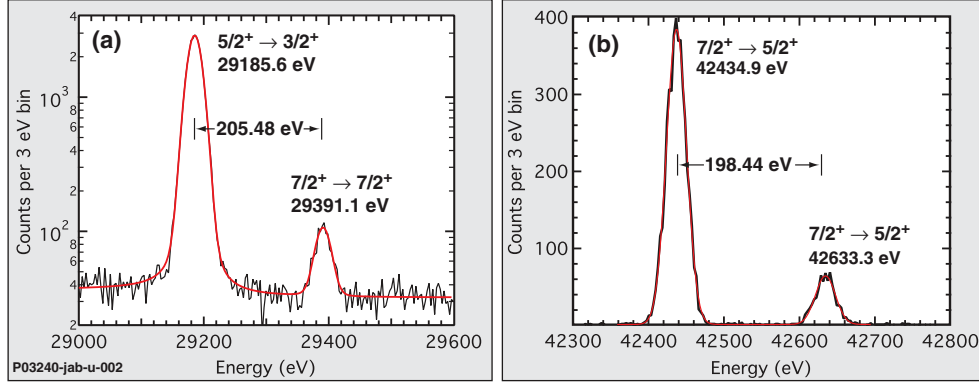
Fig. 2.5   Energy spectra of 29 keV and 42 keV obtained by X-ray spectrometer[3]

^{229}Th atom. They deduced the band of the isomeric state was $j^{\pi} = \frac{3^{+}}{2}$ at the energy level of about 100 eV. Reich and Helmer measured multiple γ-rays emitting from the two excited state, 97.1 keV and 148.1 keV [2](Figure 2.4). They derived the energy $E(^{229\mathrm{m}}\mathrm{Th}) = -1 \pm 4$ eV with averaged these three difference

$$\Delta_1 = E(97.1 - 0) - E(71.8 - E(^{229\mathrm{m}}\mathrm{Th})) - E(97.1 - 71.8), \tag{2.30}$$

$$\Delta_2 = E(97.1 - 0) - E(97.1 - 29.1) - E(29.1 - E(^{229\mathrm{m}}\mathrm{Th})), \tag{2.31}$$

$$\Delta_3 = [E(148.1 - 0) - E(146.3 - E(^{229\mathrm{m}}\mathrm{Th}))] - [E(148.1 - 29.1) - E(146.3 - 29.1)]. \tag{2.32}$$

Where, $E(\#)$ is the energy of $\#$ emission level state, i.e., $E(97.1)$ is the energy of 97.1 keV. This was the first indirect measurement of the lowest lying excited state of ^{229}Th. Reich and Helmer improved the energy resolution of detectors by using HPGe and Si detectors and measured γ-rays of ^{229}Th in 1994 [30]. They calculated the isomeric state using the same scheme including additional lines

$$\Delta_4 = [E(148.1 - 0) - E(146.3 - E(^{229\mathrm{m}}\mathrm{Th}))] - [E(148.1 - 71.8) - E(146.3 - 71.8)], \tag{2.33}$$

and derived the result

$$E(^{229\mathrm{m}}\mathrm{Th}) = 3.5 \pm 1.0 \text{ eV}. \tag{2.34}$$

Guimarães-Filho and Helene[31]   reanalyzed the data from [30] including the branching rations and obtained

$$E(^{229\mathrm{m}}\mathrm{Th}) = 5.5 \pm 1.0 \text{ eV}. \tag{2.35}$$

In 2007, Beck et al.[3] measured 4 low level γ-rays using microcalorimeters with an energy resolution of 26 eV (FWHM) and determined the isomeric state. At first, they only considered the 29.19 keV doublet lines and they calculated $^{229\mathrm{m}}$Th by $E(^{229\mathrm{m}}\mathrm{Th}) = \frac{(E(②→③)-E'(④→⑥,④→⑤))-(E(②→④)-E'(③→⑤,③→⑥))}{1-b_{29}}$ with branching ration b of 29.19 keV doublet as $b_{29} = 1/13$ and the energy was

$$E(^{229\mathrm{m}}\mathrm{Th}) = 7.6 \pm 0.5 \text{ eV}. \tag{2.36}$$

They updated it with considering additional 42.43 keV doublet and the result [28] was

$$E(^{229\mathrm{m}}\mathrm{Th}) = 7.8 \pm 0.5 \text{ eV}. \tag{2.37}$$

In 2015, Justin Jeet et al.[4] measured the lowest-energy ^{229}Th isomeric transition by directly excited that isomeric state using the synchrotron radiation. They used LiSrAlF$_6$ crystals doped in ^{229}Th that are exposed with the Vacua-Ultraviolet (VUV) synchrotron radiation from 7.412 to 8.8 eV energy range with step size ≤ 0.1 eV. They scanned continuously within the energy range since the step size was set smaller the line width of VUV ($\hbar\Gamma \sim 0.19$ eV) . If the VUV photons area resonant with the lowest-energy ^{229}Th isomeric transition, the ground state of ^{229}Th is excited to the isomeric state and after a certain excitation period T_e, the VUV photons are closed by the shutter and fluorescence from $^{229\mathrm{m}}$Th state decay to the ground state is detected by two photomultiplier tubes with T_d detection time (Figure 2.6 left) . The number of detected photons N_d and the lifetime τ' of ^{229}Th transition are related as

$$N_\mathrm{d} \propto N_0 \left(1 - \exp(-T_\mathrm{e}/\tau')\right) \left(\exp\left(-t/\tau'\right)\right), \tag{2.38}$$

where N_0 is a constant and T_e is the time during irradiation of VUV. They chose T_e to 200 s and T_d to 1000 s. From the obtained data (Figure 2.6 right), they fitted it with Equation (2.38) and calculated the upper limit on the transition lifetime of ^{229}Th isomeric state. On the other hand, the lower limit is obtained by fitting the average background without any photon signals. The error of the lifetime τ' is calculated by $\Delta\chi^2$ test statistic in Feldman-Cousins analysis. They concluded that the region of the lifetime $(1-2)$ s $\lesssim \tau \lesssim (2000-5600)$ s for the energy range $7.3 - 8.8$ eV is a exclusion region of existence of the lowest-energy ^{229}Th state within 90 % confidence level. Yamaguchi studied similar experiment [5] with CaF$_2$ crystals attached on ^{229}Th. They used the emission of an undulator device with the line width of 10 nm and scanned the wavelength range of $131 - 318$ nm $(3.9 - 9.5\,\mathrm{eV})$. To detect the fluorescence only from ^{229}Th isomeric state, they also used the shutter to prevent the photons from undulator radiation and the dead time between the excited and detection phase was 10 ms. In this case, T_e was 500 s and T_d was 100 s. From the obtained fluorescence signal (Figure 2.7 left), they fitted the data with a single exponential function but the no clear signal was found. They also fitted the data by the exponential function with free parameter of the amplitude and fixed the decay constant to 50,100, 500 s (Figure 2.7 right). Both results showed the energy range of $3.9 - 9.5$ eV is excluded as a exist range of ^{229}Th isomeric state.

2.3.2   Measurement of Internal Conversion Decay

The key signature of ^{229}Th isomeric state is that it decays and emits an electron due to internal conversion (IC). In 2012, Erik Lars Swanberg studied direct measurement of ^{229}Th isomeric state at Lawrence Livermore National Laboratory (LLNL)[32]. He used an electroplated ^{233}U source to produce the ^{229}Th and the ^{229}Th isomeric state. This measurement used the Alpha Recoil Technique, first the ^{229}Th isomeric state recoil from the ^{233}U source is absorbed in a recoil catcher and second the recoil catcher is removed from the ^{233}U source and is located between a Si detector and PhotoMultiplier Tubes (PMT) with closely located Multi-Channel Plate (MCP) detectors. The Si detector used to measure the energy of alpha particles, the PMT used to detect single photons, and the MCP used to detect individual electrons. He searched for photons and electrons from the ^{229}Th isomeric state, but the decay of ^{229}Th isomeric state was not observed. In 2016, Lars von der Wensen et al., [6]carried out the similar experiment and controlled the ^{229}Th isomeric state emitted from ^{233}U source (Figure 2.8). They tried to detect a low energy by IC decay with shorter half-life. The ^{233}U source was located in a buffer-gas stopping cell where ^{229}Th ions are produced. The kinetic energy of these recoil ions up to 84 keV is removed in ultra-pure helium gas. The slow ^{229}Th ions was guided to a supersonic Laval nozzle by a radio-frequency and
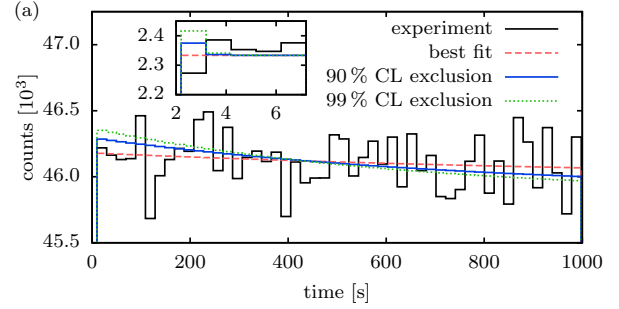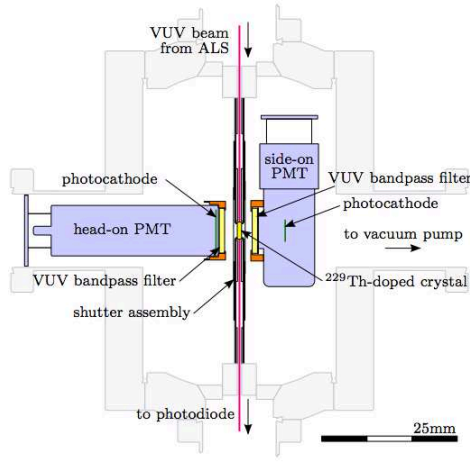
Fig. 2.6 Schematic view of the experiment setup (left) and data with model fit result in $\hbar\omega = 7.7$ eV(right)[4].
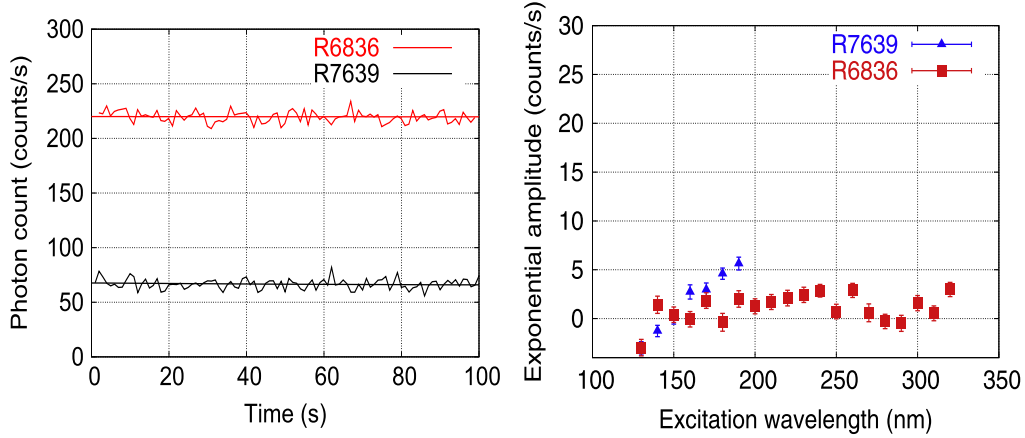
Fig. 2.7 Results of fluorescence signal (left) and the exponential amplitude of the fitting model with excitation wavelength (right) [5].

direct current funnel and then a specific ^{229}Th ions was extracted there. The isolated ^{229}Th ions was sent into a radio-frequency quadrupole. During going through a quadrupole mass-separator, the daughter nuclides of ^{233}U source are separated and ^{229}Th only remains. The specific ^{229}Th ions, ^{229}Th^{2+}, ^{229}Th^{3+} were attached on MCP and radiated the electrons by IC (Figure 2.8). They obtained the upper and lower limit of half-life of the isomer from the decay signal in neutral thorium atom and ^{229}Th^{2+}. Based on the half-life estimate, they reported the energy of the isomeric $E(^{229m}$Th) is

$$6.3 \text{ eV} \le E(^{229\text{m}}\text{Th}) \le 18.3 \text{ eV}. \tag{2.39}$$

2.3.3 Measurement of the Electrons Decay from $^{229\text{m}}$Th with STJ

Other direct measurement was carried out by Ponce with 4 pixels Superconducting Tunnel Junction (STJ) detectors[33]. The measurement used recoil ions and they inserted the recoil ions into STJ detectors, where the decay of ^{229}Thisomeric state was occurred with a particular lifetime. The ions transported the energy up to
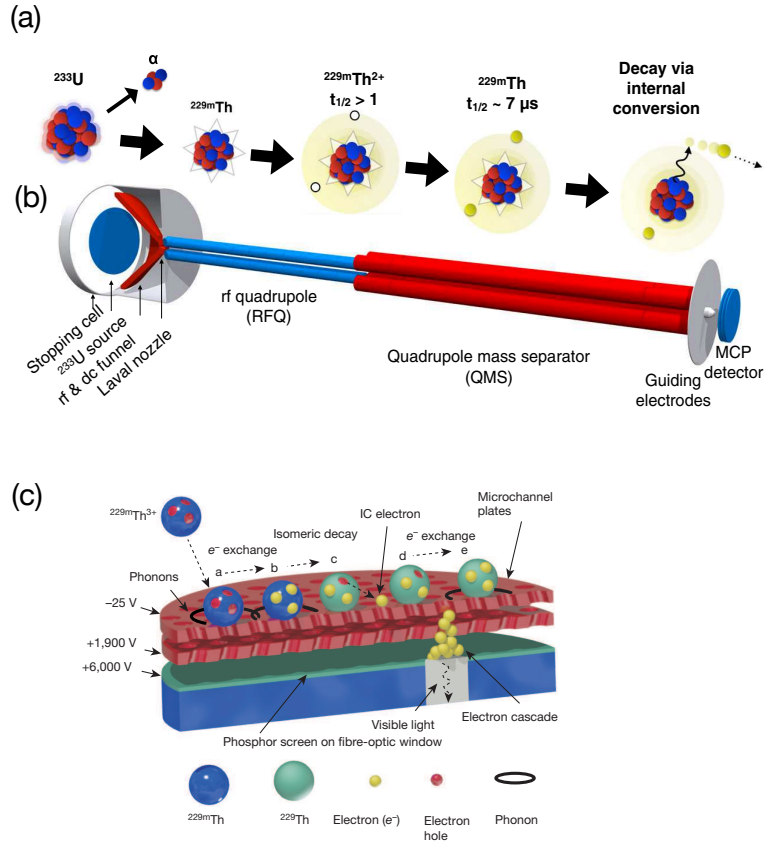
Fig. 2.8   (a)Detailed detection scheme of electrons decay from ^{229m}Th by internal conversion. (b) Scheme of the experiment setup. (c) Scheme of the isomer detection at the MCP detector [6, 7].
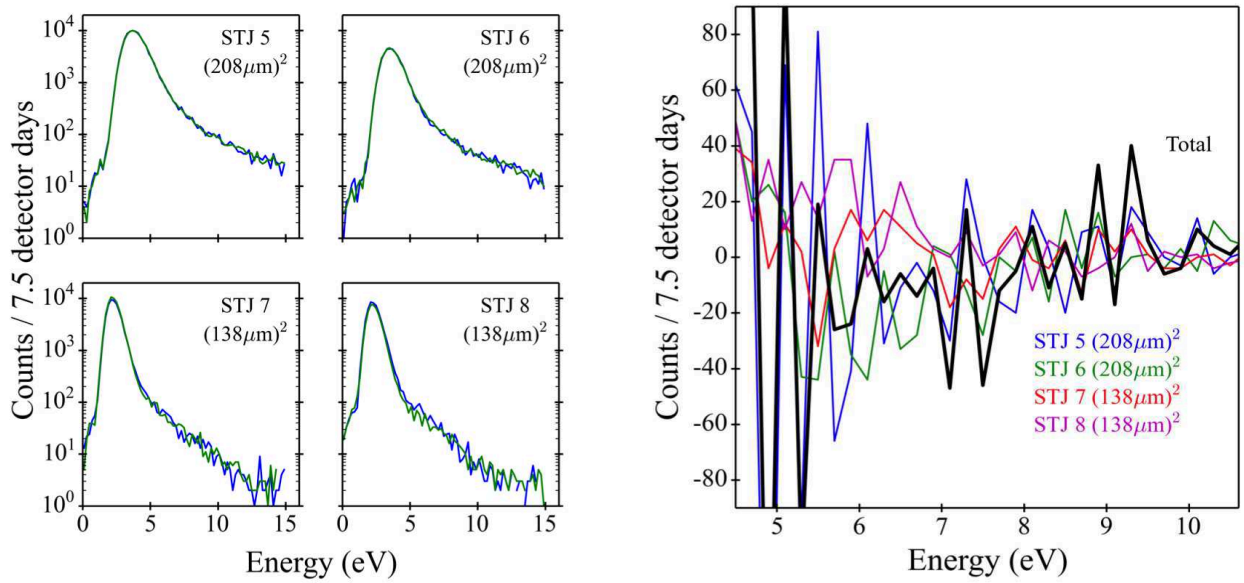
Fig. 2.9   (Left) The energy spectra of four STJ detectors in ^{233}U irradiation, green line and blue line represent respectively before and after a ^{229}Th recoil impact. (Right) Closed up the difference between the before and after spectra. Black line is a sum of total spectrum [8].
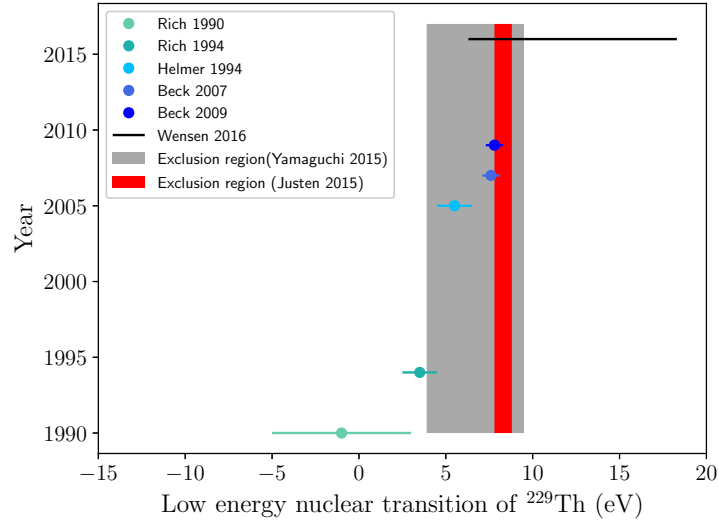
Fig. 2.10 Lowest-energy of ^{229}Th isomeric state from previous measurements, Dots and bars incidental to dots are expressed the measured isomeric energy values and its error, respectively. Solid line is expressed the measured isomeric energy. The grey and red shaded areas are expressed the excluded region.

90 keV and attached the STJ then the energy was converted to low-energy excitation inside the STJ. The STJ detectors taken the energy from the recoil impact and turned back to stationary state after that, the detectors could detect the electron from the internal conversion decay of the ^{229}Th isomeric state. They searched signals between 15 ms and 100 ms before and after the recoil impact considering the relaxation time of the STJ that about 10 ms since the theoretical estimation to the half-life was 10^{-6} s to 10^4 s and widely accepted value was 10^{-3} s. Comparing two spectra which were before and after recoil impact, they concluded that no peak was observed at 7.8 eV (Figure 2.9). They did not see the signals with long time interval because it was considered the signal from high energy electrons. Around the same time, B.Seiferle et. al., 2017[7]reported the half-life of natural ^{229}Th isomeric state by internal conversion was to be 7 ± 1 μs so that Ponse could not detect the signal from the ^{229}Th isomeric state due to the long relaxation time of STJ.

2.4 Summary

The time variation of the fine structure constant was searched several measurements. The advantage of the comparison the two atomic transition frequencies is model independent while the Oklo phenomemo and astrophysical observations are model dependent. In order to improve the sensitivity, it is necessary to use the nuclear clock which reference the lowest-energy of ^{229}Th isomeric state. However, that energy was not exactly determined and several measurements were done. From previous section, we summarize the measured lowest-energy of ^{229}Th isomeric state and express in Figure 2.10. In this figure, Dots and bars incidental to dots express the measured isomeric energy values and its error from previous measurements. Solid line is the measured isomeric energy from [6]. Excluded region obtained by [4, 5] are expressed as grey and red shaded. We consider the isomeric energy of ^{229}Th is between 9.5 eV and 18.3 eV. It is difficult to cover the entire energy range by direct excitation of ^{229m}Th using synchrotron radiation because it is hard to produce the synchrotron radiation correspond to that energy range. The measurement of the lowest-energy of ^{229}Th isomeric transition by γ-ray spectroscopy is desirable.

Chapter 3

γ-ray Spectroscopies of ^{229}Th using TES microcalorimeter

In 2015, we started a TES-Thorium project to measure the lowest-energy of ^{229}Th isomeric transition by γ-ray spectroscopy using a similar way to Beck [3]. In order to obtain an energy resolution at around 29 keV, a microcalorimeter is an only candidate detector because another γ-ray detectors can just archive energy resolution of about 1.5 keV. The microcalorimeter is a detector which measures the energy as a temperature change of the device. It consists of an absorber which absorbers entering photons, a thermometer which measures the temperature of the device, a thermal bath which is made of silicon substrate, and a thermal link which let heat flow to the thermal bath of the device to recover the equilibrium state. There are different types of calorimeters reflecting the difference in thermometer; highly doped semiconductor whose resistance shows temperature dependent even at cryogenic temperatures, a transition edge sensor (TES) which uses a sharp temperature dependence of superconducting material, and a magnetic thermometer which uses temperature dependence of magnetization where a paramagnetism is in a bias magnetic field. We selected the TES microcalorimeter as a detector for this project and developed TES microcalorimeters. In this project, we are collaboration with RIKEN, JAEA, Kyushu University, and Tohoku University. JAEA was in charge of the operation of the refrigerator. The preparation of ^{233}U source was carried out by RIKEN and Tohoku University. ISAS was responsible for the development of the TES device and both ISAS and Kyushu University were responsible for evaluating the performance of the TES device and analyzing the data.

3.1 Two Methods to Measure Lowest-energy of ^{229}Th Isomeric State

We adopt two methods to constrain the isomer energy level. One is to measure energies of four γ-rays, $E(\textcircled{2} \to \textcircled{3}), E(\textcircled{2} \to \textcircled{4})$, $E(\textcircled{3} \to \textcircled{5})$, $E(\textcircled{4} \to \textcircled{6})$ in Figure 2.3 and determine the lowest-energy of ^{229}Th isomeric energy using these lines and branching ration (see Equation 2.28) like [3] and we call it indirect detection. The second method is to separate 29.19 keV doublet which means $E(\textcircled{4} \to \textcircled{5})$ and $E(\textcircled{4} \to \textcircled{6})$ from spectrum. We call it direct detection.

3.2 Requirements for TES Microcalorimeter System

First, we made simulations in order to find how the 29.19 keV doublet will spread and overlap by the energy resolution of the detector. We set the model function of these lines

$$M(E) = N(b_{29} \cdot G(E - E(\textcircled{4} \to \textcircled{5}), \sigma) + (1 - b_{29}) \cdot G(E - E(\textcircled{4} \to \textcircled{6}), \sigma)), \qquad (3.1)$$

Table 3.1 Intensity of 4 γ-ray lines in ^{229}Th

	Energy (keV)	Probability	Intensity
④ → ⑤	29.19	6.69×10^{-5}	0.063
④ → ⑥	29.19–E(^{229m}Th)		
② → ③	29.39	4.91×10^{-6}	0.005
③ → ⑤	42.43	9.02×10^{-4}	0.854
③ → ⑥	42.43–E(^{229m}Th)		
② → ④	42.63	8.20×10^{-5}	0.078
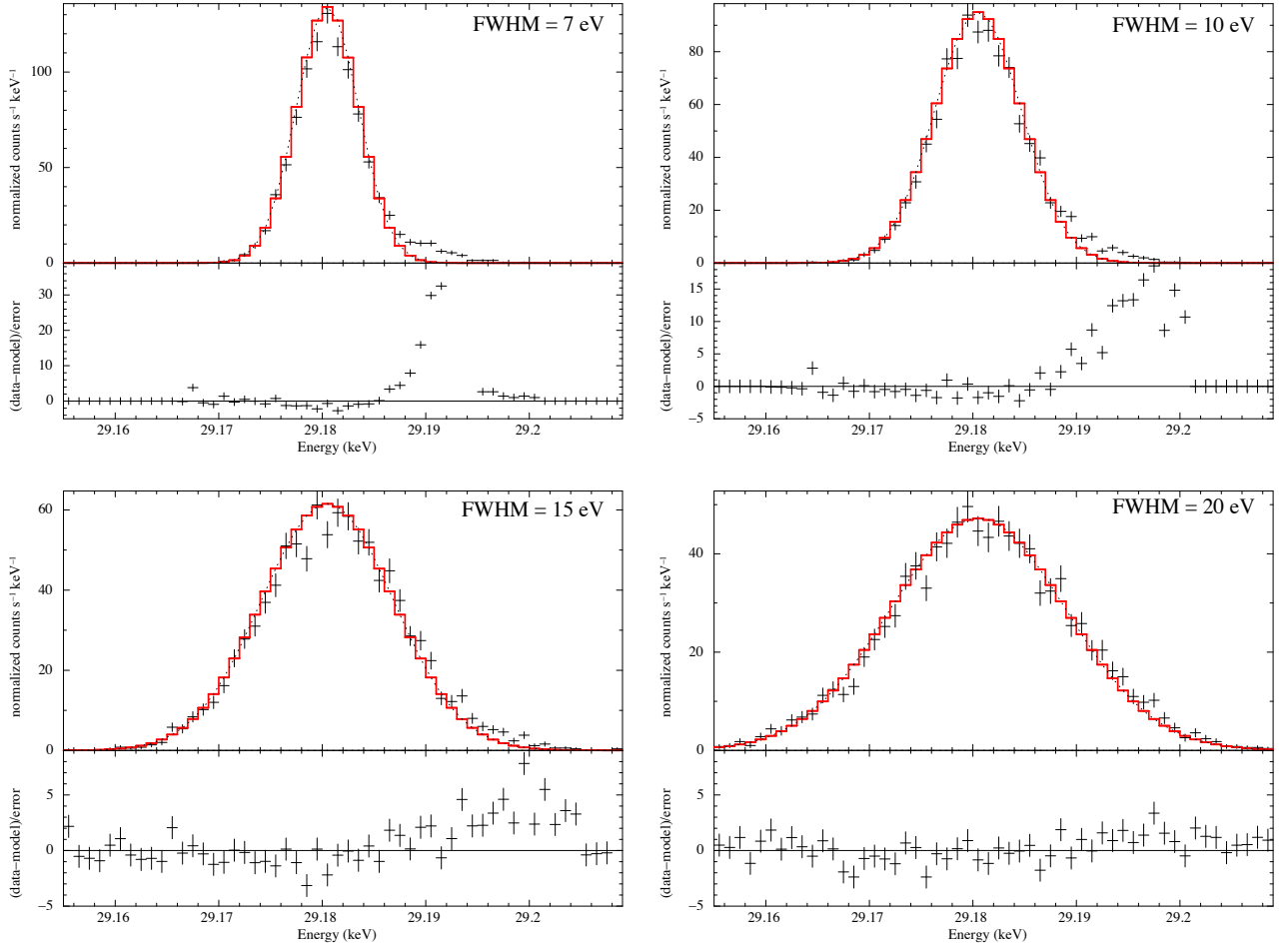
Fig. 3.1 Simulated energy spectrum of 29.19 keV doublet and fit results of line decay from 29.19 keV to isomer state with a single Gaussian assuming E(^{229m}Th) = 9.5 eV. Set the FWHM of the Gaussian to 7 eV (top left), Set the FWHM of the Gaussian to 10 eV (top right), Set the FWHM of the Gaussian to 15 eV (bottom left), Set the FWHM of the Gaussian to 20 eV(bottom right).

where $G(E)$ is a Gaussian function, σ is a energy resolution of the detector represented in Gaussian sigma, and b_{29} is a branching ration of the 29 keV doublet. We set total counts to 5000 and performed the Monte Carlo simulation with fixed the energy resolution. The obtained energy spectrum $f(E)$ were fitted by a single Gaussian $G(E, \sigma)$ setting the energy and the energy resolution as free parameters and we calculated the residual between $f(E)$ and $G(E, \sigma)$. From the residual, we judged whether we can recognize excess due to the low-intensity line. The lowest-energy of ^{229}Th isomeric state is assumed to be 9.5 eV or 18.3 eV (2.4) and the energy resolution is set to 7 eV, 10 eV, 15 eV, and 20 eV (Figure 3.1, 3.2). We found the doublet can be recognized if the energy
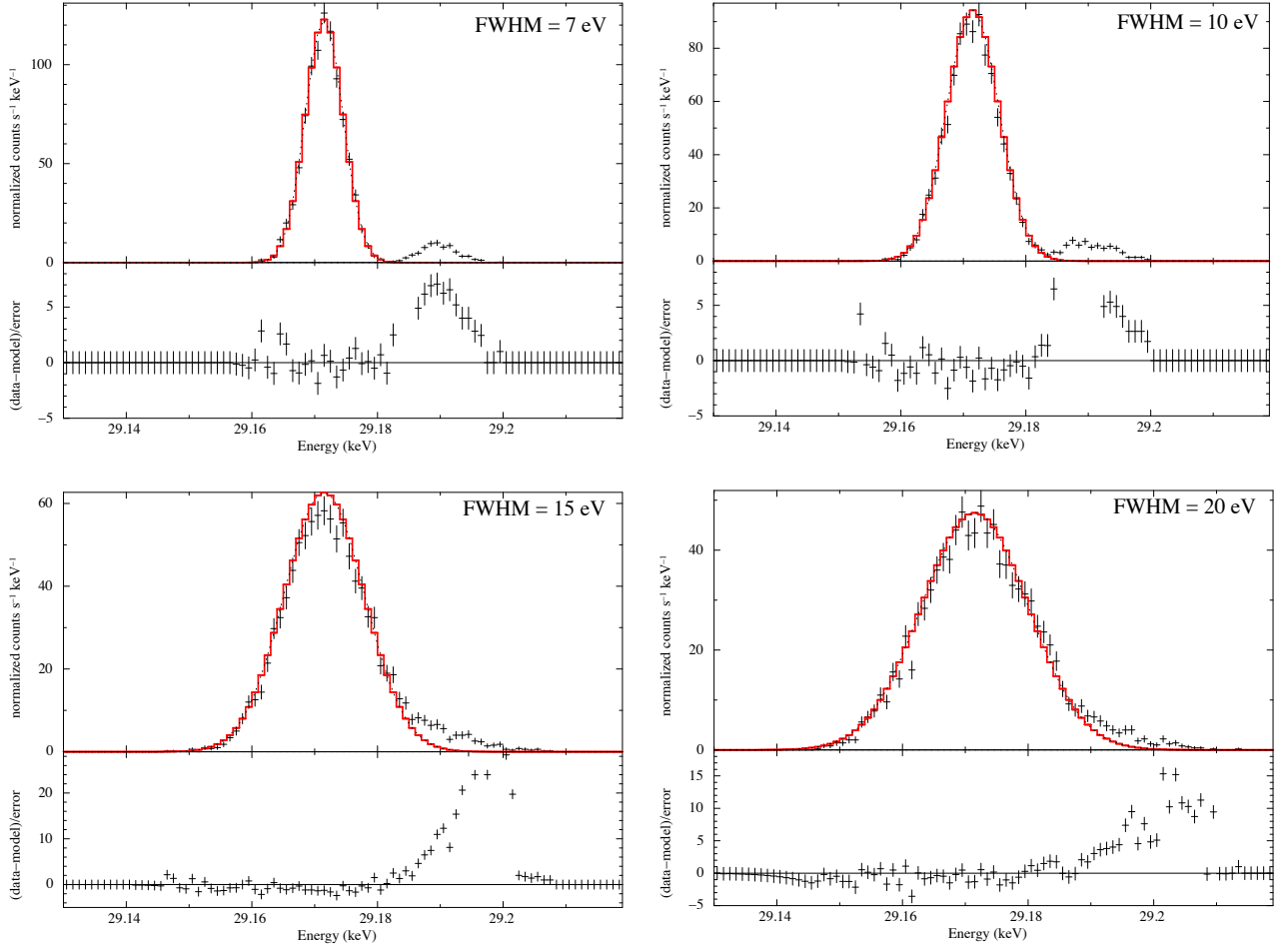
Fig. 3.2   Simulated energy spectrum of 29.19 keV doublet and fit results of line decay from 29.19 keV to isomer state with a single Gaussian assuming $E(^{229m}\text{Th}) = 18.3$ eV. Set the FWHM of the Gaussian to 7 eV (top left), Set the FWHM of the Gaussian to 10 eV (top right), Set the FWHM of the Gaussian to 15 eV (bottom left), Set the FWHM of the Gaussian to 20 eV(bottom right).
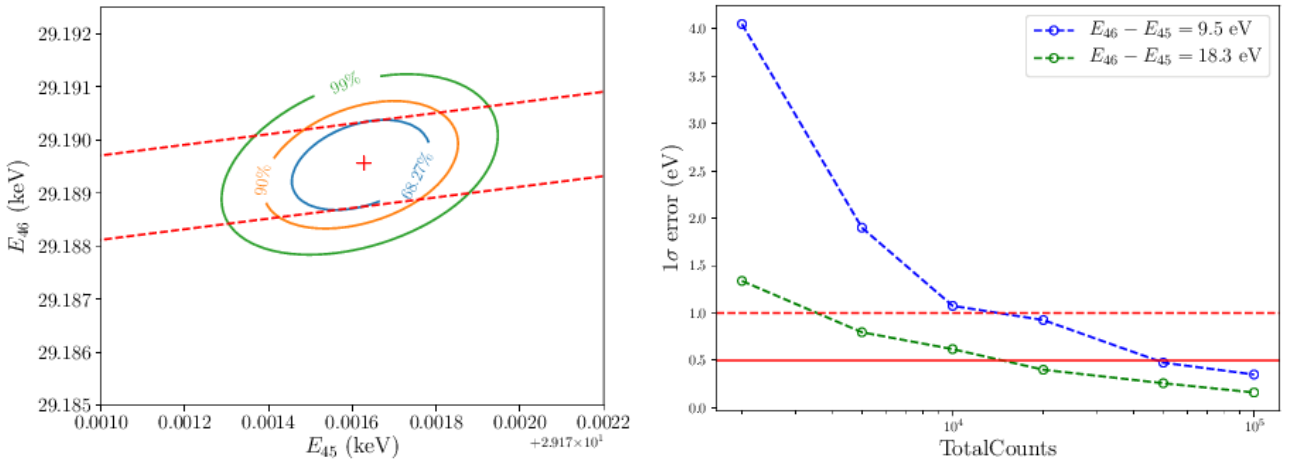
Fig. 3.3   Contour of 29.19 keV doublet in the case of $E(^{229m}\text{Th}) = 18.3$ eV with energy 15 eV energy resolution (left) and total counts vs statistical error with 1 σ

resolution is 15 eV in both cases of 9.5 eV and 18.3 eV. Next, we estimated how much counts we need to obtain the statistical error of the lowest-energy of ^{229}Th isomeric state below 0.5 eV. We generated the 29.19 keV doublet spectrum and fitted the spectrum using two Gaussian functions whose energy and intensity are free. Since the energies of 29.19 keV doublet are correlative relation, we calculated the error using a contour of two energies. The contour was generated by $E(④ \to ⑤)$ and $E(④ \to ⑥)$ and fitted the contour with a linear function assuming $E(④ \to ⑤)_{\max} - E(④ \to ⑥)_{\max} = E(^{229\mathrm{m}}\mathrm{Th})$ and $E(④ \to ⑤)_{\min} - E(④ \to ⑥)_{\min} = E(^{229\mathrm{m}}\mathrm{Th})$. Figure 3.3 shows the contour of 29.19 keV doublet in the case of $E(^{229\mathrm{m}}\mathrm{Th}) = 18.3$ eV. We then calculated the statistical error as the half of the width of the two linear functions. In this way, we calculated the statistical error with 1 σ both $E(^{229\mathrm{m}}\mathrm{Th}) = 9.5$ eV and $E(^{229\mathrm{m}}\mathrm{Th}) = 18.3$ eV with changing the total counts. From the results Figure 3.3, we found that the total counts of 1.5×10^4 and of 5×10^4 are required in the case of $E(^{229\mathrm{m}}\mathrm{Th}) = 18.3$ eV and $E(^{229\mathrm{m}}\mathrm{Th}) = 9.3$ eV respectively.

On the other hand, in the indirect detection, we estimated the total counts which satisfy statistical error as the same in direct detection below 0.5 eV. Assuming that we can calculate the statistical error by error propagation of 4 lines, the error $\delta\sigma$ is

$$\delta\sigma^2 = \frac{\sigma_{\mathrm{E}}^2}{N_{29.19}} + \frac{\sigma_{\mathrm{E}}^2}{N_{29.39}} + \frac{\sigma_{\mathrm{E}}^2}{N_{42.43}} + \frac{\sigma_{\mathrm{E}}^2}{N_{42.63}}, \tag{3.2}$$

$$= \frac{\sigma_{\mathrm{E}}^2}{N_{\mathrm{total}}} \left(\frac{1}{I_{29.19}} + \frac{1}{I_{29.39}} + \frac{1}{I_{42.43}} + \frac{1}{I_{42.63}} \right), \tag{3.3}$$

where σ_{E} is an energy resolution, $I_{29.19}$, $I_{29.39}$, $I_{42.43}$, and $I_{42.63}$ are relative intensities of each lines, and N_{total} is total number of counts. Thus the total number of photons is expressed as

$$N_{\mathrm{total}} = \frac{\sigma_{\mathrm{E}}^2}{\delta\sigma^2} \left(\frac{1}{I_{29.19}} + \frac{1}{I_{29.39}} + \frac{1}{I_{42.43}} + \frac{1}{I_{42.63}} \right). \tag{3.4}$$

When we set the energy resolution 10 eV, the total counts are required 16600. When the energy resolution is 15 eV, 37000 counts are required. Thus, with an energy resolution of 15 eV and total counts of 50×10^3 in the direct detection and of 37×10^3 in the indirect detection, we will be able to obtain 0.5 eV statistical errors.

3.3 TES Microcalorimeter for 30 keV and Its Problems for Measuring 30 keV Photons

TES microcalorimeters have been developed mainly for the energy range below 10 keV (soft X-ray band) using normal conductive metal as an absorber and the best energy resolution is 0.72 eV at 1.5 keV [34]and 1.8 eV at 6 keV [35] and fast decay time ~ 100 μs is obtained. On the other hand, above 100 keV, tin is often used as an absorber because of its low heat capacity and high X/γ-ray stopping power. The slow thermalization of tin is not a problem in this high energy range due to long decay time to return to the thermal equilibrium state. Energy resolutions of 27 to 100 eV have been obtained by[36, 37]. However, TES microcalorimeters optimized for 30 keV have never been developed. We developed TES microcalorimeters with a gold metal absorber for 30 keV by extending the energy range of the TES which was optimized for soft X-ray band.

When TES X-ray microcalorimeters absorb high energy photons (30 keV), non-linear response to the energy arises mainly due to their transition edge characteristic. Because of this non-linear relation between pulse-height-analyses-value (PHA) and energy, the energy resolution degrades with increasing energy. A calibration curve

between PHA and energy including the non-linearity is needed. In our project, we need precise energy-scale and energy-resolution calibrations. We use radio isotopes and some X-ray induced emission line as calibration source whose emission lines contain fine structures and we need spacial care for the calibration.

3.4   Procedures toward Measuring Lowest-energy of ^{229}Th Isomeric State

In order to find out how to calibrate the non-linear energy scale, we conducted firstly an laboratory experiment for the calibration.We irradiated a TES microcalorimeter with a wide energy range of photons simultaneously from 3.3 to 17.8 keV using ^{41}Ca, ^{55}Fe, and ^{241}Am isotope. We then studied how we can derive the PHA to energy calibration curve precisely.

We designed, fabricated and evaluated a TES device for measurement of lowest-energy of ^{229}Th isomeric state at JAEA in Oarai. The energy resolution was 14 eV at 6 keV and 24 eV at 26 keV in our laboratory test. Then we installed the detector stage in the Oarai experiment. We measured the γ-rays from ^{233}U isotope in 449.5 hours. In Oarai experiment, due to thermal fluctuation noise, the energy resolution decreased to 40 eV at 26 keV. We obtained an constraint for the lowest-energy of ^{229}Th isomeric state in the TES resistance analysis, $8.4^{+7.2}_{-5.8} \pm 9.5$ eVwithin the statistical and the systematic error. We identified the source of the noise to be γ-ray irradiation on the silicon substrate of the TES device. We also found that there is room for improvement of the energy resolution and that we can increase counting rate by operating more TES pixels and improve calibration by inserting more calibration lines.

We thus developed a new TES microcalorimeter and a collimator installed very close to the microcalorimeter to reduce γ-ray photons to hit the silicon substrate. We brought the new detector system to Tohoku University. We proved improvement of the energy resolution in this environment.

We also established a new calibration source operation plain and estimated whether we can separate the 29.19 keV doublet using Monte Carlo simulation. However, a problem occurred in the dilution refrigerator and we had to stop the experiment. In this thesis, we report the new developed calibration method, the results in Oarai campaign, the new developed TES device and collimator, and the results of Monte Carlo simulation.

Chapter 4

Transition-Edge Sensor (TES) Calorimeter and Readout system

Calorimeters have been used to as bolometers which measure infrared radiation, and their theory is fully developed [38, 39]. In 1949, Andrews et al. flowed current to a niobium nitride strip at 15 K where its superconducting transition and measured the signals when the alpha particles are incident to the strip. This was the first report of demonstration of a TES calorimeter. The main theories of the calorimeter and TES calorimeter were studied by D.McCammon and K.D.Irwin [40, 41]. In this chapter, we will review the principle of the TES microcalorimeter based on their theory [40, 41].

4.1 X-ray Microcalorimeter

An X-ray microcalorimeter is a spectrometer which measures a photon energy as a small temperature rise. The X-ray calorimeter has three parts: there are an absorber that absorbs photons, a thermometer that measures the temperature rise caused by photons, and a low temperature heat sink which connects with the thermometer by thermal conductance G(Figure 4.1). Phonons are absorbed by the photoelectronic effect in the absorber and are converted to thermal energy. In that time, the temperature change (ΔT) in the device is represented as
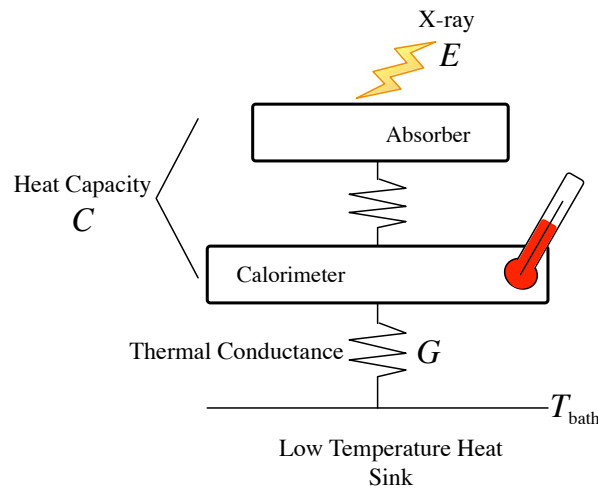
Fig. 4.1   Schematic view of calorimeter

$$\Delta T = \frac{E}{C}. \tag{4.1}$$

Strictly speaking, the heat capacity, C, also changes with the temperature change in device, there is a non-linear relation between energy and temperature change. The heat generated by photons flows to a heat sink through thermal link and then temperature decay back to its equilibrium state. The thermal flow is represented by

$$C\frac{d\Delta T}{dt} = -G\Delta T. \tag{4.2}$$

From this equation, the decay time τ_0 is

$$\tau_0 = \frac{C}{G}. \tag{4.3}$$

In principle, an energy resolution is independent of incident energies and is determined by fluctuation of the number of photons in the device. The number of phonon is represented by the total thermal energy of the calorimeter (CT) and the average energy in a phono ($k_{\mathrm{B}}T$)

$$N = \frac{CT}{k_{\mathrm{B}}T}, \tag{4.4}$$

where k_{B} is the Boltzmann constant. The statistical fluctuation of phonons is

$$\sqrt{N} = \sqrt{\frac{CT}{k_B T}}. \tag{4.5}$$

The thermal fluctuation of the device by the fluctuation of phonons is

$$\Delta U = \sqrt{\frac{CT}{k_B T}}k_{\mathrm{B}}T = \sqrt{Ck_{\mathrm{B}}T^2}. \tag{4.6}$$

The main part of the fluctuation is the fluctuation of phonons since the thermal fluctuation generated by the incident X-ray is small so that the energy resolution depends on statistical fluctuation of phonons. The Full width half maximum (FWHM) of the energy resolution is represented by

$$\Delta E_{\mathrm{FWHM}} = 2.35k_{\mathrm{B}}T\sqrt{N} = 2.35\sqrt{Ck_{\mathrm{B}}T^2}. \tag{4.7}$$

Generally, the energy resolution depends on the sensitivity of temperature and is described using the coefficient $\xi \propto \sqrt{1/\alpha}$

$$\Delta E_{\mathrm{FWHM}} = 2.35\xi\sqrt{Ck_{\mathrm{B}}T^2}. \tag{4.8}$$

To achieve the high energy resolution, it needs to operate low temperature (~ 100 mK) and have a high sensitivity (α).

4.2   TES : Transition edge sensor

Transition edge sensor is a very-high sensitive thermometer using a superconductor. It reads a temperature change as a resistance change with a very narrow transition edge (Figure 4.2). The sensitivity of the thermometer is defined as
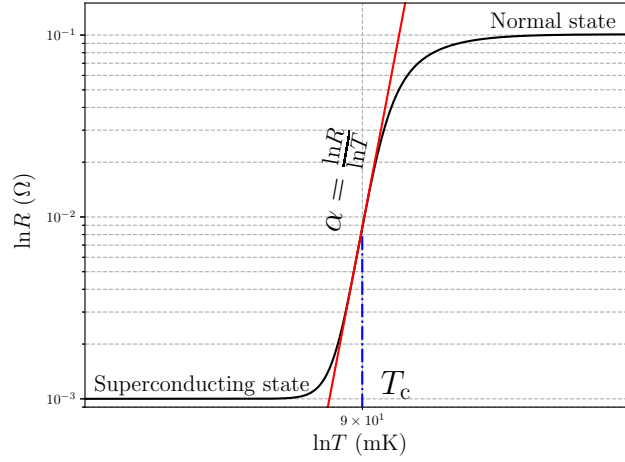
Fig. 4.2   Transition edge

$$\alpha \equiv \frac{d\ln R}{d\ln T} = \frac{T}{R}\frac{dR}{dT}. \tag{4.9}$$

TES has $\alpha \sim 100$, on the other hand semiconductor calorimeters like XRS has $|\alpha| \leq 6$. The energy resolution of the TES is proportional to $\sqrt{1/\alpha}$ and is one hundred times higher than that of semiconductor calorimeters. When we use the TES calorimeter, the TES calorimeter is needed to operate within the transition edge. Transition temperature is controlled using proximity effect in the biliary of superconductor and normal conductor.

4.3   Basic Parameters

4.3.1   Heat Capacity

The heat capacity C is a important parameter for calorimeters and that determines the energy resolution and a decay time constant. The heat capacity is represented by using molar specific heat, c, density, ρ, atom weight, M, volume, V,

$$C = c\frac{\rho V}{M}. \tag{4.10}$$

When temperature is too lower than the Fermi temperature and Debye temperature, the specific heat at constant volume is sum of a lattice specific heat (c_l) caused by phonons fluctuation and an electron specific heat (c_e) caused by conduction electrons fluctuation

$$c = c_l + c_e. \tag{4.11}$$

Lattice specific heat c_l

Using the Debye model [42, 43], a state density of three-dimensional is represented as

$$D(\omega) = \frac{V\omega^2}{2\pi^2 v^3}, \tag{4.12}$$

where V is a volume, v is a sound velocity K is a wave vector and $\omega = v \cdot K$. The upper limit of the frequency of the lattice vibration, ω_{D}, is calculated by the total number of mode in which the wave vector is less than K

$$\omega_{\mathrm{D}}^3 = \frac{6\pi^2 v^3 N}{V}. \tag{4.13}$$

The upper limit of the wave vector, K_{D}, is also calculated by

$$K_{\mathrm{D}} = \frac{\omega_{\mathrm{D}}}{v}, \tag{4.14}$$

$$= \left(\frac{6\pi^2 N}{V}\right)^{1/3}. \tag{4.15}$$

In the Debye model, the wave vector which is larger than K_{D} is not allowed. The internal energy U is calculated as

$$U = \int_{-\infty}^{\infty} D(\omega) \frac{\hbar\omega}{e^{\hbar\omega/k_{\mathrm{B}}T} - 1} d\omega, \tag{4.16}$$

$$= \int_{0}^{\omega_{\mathrm{D}}} \frac{V\omega^2}{2\pi^2 v^3} \cdot \frac{\hbar\omega}{e^{\hbar\omega/k_{\mathrm{B}}T} - 1} d\omega, \tag{4.17}$$

$$= \frac{3V k_{\mathrm{B}}^4 T^4}{2\pi^2 v^3 \hbar^3} \int_{0}^{x_{\mathrm{D}}} \frac{x^3}{e^x - 1} dx. \tag{4.18}$$

where $x = \hbar\omega/k_{\mathrm{B}}T$ and $x_{\mathrm{D}} \equiv \hbar\omega_{\mathrm{D}}/k_{\mathrm{B}}T \equiv \theta/T$. We define the θ as the Debye temperature

$$\theta = \frac{\hbar v}{k_{\mathrm{B}}} \cdot \left(\frac{6\pi^2 N}{V}\right)^{1/3}. \tag{4.19}$$

Then U is

$$U = 9N k_{\mathrm{B}} T \left(\frac{T}{\theta}\right)^3 \int_{0}^{x_{\mathrm{D}}} \frac{x^3}{e^x - 1} dx. \tag{4.20}$$

When T is extremely low ($T \ll \theta$), the result of the integral part in Equation (4.20) is

$$\int_{0}^{\infty} \frac{x^3}{e^x - 1} dx = \zeta(4)\,\Gamma(4) = \frac{\pi^4}{15}, \tag{4.21}$$

and U is obtained as

$$U \simeq \frac{3\pi^4}{5} N k_{\mathrm{B}} T \left(\frac{T}{\theta}\right)^3. \tag{4.22}$$

The lattice specific heat in $T \ll \theta$ is calculated by Equation (4.22)

$$c_l = \frac{\partial U}{\partial T} \simeq \frac{12\pi^4}{5} N k_{\mathrm{B}} \left(\frac{T}{\theta}\right)^3, \tag{4.23}$$

$$= 234 N k_{\mathrm{B}} \left(\frac{T}{\theta}\right)^3 \ (\mathrm{J/mol \cdot K}). \tag{4.24}$$

Electronic specific heat c_{e}

Electrons near the fermi state contribute to electronic specific heat. We can calculate the electronic specific heat using Fermi-Dirac statistic. Fermi-Dirac distribution gives the number of particles with energy ϵ under the temperature T and the chemical potential μ

$$f_{\mathrm{FD}}(\epsilon) = \frac{1}{e^{(\epsilon-\mu)/k_{\mathrm{B}}T} - 1}. \tag{4.25}$$

In the energy below the Fermi energy ($k_{\mathrm{B}}T \ll \epsilon_{\mathrm{F}}$), the change of internal energy U when the temperature changes from 0 to T is represented as [43]

$$\Delta U = \int_{\epsilon_{\mathrm{F}}}^{\infty} (\epsilon - \epsilon_{\mathrm{F}}) D(\epsilon) f_{\mathrm{FD}}(\epsilon) d\epsilon + \int_{0}^{\epsilon_{\mathrm{F}}} (\epsilon_{\mathrm{F}} - \epsilon)[1 - f(\epsilon)] D(\epsilon) d\epsilon. \tag{4.26}$$

The electronic specific heat is calculated by differentiating the internal energy with respect to the temperature

$$c_{\mathrm{e}} = \frac{dU}{dT} = \int_{0}^{\infty} (\epsilon - \epsilon_{\mathrm{F}}) \frac{df_{\mathrm{FD}}}{dT} D(\epsilon) d\epsilon. \tag{4.27}$$

We evaluate the state density $D(\epsilon)$ with ϵ_{F} and put it outside the integral. In the $k_{\mathrm{B}}T \ll \epsilon_{\mathrm{F}}$, we can set the chemical potential μ to ϵ_{F}. Then the electronic specific heat is

$$c_{\mathrm{e}} = \frac{\pi^2 k_{\mathrm{B}}^2}{3} D(\epsilon_{\mathrm{F}}) T. \tag{4.28}$$

4.3.2   Thermal Conductance

The thermal conductance is defined as

$$G \equiv dP/dT, \tag{4.29}$$

and it depends on the temperature

$$G = G_0 T^{n-1}. \tag{4.30}$$

where n is determined by the mediums conducting heat. In the case of electrons conduct heat, then $n = 2$. In the other case of the lattice conduct heat, then $n = 4$. Considering the thermal conductance between thermal link and TES, the temperature of the TES is higher than bath temperature $T \gg T_{\mathrm{bath}}$. The heat flowing between

TES and thermal link is calculated by integrating Equation (4.29)

$$p = \int\limits_{T_{\text{bath}}}^{T} G dT,$$
$$= \frac{G_0}{n} \left(T^n - T_{\text{bath}}^n\right). \tag{4.31}$$

If the difference of T and T_{bath} is large enough, we can approximate the temperature to the transition temperature T_c and the equation is written by T_c

$$P \simeq \frac{G T_c}{n} \left(1 - \left(\frac{T_{\text{bath}}}{T_c}\right)^n\right). \tag{4.32}$$

4.4   TES-Responses in Linear Region

4.4.1   ETF: Electrothermal Feedback

TES is a very sensitive thermometer however, the operating points is needed to keep on a very narrow transition edge. We apply the voltage-bias to TES and keep the operating point by a negative feedback. A temperature change in a TES is transduced into an electrical current change by the change in the resistance of the TES. The electrical current signal in the TES is fed back into a temperature change by Joule power dissipation. This is called electrothermal feedback (ETF) process. Under voltage-bias conditions, as the temperature and resistance increase, the Joule power, $P_{\text{J}} = V^2/R$, decreases, and electrothermal feedback is negative. Negative feedback makes the detector response linear and the dynamic range increase. This feedback technique for the TES is studied by [44, 40]. The heat conduction equation of a TES with the temperature T is represented by,

$$C \frac{dT}{dt} = P_{\text{out}} + P_J - P_{\text{bath}}. \tag{4.33}$$

When X-ray photons enter the TES, and then the temperature rises as minute temperature change $\Delta T \equiv T - T_0$, the change of internal energy is equal to heat balance

$$C \frac{dT}{dt} = \frac{V_{\text{b}}}{R(T)} - \frac{G_0}{n}(T^n - T_{\text{bath}}^n). \tag{4.34}$$

The temperature change ΔT is by the first approximation of Equation (4.34)

$$C \frac{d\Delta T}{dt} \simeq \frac{V_{\text{b}}^2}{R_0^2} \Delta R - G_0 T^{n-1} \Delta T, \tag{4.35}$$
$$= \frac{P_{\text{b}} \alpha}{T} \Delta T - G \Delta T, \tag{4.36}$$

where $G = G_0 T^{n-1}$. The solution of Equation (4.36) is

$$\Delta T = \Delta T_0 \exp\left(-\frac{t}{\tau_{\text{eff}}}\right), \tag{4.37}$$

where τ_{eff} is effective decay time in ETF and is represented with intrinsic decay time τ_0

$$\tau_{\mathrm{eff}} \equiv \frac{C/G}{1 + \frac{P_{\mathrm{b}}\alpha}{GT}}, \tag{4.38}$$

$$= \frac{\tau_0}{1 + \frac{P_{\mathrm{b}}\alpha}{GT}}. \tag{4.39}$$

The effective decay time is smaller than the intrinsic decay time and the TES returns to the thermal equilibrium state. Equation (4.39) is written as

$$\tau_{\mathrm{eff}} = \frac{\tau_0}{1 + \frac{\alpha}{n}\left(1 - \left(\frac{T_{\mathrm{bath}}}{T}\right)^n\right)}. \tag{4.40}$$

The bath temperature is much smaller than the temperature of the TES ($T_{\mathrm{bath}} \ll T$), the effective decay time is approximated as

$$\tau_{\mathrm{eff}} = \frac{\tau_0}{1 + \frac{\alpha}{n}}, \tag{4.41}$$

$$\simeq \frac{n}{\alpha}\tau_0, \tag{4.42}$$

where $\alpha/n \gg 1$. The X-ray energy is read out by the current change, and the current change is represented by

$$\Delta I = \frac{V_{\mathrm{b}}}{R(T_0 + \Delta T)} - \frac{V_{\mathrm{b}}}{R(T_0)}, \tag{4.43}$$

$$\simeq -\frac{\Delta R}{R}I, \tag{4.44}$$

$$\simeq -\alpha\frac{E}{CT}I. \tag{4.45}$$

4.4.2   ETF Diagram

We consider the response of the TES in the case of entering the minute power depends on time $\delta P e^{i\omega t}$. The temperature change correspond to $\delta P e^{i\omega t}$ is expressed as $\delta T e^{i\omega t}$. The heat conduction equation without feedback is

$$C\frac{d}{dt}(\delta T e^{i\omega t}) = P_{\mathrm{bad}} + \delta P_{\mathrm{bad}}e^{i\omega t} - \frac{G_0}{n}\left((T + \delta T e^{i\omega t})^n - T_{\mathrm{bath}}^n\right), \tag{4.46}$$

where P_{bad} is back ground power. In the equilibrium state, the power is

$$P_{\mathrm{bad}} = \frac{G_0}{n}(T^n - T_{\mathrm{bath}}^n). \tag{4.47}$$

δT is expressed with δP by Equation (4.46) and (4.47)

$$\delta T = \frac{1}{G}\frac{1}{1 + i\omega\tau_0}\delta P. \tag{4.48}$$

Under the ETF, the equation of conservation of energy is

$$C\frac{d}{dt}(\delta T e^{i\omega t}) = P_{\mathrm{bad}} + \delta P_{\mathrm{bad}}e^{i\omega t} + P_{\mathrm{b}} + \delta P_{\mathrm{b}}e^{i\omega t} - \frac{G_0}{n}\left((T + \delta T e^{i\omega t})^n - T_{\mathrm{bath}}^n\right). \tag{4.49}$$
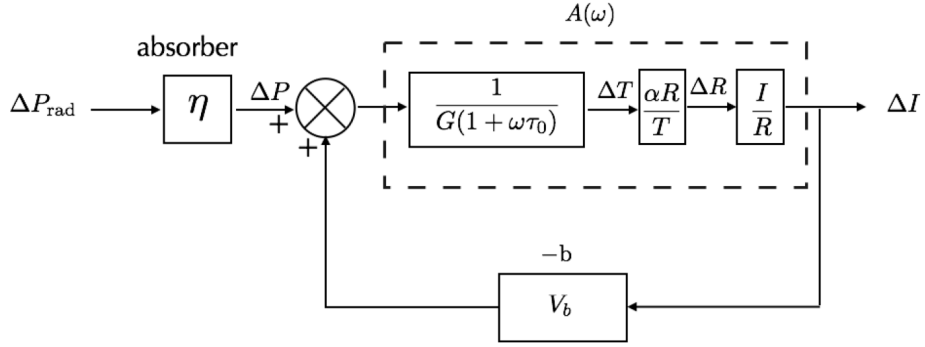
Fig. 4.3   The ETF diagram under the constant voltage bias

The heat conduction equation without external power is

$$P_{bgd} + P_b = \bar{G}(T - T_{\text{bath}}). \tag{4.50}$$

Following relation expressions are consist under the constant voltage

$$\delta P_b e^{i\omega t} = \frac{dP_b}{dI} \delta I e^{i\omega t} = V_b \delta I e^{i\omega t}, \tag{4.51}$$

$$\delta I e^{i\omega t} = \frac{dI}{dR} \delta R e^{i\omega t} = -\frac{V_b}{R^2} \delta R e^{i\omega t}, \tag{4.52}$$

$$\delta R e^{i\omega t} = \frac{dR}{dT} \delta T e^{i\omega t} = \alpha \frac{R}{T} \delta T e^{i\omega t}. \tag{4.53}$$

Using these equation, Equation (4.49) is

$$P_{bgd} + \delta P e^{i\omega t} + P_b - \frac{V_b^2}{R} \frac{\alpha}{T} \delta T e^{i\omega t} = \bar{G}(T - T_{\text{bath}}) + G \delta T e^{i\omega t} + i\omega C \delta T e^{i\omega t}. \tag{4.54}$$

Then δT is expressed with δP,

$$\delta T = \frac{1}{\alpha \frac{P_b}{T} + G + i\omega C} \delta P, \tag{4.55}$$

$$= \frac{1}{G} \frac{1}{\frac{\alpha P_b}{GT}} \frac{1}{1 + i\omega \tau_{eff}} \delta P, \tag{4.56}$$

where τ_{eff} is equal to Equation (4.39).

4.4.3   Formulation of ETF as Feedback

Figure 4.3 shows the system of ETF as a feedback circuit. The quantity of feedback b and loop gain $\mathcal{L}(\omega)$ is respectively

$$b = -V_{\mathrm{b}}, \tag{4.57}$$

$$\mathcal{L} = \frac{1}{G(1+i\omega\tau_0)} \times \alpha\frac{R}{T} \times \left(-\frac{I}{R}\right) \times (-V_{\mathrm{b}}), \tag{4.58}$$

$$= \frac{\alpha P_{\mathrm{b}}}{GT}\frac{1}{1+i\omega\tau_0}, \tag{4.59}$$

$$\equiv \frac{\mathcal{L}_0}{1+i\omega\tau_0}, \tag{4.60}$$

where

$$\mathcal{L}_0 \equiv \frac{\alpha P_{\mathrm{b}}}{GT}, \tag{4.61}$$

is a loop gain where frequency is zero.

4.4.4   Current Responsively

In operating TES under the ETF, the incident power δP is outputted as the current change δI. We define a transfer function as

$$S_I(\omega) \equiv \frac{\delta I}{\delta P}. \tag{4.62}$$

The transfer function is denoted by the loop gain $\mathcal{L}(\omega)$

$$S_I(\omega) = \frac{1}{b}\frac{\mathcal{L}(\omega)}{1+\mathcal{L}(\omega)}, \tag{4.63}$$

$$= -\frac{1}{V_{\mathrm{b}}}\frac{\mathcal{L}_0}{\mathcal{L}_0+1\omega\tau_0}, \tag{4.64}$$

$$= -\frac{1}{V_{\mathrm{b}}}\frac{\mathcal{L}_0}{\mathcal{L}_0+1}\frac{1}{1+i\omega\tau_{\mathrm{eff}}}. \tag{4.65}$$

The power of S_I is

$$|S_I(\omega)|^2 = \frac{1}{V_{\mathrm{b}}^2}\left(\frac{\mathcal{L}_0}{\mathcal{L}_0+1}\right)^2\frac{1}{1+\omega^2\tau_{\mathrm{eff}}^2}. \tag{4.66}$$

For a large loop gain ($\mathcal{L}_0 \gg 1$), Equation (4.67) is

$$S_I(\omega) = -\frac{1}{V_{\mathrm{b}}}\frac{1}{1+i\omega\tau_{\mathrm{eff}}}. \tag{4.67}$$

For the $\omega \ll 1/\tau_{\mathrm{eff}}$, Equation (4.67) is

$$S_I(\omega) = -\frac{1}{V_{\mathrm{b}}}. \tag{4.68}$$

$S_I(\omega)$ is called current responsively and this responsively is to be in inverse proportion to bias voltage.

4.4.5   Actual Response

In the case of entering the X-ray photons, the response correspond to incident power $P(t) = E\delta(t)$ is calculated by following procedure. The input power $P(t)$ is assumed to be delta function when the temperate change of the device by absorbing the X-ray photons is much faster than the response speed of TES. The input power in angular frequency space $(-\infty < \omega < \infty)$,

$$P(\omega) = \frac{1}{2\pi} \int_{-\infty}^{\infty} E\delta(t)e^{i\omega t}dt, \tag{4.69}$$

$$= \frac{E}{2\pi}. \tag{4.70}$$

In the angular frequency space, the output current $I(\omega)$ is calculated by multiplying $P(\omega)$ and $S_I(\omega)$

$$I(\omega) = S_I(\omega)P(\omega), \tag{4.71}$$

$$= -\frac{E}{2\pi V_{\rm b}} \frac{\mathcal{L}_0}{\mathcal{L}_0 + 1} \frac{1}{1 + i\omega\tau_{\rm eff}}. \tag{4.72}$$

We convert $I(\omega)$ to $I(t)$ by inverse Fourier transform,

$$I(t) = \int_{-\infty}^{\infty} I(\omega)e^{-i\omega t}d\omega, \tag{4.73}$$

$$= -\frac{E}{2\pi V_{\rm b}} \frac{\mathcal{L}_0}{\mathcal{L}_0 + 1} \int_{-\infty}^{\infty} \frac{e^{-i\omega t}}{1 + i\omega\tau_{\rm eff}}d\omega, \tag{4.74}$$

$$= -\frac{E}{V_b\tau_{\rm eff}} \frac{\mathcal{L}_0}{\mathcal{L}_0 + 1} \exp\left(-\frac{t}{\tau_{\rm eff}}\right), \tag{4.75}$$

$$= -\frac{\alpha E}{CT}I_0 \exp\left(-\frac{t}{\tau_{\rm eff}}\right). \tag{4.76}$$

This equation consists with Equation (4.45). I_0 is a current though the TES under the equilibrium state. On the other hands, the temperature change by the input $P(t) = E\delta(t)$ in frequency space is

$$\Delta T(\omega) = \frac{1}{G(1 + i\omega\tau_0)} \frac{1}{1 + \mathcal{L}(\omega)}P(\omega), \tag{4.77}$$

$$= \frac{1}{2\pi} \frac{E}{G} \frac{1}{1 + \mathcal{L}_0} \frac{1}{1 + i\omega\tau_{\rm eff}}. \tag{4.78}$$
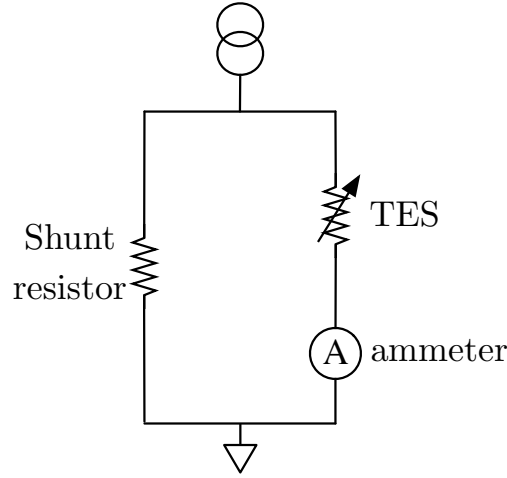
Fig. 4.4   A pseudo constant voltage-bias circuit
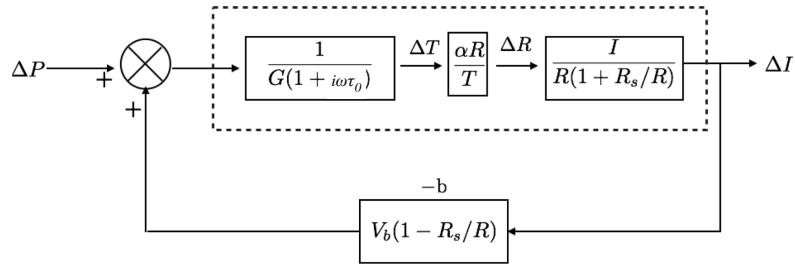
Fig. 4.5   ETF diagram in a pseudo constant voltage-bias

We convert $\Delta T(\omega)$ to $\Delta T(t)$ by inverse Fourier transform,

$$\Delta T(t) = \int\limits_{-\infty}^{\infty} \Delta T(\omega)e^{-i\omega t}d\omega, \tag{4.79}$$

$$= \frac{1}{2\pi}\frac{E}{G}\frac{1}{1+\mathcal{L}_0}\int\limits_{-\infty}^{\infty}\frac{e^{-i\omega t}}{1+i\omega\tau_{\text{eff}}}d\omega, \tag{4.80}$$

$$= \frac{E}{G\tau_{\text{eff}}}\frac{1}{1+\mathcal{L}_0}\exp\left(-\frac{t}{\tau_{\text{eff}}}\right), \tag{4.81}$$

$$= \frac{E}{C}\exp\left(-\frac{t}{\tau_{\text{eff}}}\right). \tag{4.82}$$

4.5   Compensations in Actual Circuit

In previous subsection, we assume the ideal constant voltage but, we apply a pseudo constant voltage by using a shunt resistance. The resistance of TES depends on temperature and also current. In this subsection, we consider the compensations of formulas that we lead previous section by considering these effect.

We use the pseudo constant voltage-bias circuit in actual operating. We apply a small resistor R_s in parallel with the TES resistance $R_{\text{TES}} \gg R_s$. The current, I, though the TES and joule heat power, P, is expressed as

$$I = \frac{R_{\text{s}}}{R + R_{\text{s}}} I_{\text{b}}, \tag{4.83}$$

$$P = I^2 R(I). \tag{4.84}$$

The current change to resistance and the power change to current is calculated as

$$\frac{\delta I}{\delta R} = -\frac{I}{R(1 + \frac{R_{\text{s}}}{R})}, \tag{4.85}$$

$$\frac{\delta P}{\delta I} = V_{\text{b}} \left(1 - \frac{R_{\text{s}}}{R}\right). \tag{4.86}$$

The diagram of ETF is shown in Figure 4.5. The loop gain, $\mathcal{L}_1$ and quantity of feedback, b_1 is

$$\mathcal{L}(\omega) = \frac{1}{G(1 + i\omega\tau_0)} \frac{\alpha R}{T} \frac{I}{R(1 + R_{\text{s}}/R)} V_{\text{b}}(1 - R_{\text{s}}/R) = \mathcal{L}_0 \frac{1}{1 + i\omega\tau_0} \frac{1 - R_{\text{s}}/R}{1 + R_{\text{s}}/R} = \frac{\mathcal{L}_1}{1 + i\omega\tau_0}, \tag{4.87}$$

$$b_1 = -V_{\text{b}} \left(1 - \frac{R_{\text{s}}}{R}\right). \tag{4.88}$$

where, $\mathcal{L}_1$ is

$$\mathcal{L}_1 = \frac{1 - R_{\text{s}}/R}{1 + R_{\text{s}}/R} \mathcal{L}_0. \tag{4.89}$$

The current responsibility S_I is

$$S_I = \frac{1}{b_1} \frac{\mathcal{L}(\omega)}{1 + \mathcal{L}(\omega)}, \tag{4.90}$$

$$= -\frac{1}{V_{\text{b}} \left(1 - \frac{R_{\text{s}}}{R}\right)} \frac{\mathcal{L}_1}{\mathcal{L}_1 + 1} \frac{1}{1 + i\omega\tau'_{\text{eff}}}. \tag{4.91}$$

The effective decay time in pseudo constant voltage bias is

$$\tau'_{\text{eff}} \equiv \frac{\tau_0}{\mathcal{L}_1 + 1}. \tag{4.92}$$

4.6   Intrinsic Noise

There are several noises in operating a TES such as the statical fluctuations, the Jonson noise, thermal fluctuations, a 1/f noise, and a rf noise. When we use the TES, the Johnson noise and the phonon noise always exist and the energy resolution of TES is limited by these noises. The Johnson noise which occurs in thermometer resistance and the phonon noise which is a thermal fluctuation noise caused by a finite thermal conduction [40]. Figure 4.6 shows the ETF diagram within the Johnson noise and the phonon noise. The phonon noise inputs same as signal caused by thermal origin. On the other hand, Johnson noise inputs when the signal becomes resistance change caused by resistance origin. The minute phonon noise change δP_{ph} becomes minute current
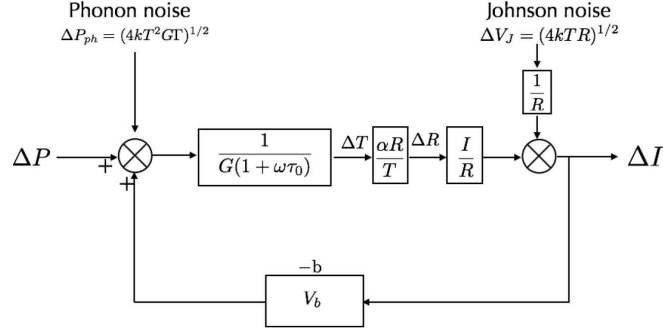
Fig. 4.6   ETF diagram within Johnson noise and phonon noise

change, δI_{ph}

$$\delta I_{\mathrm{ph}} = S(\omega)\delta P_{\mathrm{ph}}, \tag{4.93}$$

$$= -\frac{1}{V_{\mathrm{b}}}\frac{\mathcal{L}_0}{\mathcal{L}_0 + 1}\frac{1}{1 + i\omega\tau_{\mathrm{eff}}}\delta P_{\mathrm{ph}}. \tag{4.94}$$

The current density of phonon noise is

$$\delta I_{\mathrm{ph}}^2 = |S_I|^2 \delta P_{\mathrm{ph}}^2, \tag{4.95}$$

$$= \frac{1}{V_{\mathrm{b}}^2}\left(\frac{\mathcal{L}_0}{\mathcal{L}_0 + 1}\right)^2 \frac{1}{1 + \omega^2\tau_{\mathrm{eff}}^2}\delta P_{\mathrm{ph}}^2. \tag{4.96}$$

The power density of phonon noise in $0 \le f \le \infty$ is

$$\delta P_{\mathrm{ph}}^2 = 4k_{\mathrm{B}}GT^2\frac{\int_{T_{\mathrm{bath}}}^{T}\left(\frac{t_\kappa(t)}{T_\kappa(T)}\right)^2 dt}{\int_{T_{\mathrm{bath}}}^{T}\left(\frac{\kappa(t)}{\kappa(T)}\right)^2 dt}, \tag{4.97}$$

$$\equiv 4k_{\mathrm{B}}GT^2\Gamma, \tag{4.98}$$

where $\kappa(T)$ is a thermal conductivity of substance that constructs thermal link. We define η as $\eta \equiv T_{\mathrm{bath}}/T$ and assume $\kappa(T) = \kappa(T_{\mathrm{bath}})\eta^{-(n-1)}$, then Γ is expressed as

$$\Gamma = \frac{n}{2n + 1}\frac{1 - \eta^{(2n+1)}}{1 - \eta^n}. \tag{4.99}$$

The current density of phonon noise is obtained by Equation (4.96) and (4.98)

$$\delta I_{\mathrm{ph}}^2 = \frac{4k_{\mathrm{B}}GT^2\Gamma}{V_{\mathrm{b}}^2}\left(\frac{\mathcal{L}_0}{\mathcal{L}_0 + 1}\right)^2 \frac{1}{1 + \omega^2\tau_{\mathrm{eff}}^2} = 4k_{\mathrm{B}}GT^2\Gamma|S_{\mathrm{I}}|^2. \tag{4.100}$$

On the other hand, the current fluctuations δI_{J}^0 by Johnson noise δV_{J} is

$$\delta I_{\mathrm{J}}^0 = \frac{\delta V_{\mathrm{J}}}{R}. \tag{4.101}$$

Out put fluctuation is calculated by the feedback circuit,

$$\delta I_\mathrm{J} = \frac{1}{1 + \mathcal{L}(\omega)} \delta I_\mathrm{J}^0, \tag{4.102}$$

$$= \frac{\frac{1}{\mathcal{L}_0 + 1} + i\omega\tau_\mathrm{eff}}{1 + i\omega\tau_\mathrm{eff}} \frac{\delta V_\mathrm{J}}{R}, \tag{4.103}$$

$$= \frac{1}{\mathcal{L}_0 + 1} \frac{1 + i\omega\tau_0}{1 + i\omega\tau_\mathrm{eff}} \frac{\delta V_\mathrm{J}}{R}. \tag{4.104}$$

The voltage density of Johnson noise is $\delta V_\mathrm{J}^2 = 4k_\mathrm{B}TR$ in $0 \leq f \leq \infty$ frequency space. Then, output current density is

$$\delta I_\mathrm{J}^2 = \frac{4k_\mathrm{B}T}{R} \left(\frac{1}{\mathcal{L}_0 + 1}\right)^2 \left|\frac{1 + i\omega\tau_0}{1 + i\omega\tau_\mathrm{eff}}\right|^2, \tag{4.105}$$

$$= \frac{4k_\mathrm{B}T}{R} \left(\frac{1}{\mathcal{L}_0 + 1}\right)^2 \frac{1 + \omega^2\tau_0^2}{1 + \omega^2\tau_\mathrm{eff}^2}, \tag{4.106}$$

$$= \begin{cases} \frac{4k_\mathrm{B}T}{R} \left(\frac{1}{\mathcal{L}_0 + 1}\right)^2 & \text{if } \omega \ll \tau_0^{-1} \\ \frac{4k_\mathrm{B}T}{R} & \text{if } \omega \gg \tau_\mathrm{eff}^{-1} \end{cases}. \tag{4.107}$$

$$\tag{4.108}$$

In the frequency range of $\omega \ll \tau_0^{-1}$, ETF prevents the Johnson noise. In the frequency range of $\omega \gg \tau_\mathrm{eff}^{-1}$, the output current density returns input value. The total current density δI is given to sum of squares of the Johnson noise and the phonon noise

$$\delta I^2 = \delta I_\mathrm{J}^2 + \delta I_\mathrm{ph}^2, \tag{4.109}$$

$$= \frac{4k_\mathrm{B}T}{R} \left(\frac{1}{\mathcal{L}_0 + 1}\right)^2 \frac{1 + \omega^2\tau_0^2}{1 + \omega^2\tau_\mathrm{eff}^2} + \frac{4k_\mathrm{B}GT^2\Gamma}{V_\mathrm{b}^2} \left(\frac{\mathcal{L}_0}{\mathcal{L}_0 + 1}\right)^2 \frac{1}{1 + \omega^2\tau_\mathrm{eff}^2}, \tag{4.110}$$

$$= \frac{4k_\mathrm{B}T}{R} \frac{\frac{1 + \alpha\Gamma\mathcal{L}_0}{(\mathcal{L}_0 + 1)^2} + \omega^2\tau_\mathrm{eff}^2}{1 + \omega^2\tau_\mathrm{eff}^2}. \tag{4.111}$$

The ration between the Johnson noise and the phonon noise clarify these relationship

$$\frac{\delta I_\mathrm{ph}^2}{\delta I_\mathrm{J}^2} = \frac{\alpha\Gamma\mathcal{L}_0}{1 + \omega^2\tau_0^2}. \tag{4.112}$$

From Equation (4.112), we find the Johnson noise is suppressed by the phonon noise in low frequency range, and in $\omega \gg \tau_\mathrm{eff}^{-1}$ the Johnson noise is main part of the total noise. The ration between a signal and the phonon noise is

$$\frac{\delta P_\mathrm{signal}^2}{\delta P_\mathrm{ph}} = \frac{2E^2}{4k_\mathrm{B}GT^2\Gamma}. \tag{4.113}$$

This relation is independent of frequency. This is why the signal and the phonon noise are same frequency dependence. Using Equation (4.65)and (4.106), Johnson noise is represented by the current responsively S_I

$$\delta I_\mathrm{J}^2 = \frac{4k_\mathrm{B}T}{R} \frac{b^2(1 + \omega^2\tau_0)}{\mathcal{L}_0^2} |S_\mathrm{I}|^2. \tag{4.114}$$

Intrinsic noise are expressed with current responsively

$$\delta I^2 = \frac{4k_{\mathrm{B}}T}{R}\frac{b^2(1+\omega^2\tau_0)}{\mathcal{L}_0^2}|S_{\mathrm{I}}|^2 + 4k_{\mathrm{B}}GT^2|S_{\mathrm{I}}|^2. \tag{4.115}$$

4.7 Digital Filter Process

We obtain pulse heights simply by getting the pulse height peak values. However, in this method, the TES cannot achieve the ideal energy resolution since the pulse shapes are changed by the noises. We apply the digital filter process to maximize the Signal-to-noise ratio in frequency domain. It is called optimal filter [45, 40].

4.7.1 Optimal Filter

We measure and record the current waveform by a single photon in time series. The measured pulse $D(f)$ is denoted by model pulse $M(f)$, pulse height $\mathcal{A}$ and noise $N(f)$

$$D(f) = \mathcal{A} \times M(f) + N(f). \tag{4.116}$$

The pulse height is obtained by least squares method to minimize the measured pulse and the model pulse,

$$\chi^2 \equiv \int_{-\infty}^{\infty} \frac{|D(f) - \mathcal{A} \times M(f)|^2}{|N(f)|} df. \tag{4.117}$$

The pulse height is calculated in the case of $\chi^2 = 0$,

$$\mathcal{A} = \frac{\int_{-\infty}^{\infty} \frac{DM^* + D^*M}{2|N|^2} df}{\int \frac{|M|^2}{|N|^2} df}. \tag{4.118}$$

$D(f)$ and $M(f)$ are Fourier components of a real function, these relations consist

$$D(-f) = D(f)^*, \ M(-f) = M(f)^*. \tag{4.119}$$

Using Equation (4.119), the numerator in $\mathcal{A}$ (Equation (4.118)) is

$$\int_{-\infty}^{\infty} \frac{D(f)M(f)^*}{2|N(f)|^2} df = -\int_{-\infty}^{\infty} \frac{D(-f)M(-f)^*}{2|N(f)|^2} df = \int_{-\infty}^{\infty} \frac{D(f)^*M(f)}{2|N(f)|^2} df. \tag{4.120}$$

Using Equation (4.118) is denoted as

$$\mathcal{A} = \frac{\int_{-\infty}^{\infty} \frac{DM^*}{|N|^2} df}{\int \frac{|M|^2}{|N|^2} df}, \tag{4.121}$$

$$= \frac{\int_{-\infty}^{\infty} \frac{D}{M}\left|\frac{M}{N}\right|^2 df}{\int \left|\frac{M}{N}\right|^2 df}. \tag{4.122}$$

$\mathcal{A}$ expresses the average value of the ration $D(f)/M(f)$ in the frequency space weight to $\left|\frac{M}{N}\right|^2$. Equation (4.122) is converted by inverse Fourier transform,

$$\mathcal{A} = \frac{\int_{-\infty}^{\infty} D(t)\mathcal{F}^{-1}\left(\frac{M(f)}{|N(f)|^2}\right)dt}{\int \left|\frac{M}{N}\right|^2 df} = \frac{\int_{-\infty}^{\infty} D(t)\mathcal{T}(t)dt}{\int \left|\frac{M}{N}\right|^2 df}, \tag{4.123}$$

$$\mathcal{T}(t) \equiv \mathcal{F}^{-1}\left(\frac{M(f)}{|N(f)|^2}\right). \tag{4.124}$$

We call $\mathcal{T}(t)$ as the template in optimal filter (Figure 4.7). The model pulse $M(f)$ is generated by applying the Fourier transform to an averaged pulse of a single line. The noise power $|N(f)|^2$ is generated by averaging the Fourier transformed noise spectrum. By correlating the template to all pulses, the scale factor give us the pulse height H by an input photon.

$$H = N \int_{-\infty}^{\infty} D(t)\mathcal{T}(t)dt, \tag{4.125}$$

where N is a normalized constant. In this filter, we assume that the every pulses are similar shape and energy scaled, and also pulse and noise are independent.

4.7.2   Energy Resolution

We define the Noise Equivalent Power (NEP) in frequency space with the current responsively $S_I(f)$ and noise power spectrum δI

$$\mathrm{NEP}(f) \equiv \left|\frac{\delta I(f)}{S_I(f)}\right|^2, \tag{4.126}$$

$$= \frac{4k_{\mathrm{B}}T}{R}\frac{b^2}{\mathcal{L}_0^2}\left(1 + (2\pi f)^2\tau_0^2 + \frac{\mathcal{L}_0^2}{b^2}RGT\Gamma\right), \tag{4.127}$$

$$= 4k_{\mathrm{B}}TP_{\mathrm{b}}\left(\frac{1 + (2\pi f)^2\tau_0^2}{\mathcal{L}_0^2} + \frac{\alpha\Gamma}{\mathcal{L}_0}\right). \tag{4.128}$$

The energy resolution obtained by $\mathrm{NEP}(f)$ is expressed [46]

$$\Delta E_{\mathrm{rms}} = \left(\int_0^{\infty} \frac{4}{\mathrm{NEP}^2(f)}df\right)^{-\frac{1}{2}}. \tag{4.129}$$

The intrinsic energy resolution is calculated by Equation (4.129) and (4.128),

$$\Delta E_{\mathrm{rms}} = \left(\int_0^{\infty} \frac{4}{\frac{4k_{\mathrm{B}}T}{R}\frac{b^2}{\mathcal{L}_0^2}\left(1 + (2\pi f)^2\tau_0^2 + \frac{\mathcal{L}_0^2}{b^2}RGT\Gamma\right)}df\right)^{-\frac{1}{2}}, \tag{4.130}$$

$$= \sqrt{\frac{4k_{\mathrm{B}}T}{R}\frac{b^2}{\mathcal{L}_0^2}\tau_0}\sqrt{1 + \frac{\mathcal{L}_0^2}{b^2}RGT\Gamma}, \tag{4.131}$$

$$= \sqrt{k_{\mathrm{B}}T^2C\frac{4b^2}{GTR\Gamma}}\sqrt{1 + \frac{\mathcal{L}_0^2}{b^2}RGT\Gamma}, \tag{4.132}$$
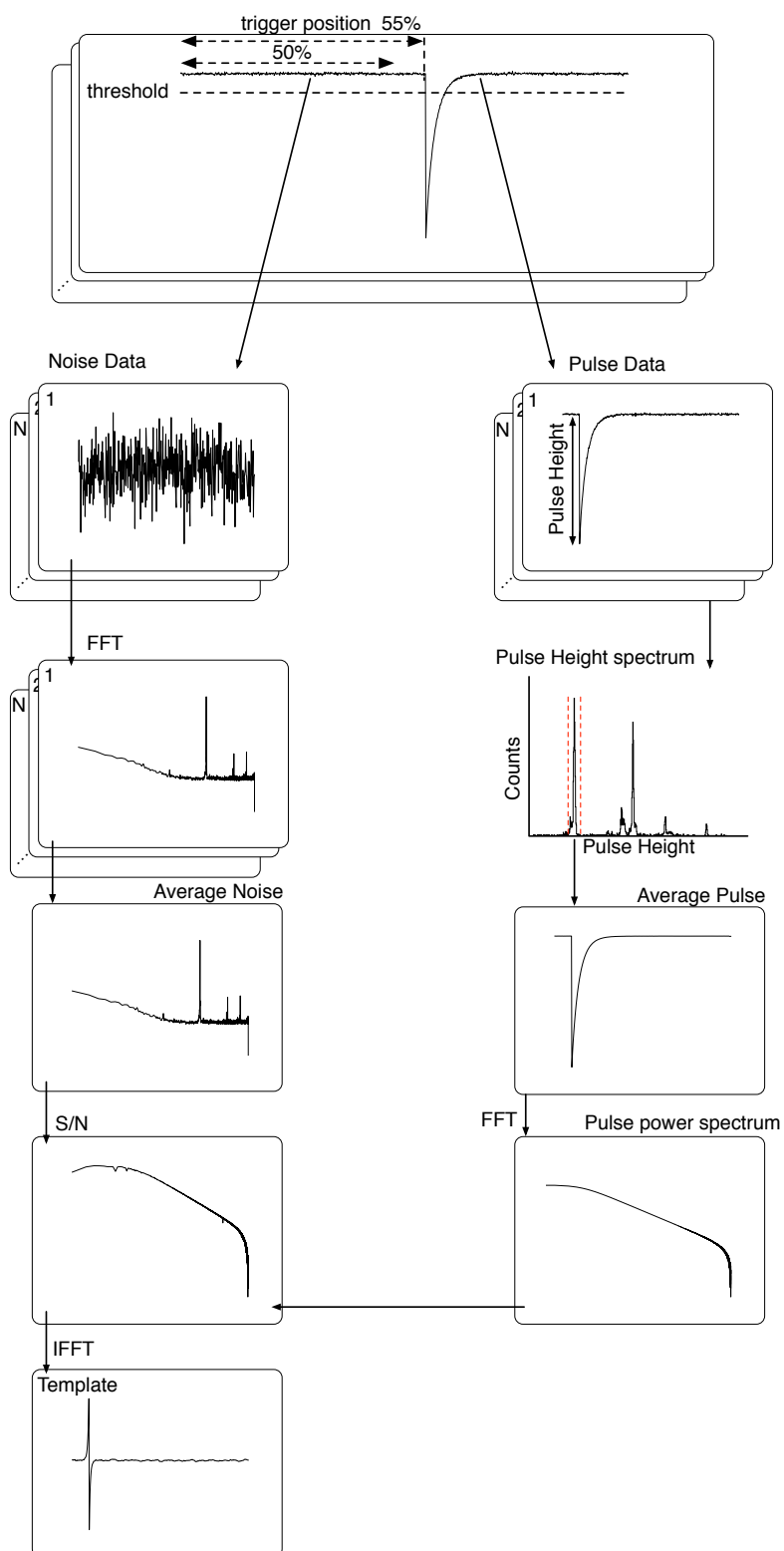
Fig. 4.7   Way of generating a template
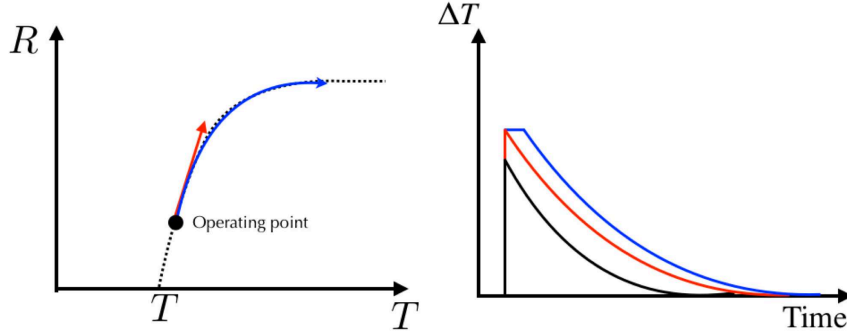
Fig. 4.8 $R - T$ relation (left) and pulse with saturation (right)

where we define ξ as a coefficient

$$\xi \equiv 2\sqrt{\frac{V^2}{GRT\mathcal{L}_0^2}}\sqrt{1 + \frac{\mathcal{L}_0^2}{V^2}RGT\Gamma}. \tag{4.133}$$

We represent energy resolution as Full width at Half Maximum (FWHM),

$$\Delta E_{\mathrm{FWHM}} = 2 \cdot \sqrt{2\ln 2}\Delta E_{\mathrm{rms}} = 2.35\xi\sqrt{k_{\mathrm{B}}T^2C}. \tag{4.134}$$

Using Equation (4.61), ξ is

$$\xi = 2\sqrt{\frac{1}{\alpha\mathcal{L}_0}}\sqrt{1 + \alpha\mathcal{L}_0\Gamma}. \tag{4.135}$$

In the case of the sufficiently low bath temperature ($T_{\mathrm{bath}} \ll T$), Γ, the joule heat power P_{b}, and loop gain $\mathcal{L}_0$ are approximated to $\Gamma \sim 1/2$, $P_{\mathrm{b}} \sim GT/n$, $\mathcal{L}_0 \sim \alpha/n$. Thus, the coefficient ξ is expressed to $\xi \simeq 2\sqrt{\sqrt{n/2}/\alpha}$.

4.8   TES Response in Non-linear Region

In the previous sections, we consider the TES microcalorimeter response in linear regime. However, the TES microcalorimeter has non-linearity in actual conditions and the energy resolution will degrade due to this non-linearity. There are three different causes of the non-linear response of the TES microcalorimeter : (1) temperature dependence of the heat capacity, (2) a non-linear $R - T$ relation of a TES, (3) deviation from a constant-voltage bias due to the bias scheme using a shunt resistance. For (1), we assume that the change of the temperature proportions to the incident energy (Equation (4.1)), but the heat capacity also changes with the temperature change, $C(T)$, thus the relation between the incident energy and the temperature is not a linear relation.

For the non-linearity of the $R - T$ relation (2), the non-linearity appears in the pulse shape regardless of the magnitude of the incident energy. In addition to this, when a TES calorimeter absorbs a high-energy photon, the operating point of TES may go over the transition edge and the pulse shape saturates and the time required to cool the TES back to its equilibrium becomes longer (Figure 4.8). The width of the transition edge is roughly

$$\Delta T_{\mathrm{edge}} \simeq \frac{T}{\alpha}. \tag{4.136}$$

Then the saturation energy E_{sat} is roughly approximated as

$$E_{\mathrm{sat}} = \frac{CT}{\alpha}. \tag{4.137}$$
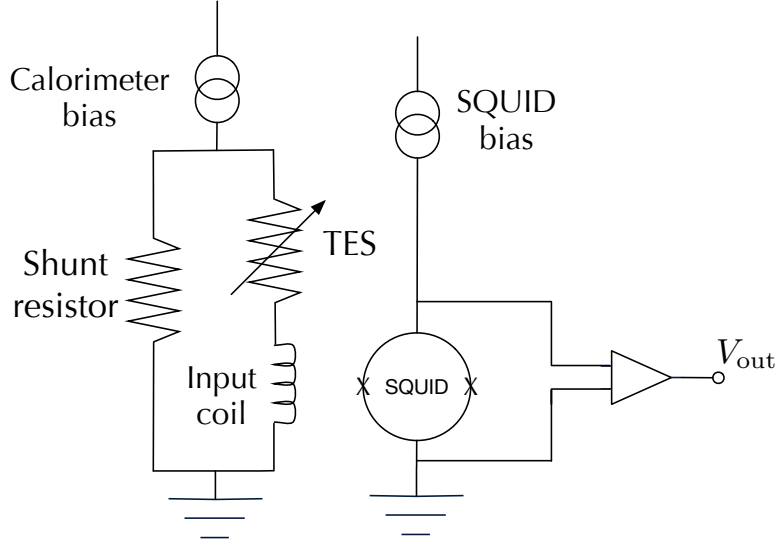
Fig. 4.9   Readout system of TES microcalorimeter using SQUID. We apply pseudo constant-voltage bias using shunt resistor.f

The ideal energy resolution is given by

$$\Delta E \simeq 2.35 \xi \sqrt{k_\mathrm{B} T E_\mathrm{sat}}, \tag{4.138}$$

We need to set E_sat higher than the maximum energy of interest e.g. $E_\mathrm{sat} = 100$ keV for the present case. The energy resolution is approximately constant for $E \ll E_\mathrm{sat}$ determined by Equation (4.138) and degrades rapidly when E approaches E_sat. Fixen et al.[47] reported an improvement method that generates the templates for each lines to recover the energy resolution near or over the E_sat. They showed that the energy resolution can be recovered to

$$\Delta E \simeq 2.35 \xi \sqrt{k_\mathrm{B} T E}. \tag{4.139}$$

For (3), since the voltage applied to the TES varies as the resistance changes, the constant voltage bias does not hold and the resistance is a function of the current and the temperature $R(T, I)$. Bandler et al.[48] reported a method to correct for (3) by converting the TES current to the TES resistance before applying the optimal filtering. Since the TES and the shunt resister (R_s) are connected in parallel, the TES current at the bias point (I_0) is expressed as

$$I_0 = \frac{R_\mathrm{s}}{R_\mathrm{s} + R_0} I_\mathrm{b}, \tag{4.140}$$

where I_b is the bias current and R_0 is the resistance of the TES at the bias point. If the current changes by minute amount ΔI, the change of the resistance is calculated by

$$\Delta R = -(R_0 + R_\mathrm{s}) \frac{\Delta I}{I_0 + \Delta I}. \tag{4.141}$$

Thus we can use ΔR instead of ΔI as the pulse record data for the pulse height analyzed value (PHA) analysis using an optimal filter.
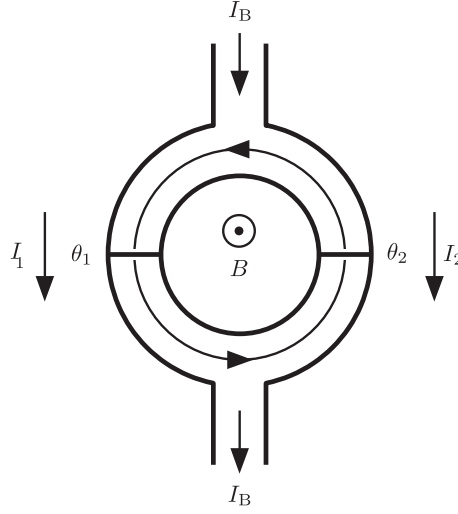
Fig. 4.10   Schema of dc-SQUID

4.9   Readout System using SQUID

The current change of TES is very small, so that change should be read out by a low impedance ammeter. Figure 4.9 is shown the readout system of TES microcalorimeter using SQUID(Superconducting QUantum Interference Device) as an ammeter [49].

4.9.1   Dc-SQUID

The dc-SQUID is a device using the Josephson effect and made of two parallel Josephson junction (Figure 4.10). The relation between a phase difference of two junctions and magnetic flux consists following equation

$$\theta_2 - \theta_1 = 2\pi\frac{\Phi}{\Phi_0}, \tag{4.142}$$

where, θ_1 and θ_2 are phase difference of two junctions respectively, Φ is the magnetic flux penetrating the ring, and Φ_0 is the flux quantum. The value of the flux quantum is

$$\Phi_0 = h/2e = 2.06 \times 10^{-15} \text{ Wb.} \tag{4.143}$$

When the Josephson junction is superconducting, the bias current I_B is written by

$$I_B = I_0 \cos\left(\pi\frac{\Phi_{\text{exp}}}{\Phi_0}\right)\sin\left(\theta_1 - \pi\frac{\Phi_{\text{exp}}}{\Phi_0}\right), \tag{4.144}$$

where I_0 is the critical current of the junction, $\Phi_{\text{exp}} \equiv \Phi - LJ$ is the external magnetic flux. L and J are the self-inductance and the current that goes through the ring. The critical current to keep SQUID in superconducting state is

$$I_{\text{max}} = 2I_0\left|\cos\left(\pi\frac{\Phi_{\text{exp}}}{\Phi_0}\right)\right|. \tag{4.145}$$

The critical current of SQUID changes periodically with external magnetic flux. When we operate SQUID by larger bias current than $2I_0$, the change of the critical current makes output voltage change according to change
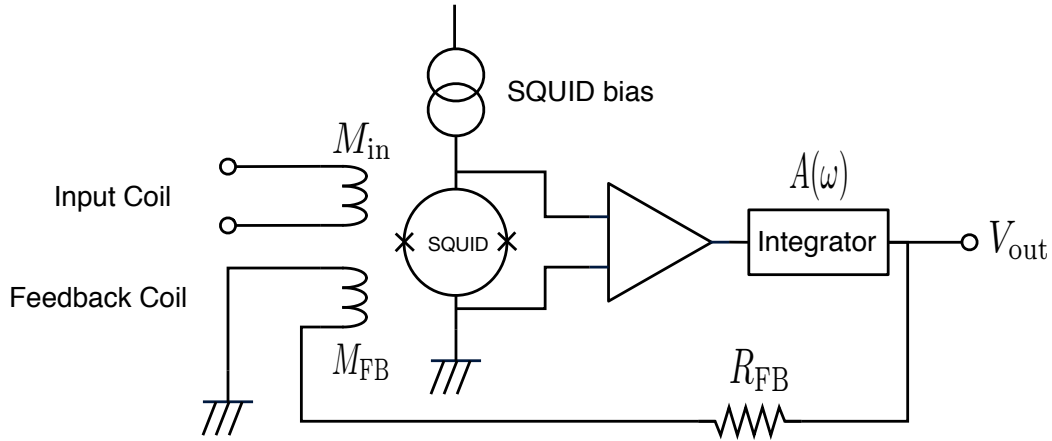
Fig. 4.11   Schematic diagram of Flux-Locked Loop

of external magnetic flux. We set coil next to SQUID and input the external magnetic flux to SQUID then, we deal SQUID as a high sensitivity ammeter.

4.9.2   Flux-locked Loop

By the periodical change of SQUID, a linear response between input and output is limited in the range of $\pm 1/4\Phi_0$. If the operating point of SQUID goes over the range, the gain changes largely and SQUID doesn't work as the ammeter. To keep the linear response, SQUID is operated under the negative feedback and the magnetic flux that goes through SQUID is limited. This method is called Flux-Locked Loop (FLL), by keeping a constant magnetic flux in SQUID.

4.9.3   Responsibility of Flux-Locked Loop

The diagram of FLL is shown in Figure 4.11. The current flows in input coil which is magnetically connected with SQUID input the SQUID loop as a magnetic flux, Φ_{in}, by the mutual inductance, M_{in}, between input coil and SQUID. The magnetic flux inputed in SQUID is converted to the voltage by a SQUID-gain, V_Φ, and amplified by a room temperature circuit. The part of output is converted to the current by feedback resistance, R_{FB}, and the current is fed back to SQUID by mutual inductance, M_{FB}, between the feedback coil and SQUID as a magnetic flux, Φ_{FB}. The loop gain of the FLL circuit is

$$\mathcal{L}(\omega) = V_\Phi \frac{A(\omega)}{R_{\mathrm{FB}}} \frac{M_{\mathrm{FB}}}{\Phi_0}. \tag{4.146}$$

The actual input magnetic flux is written as

$$\Phi_{\mathrm{in}} - \Phi_{FB} = \frac{\Phi_{\mathrm{in}}}{1 + \mathcal{L}(\omega)}, \tag{4.147}$$

by feedback. We regard SQUID operating feedback as a transimpedance amplifier that converts current to voltage. The current-voltage coefficient Ξ is

$$\Xi = \frac{V_{\text{out}}}{I_{\text{in}}}, \tag{4.148}$$

$$= \frac{\mathcal{L}(\omega)}{1 + \mathcal{L}(\omega)} \frac{M_{\text{in}}}{M_{\text{FB}}} R_{\text{FB}}, \tag{4.149}$$

$$\simeq \frac{M_{\text{in}}}{M_{\text{FB}}} R_{\text{FB}}. \tag{4.150}$$

We use $\mathcal{L} \gg 1$ for Equation (4.150). The current-voltage coefficient is consisted by mutual inductances and feedback resistance.

4.9.4   Band width of SQUID operating FLL

The output of SQUID is a periodic function. If the actual input is larger than $\pm \Phi_0/4$, FLL doesn't hold because a plus and minus sign of the SQUID gain are reversed. This is called Flux jump. The maximum input quantity is determined by loop gain. The relation between limited input quantity and loop gain is

$$\frac{1}{1 + \mathcal{L}(\omega)} \Phi_{\text{in}} < \frac{1}{4} \Phi_0. \tag{4.151}$$

In the range of Equation (4.151), SQUID operates stably under FLL, and the responsibility according to input holds linearity.

4.9.5   SQUID array

We use SQUID array to amplify the signal in low temperature stage. SQUID array is composed by large input coils connected in series and large SQUIDs connected with these input coils. Connecting a few 10 or more SQUIDs in series, and the signal is amplified with operating SQUID in a same phase. To select the SQUID array, we get the low readout noise because of amplifying the signal at low temperature and we can easily achieve the impedance matching to a SQUID circuit and room temperature circuit. In this thesis, we used the SQUID array designed in our laboratory [50] and fabricated in the Clean Room for Analog-digital superconductiVITY (CRAVITY) .

4.10   TES Resistance Operating with SQUID

We obtain the resistance of TES when we readout with SQUID. The relation between a current flowing in the TES I_{tes} and voltage applied to SQUID V_{out} is

$$V_{\text{out}} = \Xi I_{\text{tes}}. \tag{4.152}$$

The circuit equation in the TES and shunt resistance is written by

$$I_{\text{b}} = I_{\text{tes}} + I_{\text{s}}, \tag{4.153}$$

$$R_{\text{tes}} I_{\text{tes}} = R_{\text{s}} I_{\text{s}}, \tag{4.154}$$

where $I_{\rm b}$ and $I_{\rm s}$ are respectively the bias current and the current flowing in the shunt resistance and $R_{\rm tes}$ and $R_{\rm s}$ are respectively resistance of the TES and resistance of shunt. Thus, the resistance of the TES is expressed as

$$R_{\rm tes} = \frac{I_{\rm b} - I_{\rm tes}}{I_{\rm tes}} R_{\rm s}. \tag{4.155}$$

Using $V_{\rm out}$, the resistance of the TES is rewritten by

$$R_{\rm tes} = \left(\frac{\Xi}{V_{\rm out}} I_{\rm b} - 1 \right) R_{\rm s}. \tag{4.156}$$

Chapter 5

Development of New Calibration Method for Radio Isotope and Improvement of Non-linear Response to Energy

5.1   Problems of Obtaining PHA-center with Radio Isotopes

In our TES-Thorium project, we will determine small difference in two nuclear transition lines of ^{229}Th with two methods. One method requires a high accuracy in energy calibration. If we use monochromatic lines for calibration, we can easily correlate the PHA (Pulse Height Analyzed value by optimum filtering) with the energy. However if we use atomic or nuclear lines from isotopes or from X-ray/particle-induced X-ray emission, we have to conduct rather complex analysis to obtain accurate calibration, because the emission contains fine structure which our detector can only partly resolve. In previous analysis, we estimated the centroid PHA value of the line complex from the average of PHA values of events within a PHA range which include the line complex. We then related it with the weighted mean of the theoretical fine-structure line. Since the PHA-centroid-value will be dependent on the PHA range we estimate the average, the choice of the range introduces systematic error in calibration. Thus we developed a new analysis method for radio isotopes [51].

5.2   Experimental Setup

In order to study the calibration method, we carried out the X-ray irradiation test in a wide energy band $(3.3 - 17.8 \text{ keV})$ by using ^{45}Ca, ^{55}Fe, and ^{241}Am isotopes simultaneously with several line complex to obtain a continuum-free line spectra. Total integration time of the present experiment was 7 days and we obtained 8205 events in K Kα line from ^{45}Ca. We designed the detector stage on which attached the TES microcalorimeter and jig that attaches ^{45}Ca, ^{55}Fe, and ^{241}Am radio isotope. We fabricated the detector stage by ourselves. And we asked JAXA machine shop to fabricate the jig. Figure 5.2 shows the detector stage and three radio isotopes. The intensities of three radio isotope are respectively 0.003 Bq, 103 kBq, and 2.93 kBq for ^{45}Ca, ^{55}Fe, and ^{241}Am(Table 5.1). Fine structures of lines from ^{45}Ca, ^{55}Fe, and ^{241}Am radio isotope that we used in this experiment are summarized in Table 5.4.

Table 5.1 Intensity of isotope in ISAS experiment

Isotope	Intensity	Unit
^{45}Ca	0.003	Bq
^{55}Fe	103	k Bq
^{241}Am	2.93	k Bq

Table 5.2 Detailed parameters of a single TES microcalorimeter of 64-pixel array

Components	Material	Item	Unit	Measured results
TES	Ti/Au	Size	μm^2	180×180
		Thickness	nm	40/108
Electrode wiring	Al	Width	μm	10
		Pitch	μm	10
		Thickness	nm	120
Absorber	Au	Size	μm^2	120×120
		Thickness	μm	3.9
Membrane	SiNx	Size	μm^2	300×300
		Thickness	μm	1.0

Table 5.3 Measured and calculated performance parameters of a 64-pixel array TES

		Unit	Values
Transition energy	T_c	mK	162
Heat capacity	C	pJ/K	0.7
Ideal energy resolution	ΔE	eV	4
Saturation energy	E_{sat}	keV	7.5

Table 5.4 Line complex in ^{45}Ca, ^{55}Fe, and ^{241}Am radio isotope

Radio isotope	Complex line	Fine structures
^{45}Ca	K K$_\alpha$ complex	K$_{\alpha 1}$, K$_{\alpha 2}$
	K K$_\beta$ complex	K$_{\beta 1}$, K$_{\beta 3}$, K$_{\beta 1,3}$*1, $K_{\beta 5}$*2
^{55}Fe	Mn K$_\alpha$ complex	K$_{\alpha 1,2}$, K$_{\alpha 1,3}$, K$_{\alpha 1,4}$, K$_{\alpha 1,5}$, K$_{\alpha 2,1}$, K$_{\alpha 2,2}$
	Mn K$_\beta$ complex	K$_{\beta 1}$, K$_{\beta 3}$, K$_{\beta 3,1}$
^{241}Am	Np L$_{\alpha 1}$ + satellites	L$_{\alpha 1}$, satelitte1*2,satelitte2*2,satellite3*2, satellite4*2
	Np L$_{\beta 1}$+L$_{\beta 3}$	L$_{\beta 1}$, L$_{\beta 2}$

5.2.1 TES microcalorimeter

We fabricated a TES microcalorimeter array for this experiment based on the design developed for the STEM (Scanning Transmission Electron Microscope)-TES project[52]. For this project, we developed an 8×8 format, 64-pixel array [53](Figure 5.1). The size of the TES and the X-ray absorber were, respectively, 180×180 μm^2 and 120×120 μm^2. The thickness of the absorber was 3.9 μm. Then the saturation energy, E_{sat}, is estimated to be 7.5 keV for $C = 0.7$ pJ/K and $\alpha = 100$. The geometry, measured, and calculated performance parameters are listed in Table 5.2 and Table 5.3.
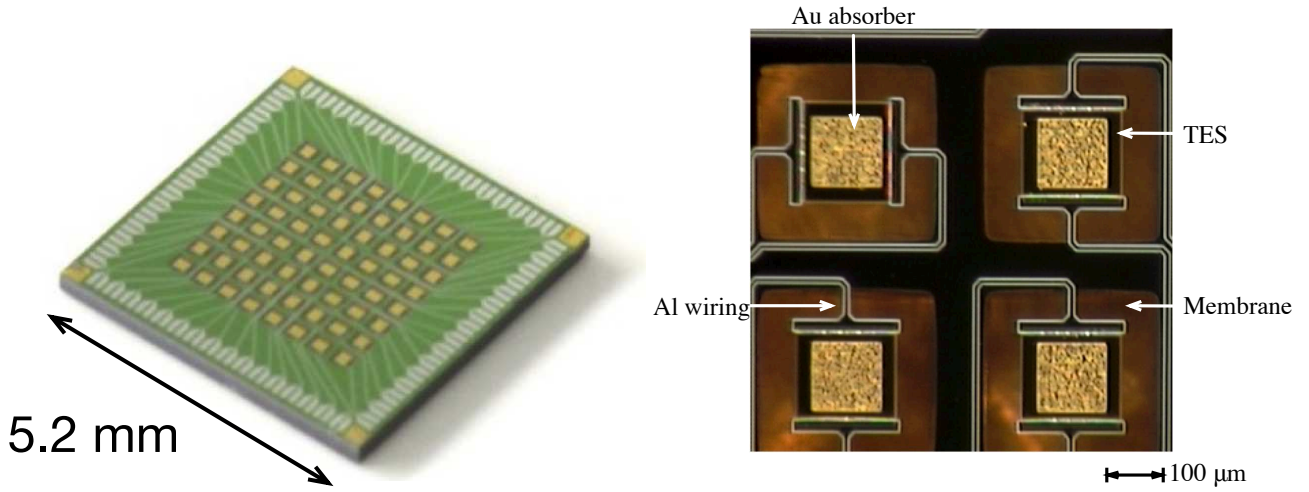
Fig. 5.1 64-pixel TES microcalorimeter array(left) and micrograph of fabricated TES microcalorimeter (right)
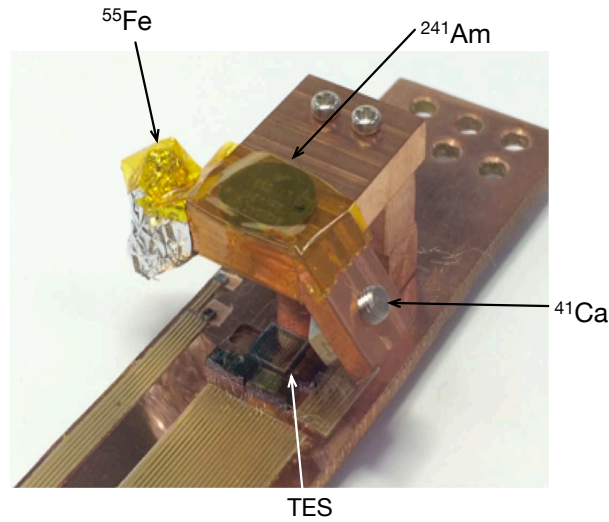
Fig. 5.2 Detector stage setup with ^{45}Ca,^{55}Fe,^{241}Am radio isotope

5.2.2 Data Acquiring Method

Figure 5.3 shows the readout schematic. The SQUID which reads out the TES was measured using Magnicon XXF-1. The analog signals from the SQUID amplifier was transmitted to the oscilloscopes, PicoScope 4224, through the Magnicon XXF-1 includes a preamplifier, an integrator, a flux-locked loop resistor, and a post amplifier. We acquired the pulse events using a trigger mode. A data length was fixed at 1 ms, and we took the first half 0.5 ms as the noise data and next half 0.5 ms as the pulse data. We set the sampling rate, the bit resolution, and the input voltage range as 40 MS/s, 15 bit, and ± 2 V.
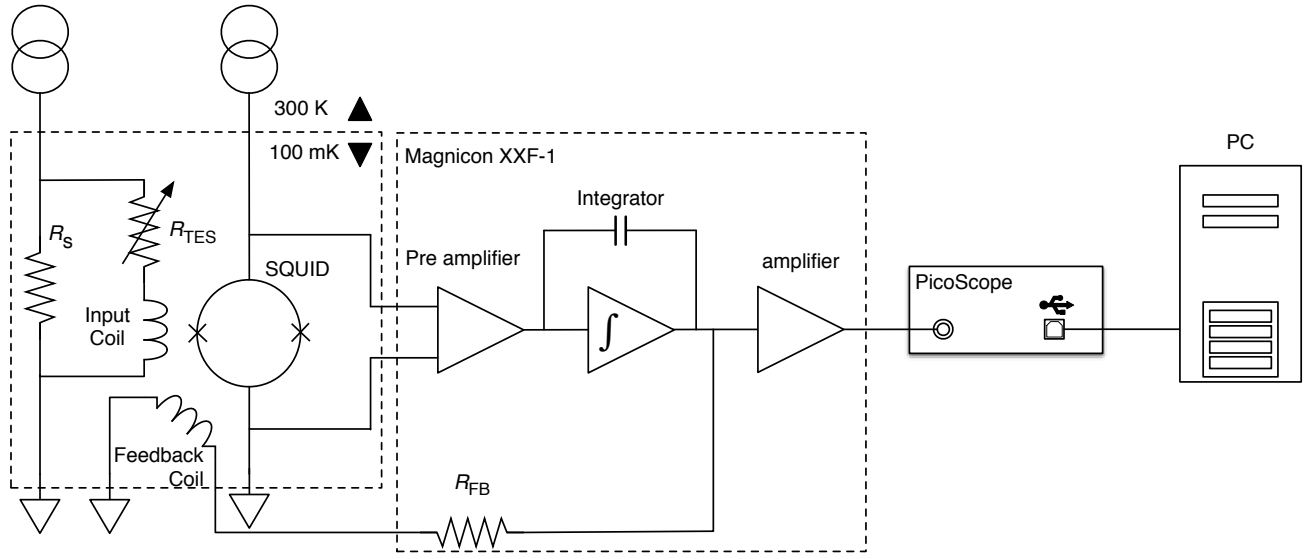
Fig. 5.3   Readout diagram of signal

Table 5.5   Parameter values determined by PHA spectrum fitting

Line	Main peak energy (keV)	FWHM (a.u.)	a (a.u./eV)	b (a.u.)
K K$_\alpha$	3.31380	$4.31^{+0.18}_{-0.17}$	$1.0021^{+0.0001}_{-0.0049}$	$-5.8^{+0.1}_{-0.7}$
K K$_\beta$	3.59149	$3.27^{+0.62}_{-0.65}$	$0.9956^{+0.018}_{-0.0024}$	$-13.3^{+0.2}_{-0.1}$
Mn K$_\alpha$	5.89885	$3.90^{+0.10}_{-0.25}$	$0.8000^{+0.00002}_{-0.00001}$	$844.6^{+0.2}_{-0.1}$
Mn K$_\beta$	6.49089	$3.38^{+0.36}_{-0.42}$	$0.6249^{+0.0000}_{-0.0004}$	$1976.1^{+0.1}_{-0.6}$
Np L$_{\alpha 1}$+ satellites	13.94426	$6.90^{+2.09}_{-2.28}$	$0.5993^{+0.0012}_{-0.0013}$	$2052.7^{+0.6}_{-0.7}$
Np L$_{\beta 1}$ + Np L$_{\beta 3}$	17.75020	$5.25^{+1.37}_{-1.67}$	$0.3202^{+0.0001}_{-0.0000}$	$6161.4^{+0.8}_{-0.5}$

5.3   New Calibration Method for PHA Spectrum

First, we applied the optimal filtering to TES-signal in the current space to determine the PHA. Since we have obtained a largest number of events in K K$_\alpha$, we made the template for optimal filtering by using the K K$_\alpha$ line (Figure 5.4). We then obtained PHA by applying the template to each pulse event (Figure 5.4). We normalized the PHA so that the PHA at the peak of K K$_\alpha$ line in PHA spectrum was 3313.8, which is the centroid energy of K K$\alpha 1$. From the PHA spectrum, we would like to obtain the centroid value of PHA which corresponds to a centroid energy of an X-ray line. It is not easy to obtain the PHA, for example K K$_{\alpha 1}$, because the K K$_{\alpha 1}$ line is strongly linked with the K K$_{\alpha 2}$ line. In order to determine the PHA value of K K$_{\alpha 1}$, the line model function within the fine structure of the line is needed. We begin from a line model function in the energy space

$$f(E) = \sum_{i=1}^{n} r_i L(E - E_{c,i}, \; \Gamma_i),\tag{5.1}$$

where L is the Lorentzian function and E is the energy. n is the number of fine structure lines, and r_i, $E_{c.i}$ and Γ_i are the relative intensity, the center energy, and the natural width of the-ith fine structure line. We used the values of r_i, $E_{c,i}$, and Γ_i referred in [54]. When we perform the model-fit in the only narrow range

---

[*1] Natural width not found in literature
[*2] Natural width and intensity ration not found in literature
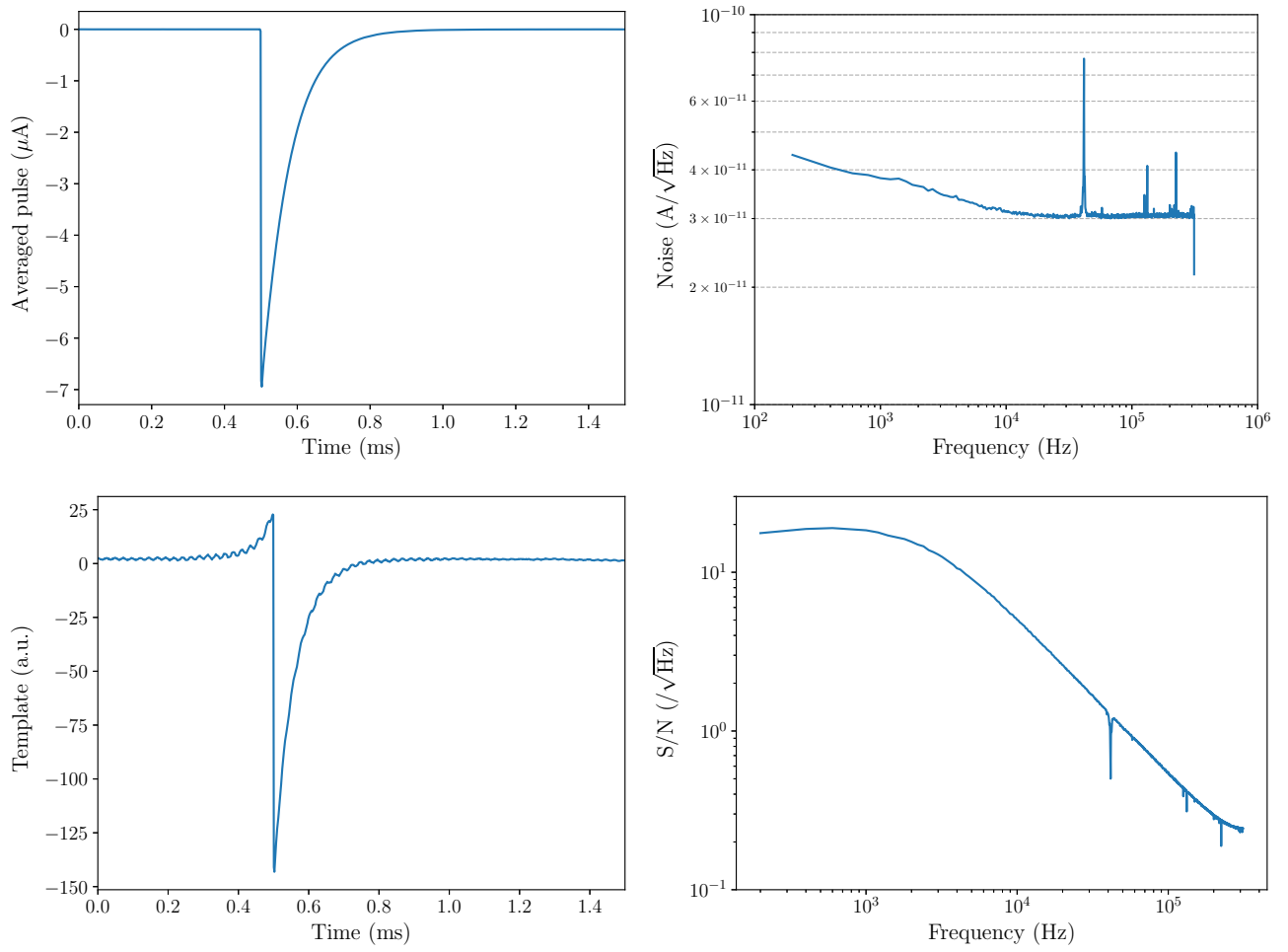
Fig. 5.4   Analysis results in the current pulses: the averaged pulse of K K$_\alpha$ (top left), the noise spectrum (top right), the template (bottom left), the signal to noise ration (bottom right).
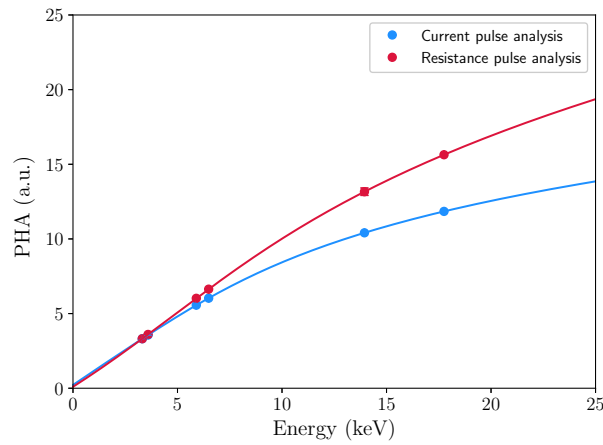
Fig. 5.5   Relation between PHA and energy for the six lines: K K$_\alpha$, K K$_\beta$, Mn K$_\alpha$, Mn K$_\beta$, Np L$_\alpha$, and Np L$_\beta$ of the current pulse and the resistance pulse analysis fitted by fourth order polynomial function.
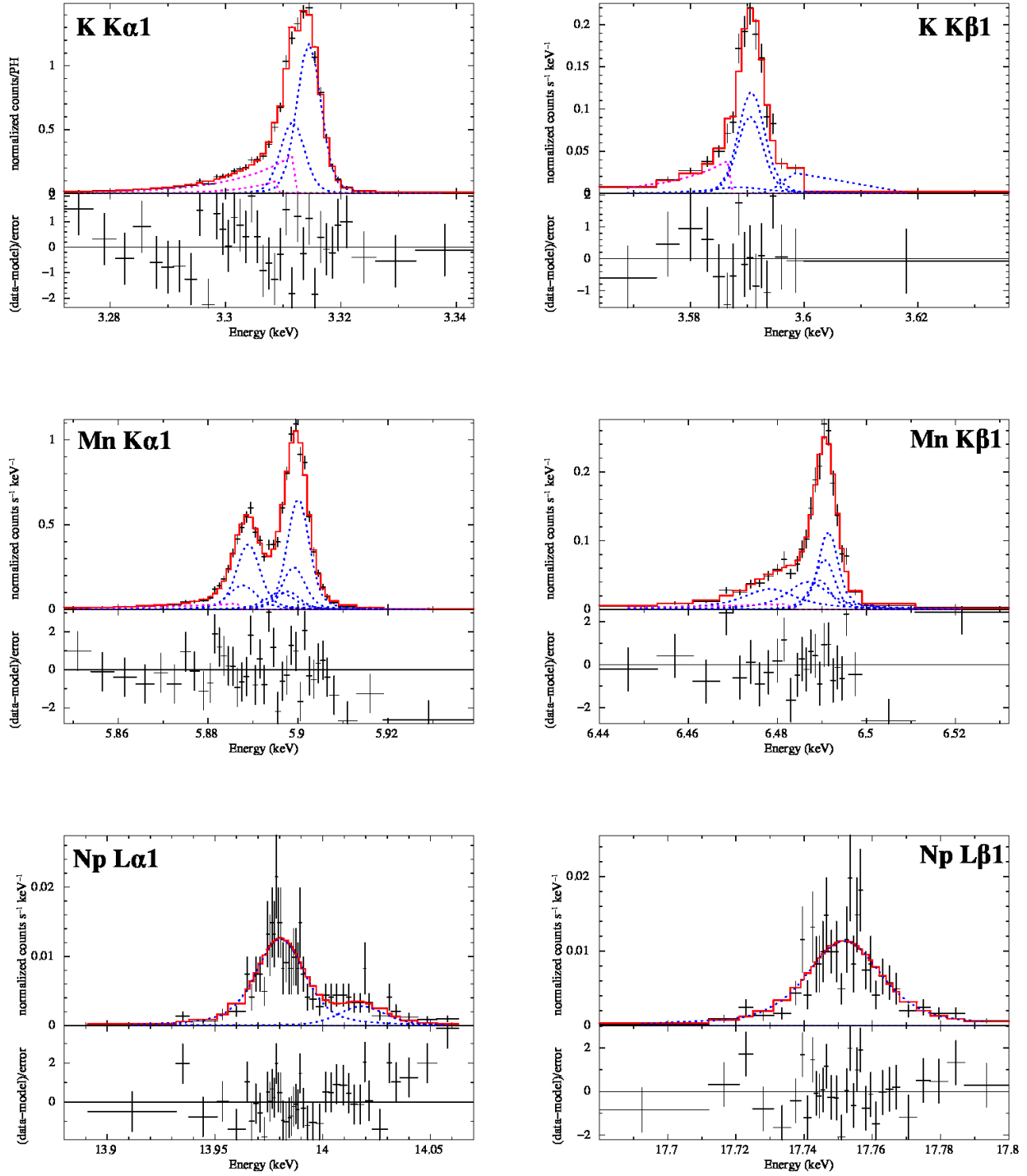
Fig. 5.6   Energy spectra of six line complexes and best fit models of the current pulse analysis

of PHA spectrum including line complex, the PHA to energy relation can be assumed to be a linear relation; $PHA = aE + b$. Then we can express the model function $F(p)$ in PHA space as

$$F(p) = N \sum_{i=1}^{n} \sum_{j} G(p - p_j, \ \sigma) r_i L(p_j - p_c(E_c), \ \Gamma_p(\Gamma_i)), \tag{5.2}$$

where p is the PHA, N is the normalization factor, p_c and Γ_p are respectively converted values from energy. We used a Gaussian function, G, as a line-spread function of the detector and convolved with Lorentzian function, L, that is the intrinsic line shapes. The Gaussian function and Lorentzian function is

$$G(x; \sigma) = \frac{1}{\sigma \sqrt{2\pi}} \exp\left(-\frac{x^2}{2\sigma^2}\right), \quad L(x; \Gamma) = \frac{\Gamma}{2\pi} \frac{1}{x^2 + (\Gamma/2)^2}. \tag{5.3}$$

Then, we performed six model fits for six line complexes. For most of all fine structures, the values of r_i, $E_{c,i}$ and Γ_i are known in literature, so the free parameters in Equation (5.2) are a, b, N, and σ. If some of the values are not known, we included them as free parameters. We employed the maximized likelihood method assuming the Poisson statistics. From the residual of the fits (=data-model), we found that the PHA spectra includes an excess low tail for K and Mn lines. This tail is a part of the response of the detector. Thus we added the following term in the model function,

$$F_{\text{tail}}(p) = u \sum_{i=1}^{n} r_i \exp\left(-\frac{p_i - p}{w}\right) \theta(p_i - p) \qquad \theta = \begin{cases} \theta = 1 & p_i - p \geq 0 \\ \theta = 0 & p_i - p < 0 \end{cases} \tag{5.4}$$

where $\theta(p)$ is the Heaviside step function. u and w are obtained by the model fits. We did not add this tail model for NpLα and NpLβ. We show the best fit values of a, b, and FWHM (Full Width Half Maximum) instead of the Gaussian sigma in Table 5.5. We estimated the statistical errors of fit parameters using log-likelihood. We set $\mathcal{L}$ as the likelihood and define $C = -2 \ln \mathcal{L}$. Wilk's theorem state that $\Delta C = C_{\text{ture}} - C_{\text{min}}$ follows χ^2 distribution with degrees of freedom that equal to the number of free parameters. We calculated the error of 90 % confidence level corresponds to $\Delta C = 2.706$.

The PHA for energy $E_{c,1}$ is obtained by using the function $PHA_1 = aE_{c,1} + b$ for each six lines. In Figure 5.5, the relation between PHA and energy is shown and from this relation, we found that the polynomial function with fourth order represents the experimental data well. We converted the PHA of all the events to energy equivalent value which is called Pulse Invariant (PI) using by the fitted polynomial function with fourth order. We generated a spectrum in the PI space (Figure 5.7) and fitted the six line complexes with a model function similar to Equation (5.2) and (5.4). In the PI space, the response to energy is assumed to be linear, we set $a = 0$, $b = 0$ in the equation $PHA = aE + b$, then set $E_{c,i}$ as a free parameter for the centroid value of the PI spectrum. Figure 5.6 shows the six line complexes spectrum and best fit model. We summarized the results in Table 5.6.

5.4 Pulse analysis using TES resistance

In the previous section, we analyzed the current pulse of the TES and found the non-linearity. We converted the current change to the resistance change using Equation (4.141) to improve the non-linearity and performed same procedure. The analysis results in the resistance pulses are shown in Figure 5.8. We fitted the PHA-to-energy relation with a fourth order polynomial function and converted to PI spectrum. The energy calibration curve becomes more close to linear than that of the current pulse (Figure 5.5). Then, the model fitted to the energy
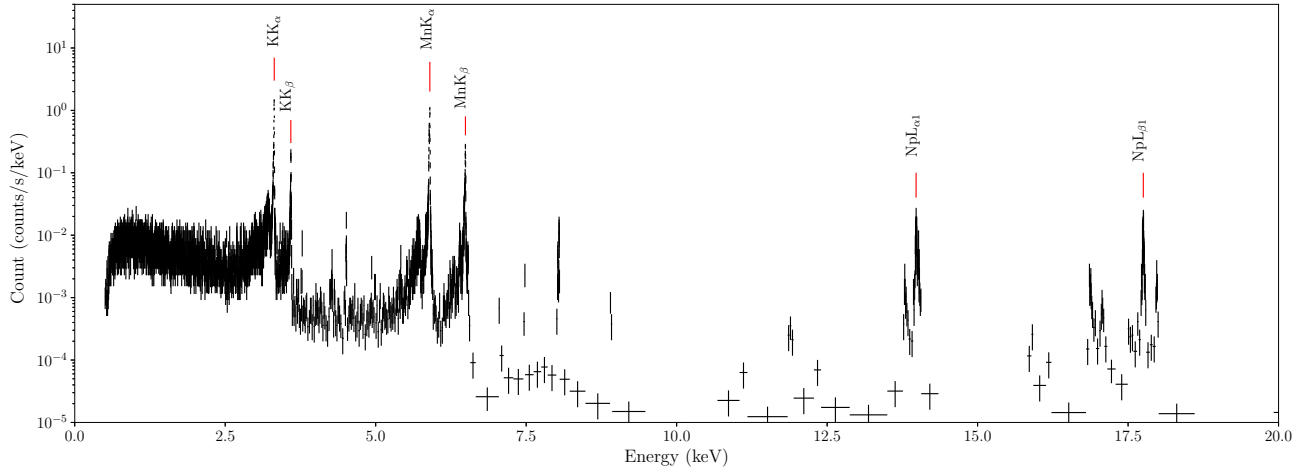
Fig. 5.7   Energy spectrum in the current pulses

Table 5.6   Energy-calibration accuracy and the energy resolution of lines by model fits of the PI spectra

Line	Main peak energy (keV)	Current pulse analysis		Resistance pulse analysis	
		Main peak $PI - E$ (eV)	FWHM (eV)	Main peak $PI - E$ (eV)	FWHM (eV)
K K_α	3.31380	$4.67^{+0.10}_{-0.20}$	$4.58^{+0.23}_{-0.18}$	$2.26^{+0.13}_{-0.06}$	$4.78^{+0.20}_{-0.21}$
K K_β	3.59149	$4.22^{+0.28}_{-0.71}$	$6.53^{+0.61}_{-0.60}$	$-1.59^{+0.30}_{-0.16}$	$5.58^{+0.57}_{-0.52}$
Mn K_α	5.89885	$2.40^{+0.21}_{-0.07}$	$4.58^{+0.20}_{-0.20}$	$-0..30^{+0.16}_{-0.09}$	$5.11^{+0.22}_{-0.27}$
Mn K_β	6.49089	$-0.56^{+0.22}_{-0.16}$	$3.93^{+0.53}_{-0.53}$	$1.27^{+0.23}_{-0.24}$	$4.07^{+05.2}_{-0.52}$
Np $L_{\alpha1}$ + satellite	13.94426	$11.74^{+2.01}_{-1.24}$	$14.41^{+5.05}_{-4.03}$	$-0.56^{+1.74}_{-1.72}$	$16.13^{+6.25}_{-5.07}$
Np $L_{\beta1}$	17.75020	$1.80^{+1.59}_{-1.60}$	$16.20^{+5.28}_{-5.09}$	$1.80^{+1.74}_{-1.79}$	$20.92^{+4.74}_{-6.65}$

spectra was carried out. The fluctuation of the centroid energy was within ±2 eV for the resistance pulses, although it was within ±12 eV for the current pulses (Table 5.6).
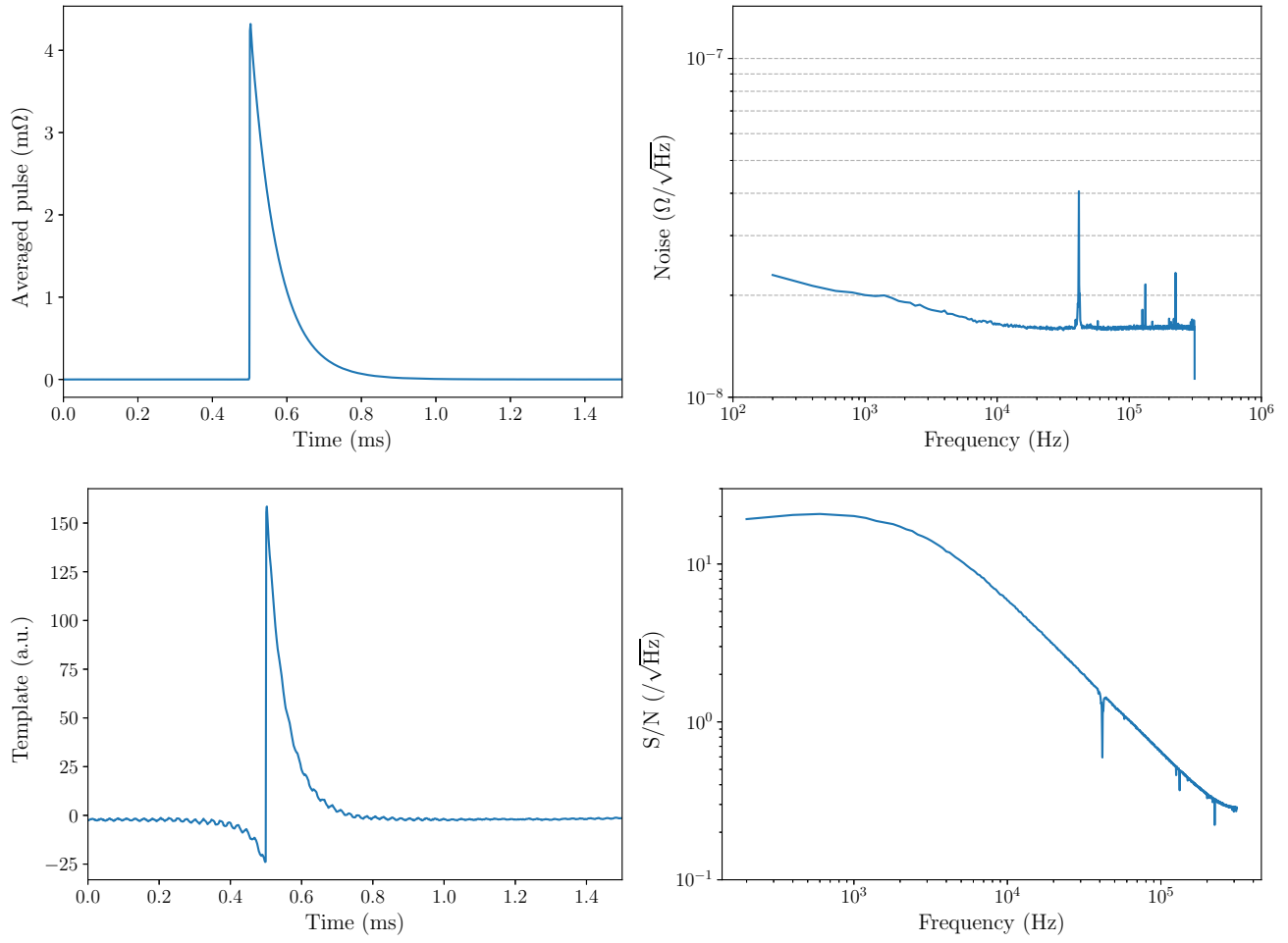
Fig. 5.8 Pulse collection results in the resistance pulses: the averaged pulse of K K$_\alpha$ (top left), the noise spectrum (top right), the template (bottom left), the signal to noise ration (bottom right).

Chapter 6

Measurement Lowest-energy of ^{229}Th Isomeric State at JAEA in Oarai

6.1 TES Detector

6.1.1 Parameter Optimizations and TES Designs

First of all, we designed a TES microcalorimeter for measurement of 30 keVγ $-$ ray. There are several parameters that determine the performance of TES detectors, e.g. the heat capacity C, the transition temperature T, the thermal conductivity G, the temperature sensitivity α. However, we can only easily vary two parameters; C and T. In order to optimize C and T that satisfy saturation energy (E_{sat}) above 40 keV and 10 eV energy resolution (ΔE), we estimated the dependence of the saturation energy and the energy resolution on the heat capacity and the transition temperature. Figure 6.1and 6.2 show the results of these estimation. In this estimation, we use $\alpha = 100$ from previous experiments. From those figures, we selected those parameter values; the heat capacity of 4.0 pJ/K and the transition temperature of 150 mK. The heat capacity is mainly determined by the thickness and the size of absorbxer. We set the thickness to 4 μm that was the maximum value of our fabrication process. We then determined the absorber size with the conditions of $C = 4.0$ pJ/K and 4.0 μm thickness. The specific
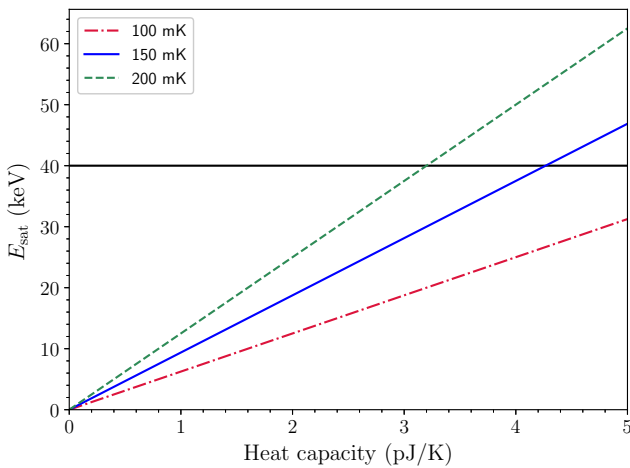
Fig. 6.1　Saturation energy vs. Heat capacity   Fig. 6.2　Energy resolution vs. Heat capacity
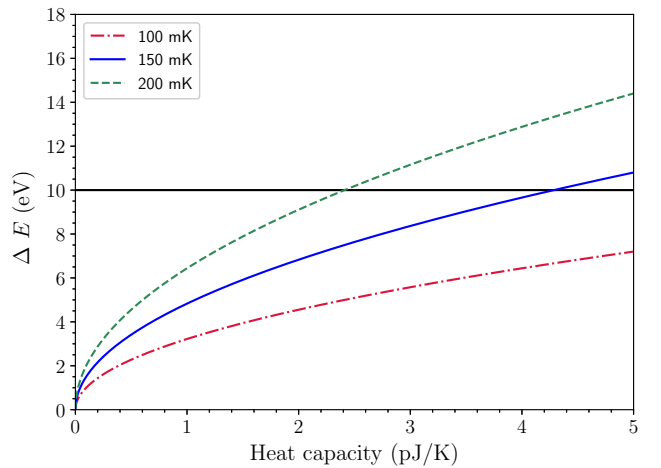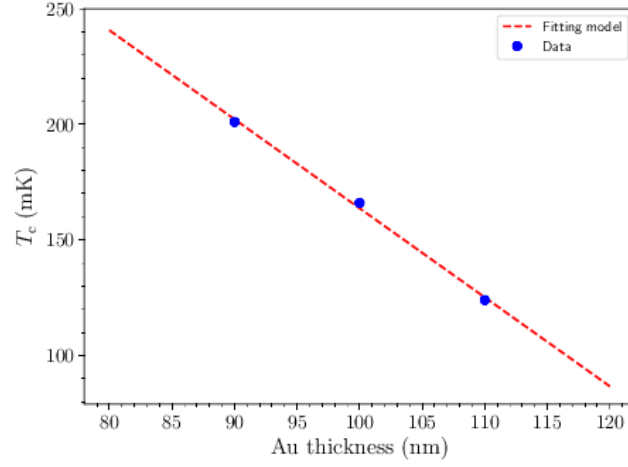
Fig. 6.3   Relation between Au thickness and transition temperature based on previous experiments

Table 6.1   Detailed designed parameters and measurement results of TES

	Material	Item	unit	Designed values	Measured values
Chip	Si	Size	mm^2	6.0×6.0	6.0×6.0
TES	Ti/Au	Size	μm^2	400×400	400×400
		Thickness	nm	40/105	40/106
Electrode wiring	Al	Width	μm	10	10
		Pitch	μm	10	10
		Thickness	nm	120	120
Absorber	Au	Size	μm^2	300×300	300×300
		Thickness	μm	4.0	3.6
Membrane	SiN$_x$	Size	μm^2	600×600	600×600
		Thickness	μm	1.0	1.0

heat of Au , c_{Au}, is estimated from

$$c_{\mathrm{Au}} = 4.2 \times 10 \ T^3 + 6.8 \times 10 \ T \ (\mathrm{JK}^{-1}\mathrm{m}^{-3}), \tag{6.1}$$

where T is given in Kelvin. We decided to set 300×300 μm^2 for the absorber size which gives $C_{\mathrm{abs}} = 3.7$ pJ/K. Transition temperature is controlled by the proximity effect. We vary the thickness of normal metal keeping the thickness of superconducting metal constant. The relation between the transition temperature and thickness of gold was obtained from previous experiments (Figure 6.3). From that relation, we set the thickness of gold of the TES to be 105 nm to satisfy the transition temperature as to be 150 mK and thickness of titanium of the TES to be 40 nm which is previous used value. The detailed designed parameters are shown in Table 6.1 and Figure 6.4 left. We allocated 2×2 array on one Silicon chip limited by the number of wires in the refrigerator (Figure 6.4 right).

6.1.2   Fabrication process of TES microcalorimeter

The TES microcalorimeter was fabricated in house using mainly JAXA and partly Tokyo Metropolitan University process facilities. Table 6.2 shows the fabrication process flow of a TES microcalorimeter. The first step was to form alignment pattern by RIE (Reactive Ion Etching) on both sides of 4-inch Si wafer on which silicon nitride and silicon oxide membranes (SiN$_x$/SiO$_2$ = 1.0/0.5 μm) are deposited. Then, silicon nitride on the membrane
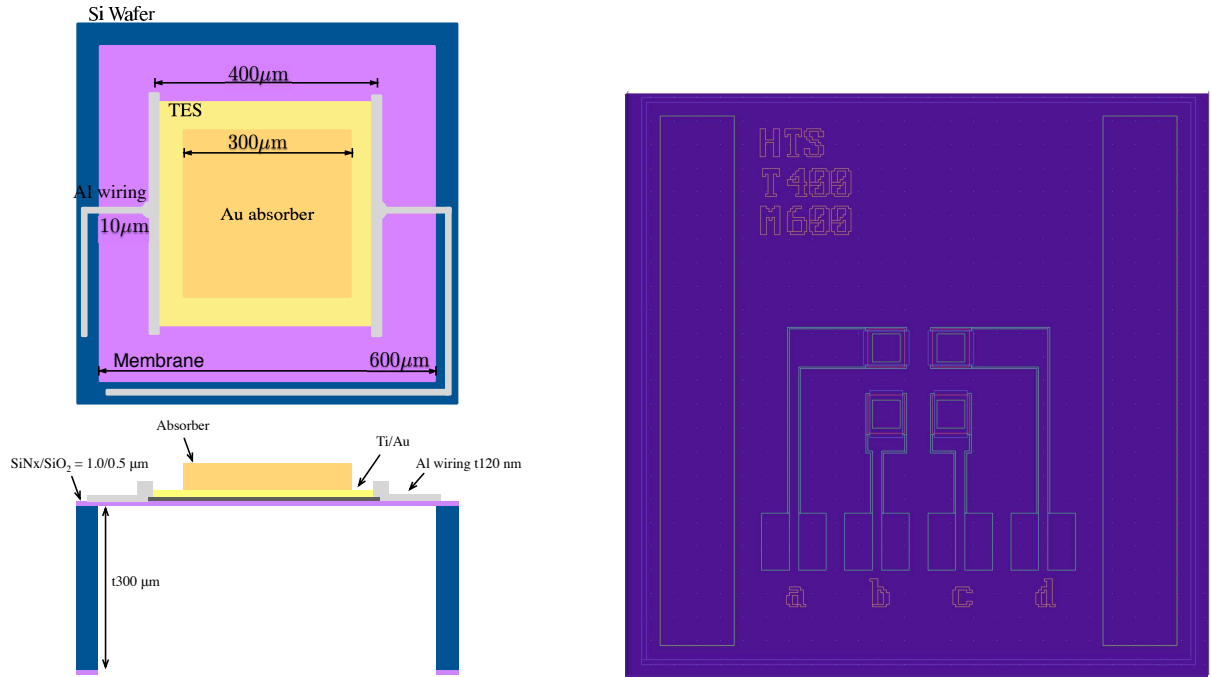
Fig. 6.4 Design of a single pixel TES (left) and cad mask design of 2×2 TES arrays for Oarai test (right).

Table 6.2 Fabrication process flow of TES microcalorimeter

#	Process	Method
1	Formation of alignment pattern on both sides of 4 inch Si wafer	Dry-etching
2	Removal of SiN_x backside of Si wafer for preparation for process #11	Dry-etching
3	Cut to 35 mm square	Dicing
4	Removal of SiO_2 on backside of Si wafer for preparation for process #11	Wet-etching
5	Ti/Au deposition by sputtering for TES	DC magnetron sputtering
6	TES patterning	Wet-etching
7	Al sputtering	RF sputtering
8	Wiring patterning	Wet-etching + Lift-off
9	Electron-beam deposition for absorber	EB-evaporation
10	Absorber patterning	Lift-off
11	Bulk Si etching from backside to form Self-standing membrane and chipping	Dry-etching

pattern of the backside of the wafer was removed by RIE. This removal process took about one hour. The 4-inch wafer was then cut to 4 pieces of 35×35 mm^2 square by the Dicing machine. Then, silicon oxide on the membrane pattern was removed by hydrofluoric acid. The Ti and Au for TES was deposited on the front side by DC magnetron sputtering at Tokyo Metropolitan University. The thicknesses of Ti and Au were 40 nm and 106 nm respectively. Then TES was patterned by wet-etching process with Iodine chemicals and Hydrogen peroxide solution. We side-etched Ti so that Au hanged over Ti at the edges of the TES to avoid the electric current to run near the edges, where we worried about the incomplete transition property of the TES. This etching process took 3 hours. For the Al wiring, Al was deposited by RF sputtering and patterned by wet-etching and lift-off processes. The Au absorber was deposited to the TES by electron-beam evaporation process and then patterned by lift-off process. We selected the lift-off process so that the process does not affect to the transition properties of the TES. Finally, the membrane structure of SiN_x/SiO_2 which supports the TES and works as the thermal link was formed by Si bulk etching with Deep RIE. Without the Ti/Au sputtering process, whole process was

(1)Coat with photoresist

Photoresist

Si wafer

(2)Exposure through the photo mask

UV light

Photo mask

(3)Reversal bake

Insert resist

(4)Flood exposure

UV light

(5)Development

Dissolve

(6)Completion
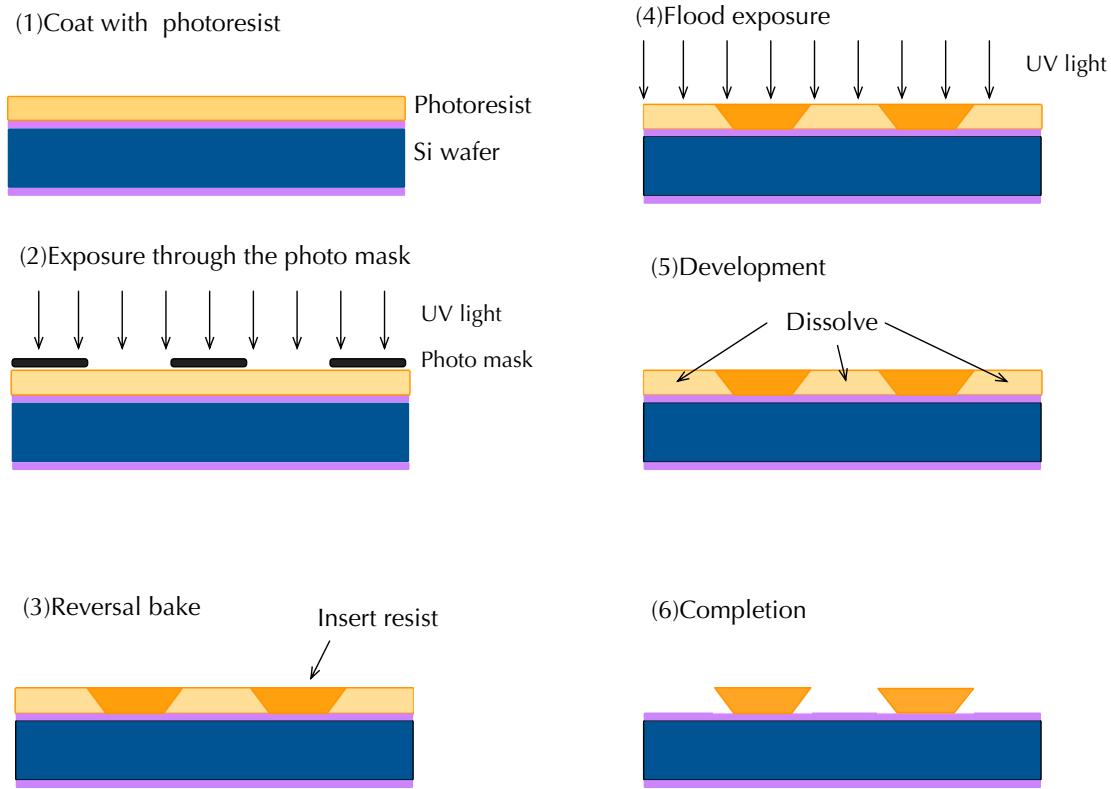
Fig. 6.5   Process schematic view of image reversal photo resist

Table 6.3   Measured and calculated performance parameters of the TES device

Items		Values	Unit
Transition temperature	T_c	164	mK
Heat capacity	C	3.97	pJ/K
Saturation energy	E_sat	51	keV
Ideal energy resolution	ΔE	11	eV

performed in JAXA's nanoelectornic clean room.

In this fabrication process, it was challenging for us to fabricate the Au absorber with above 4 μm thickness by using the lift-off process. In our previous process for fabrication of the absorber, we used positive type photo resist in which the portions reacted with UV light melt. We could not fabricate the absorber with above 4 μm thickness since not the enough thickness of the positive photo resist and the taper configuration of the photo resist pattern. We tested many type of photo resists and finally found that an image reversal photo resist worked well. The image reversal photo resist can be used for both positive and negative types, we used as negative type by performing baking process twice (Figure 6.5). The negative type photo resists reverse to positive type photo resists and in which the portions were not reacted with UV light melt (Figure 6.6). Then we build the process to form the 7.0 μm thickness photo resist which is suited for lift-off process and we could easily make the absorber patern with above 4 μm thickness.

6.1.3   Evaluation of performances of the TES microcalorimeter at ISAS

The fabricated result of the absorber thickness was measured to be 3.6 μm (Figure 6.7). The photograph of the fabricated TES device is shown in Figure 6.8.

(1)Coat with photoresist

Photoresist

Si wafer

(2)Exposure through the photo mask

UV light

Photo mask

(3)Develop the positive photoresist   (3)Develop the negative photoresist
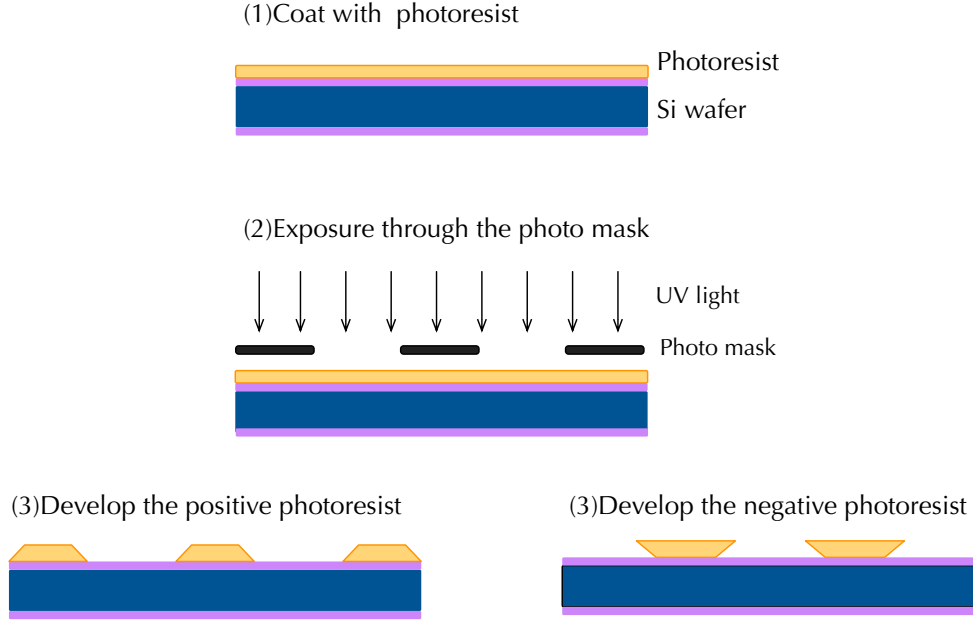
Fig. 6.6   Difference of a positive and a negative photoresist. The positive resist forms a pattern where reacts with UV light and the negative resist forms a pattern where does not react with UV light.
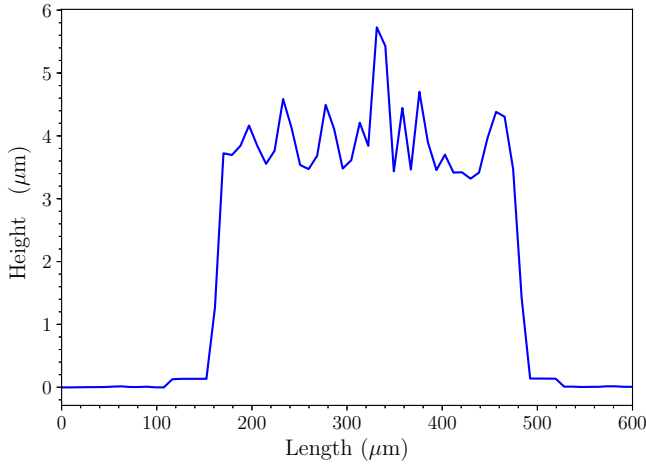
Fig. 6.7   Thickness of Au absorber of the fabricated TES device, the average value was 4.0 μm.

6.0 mm
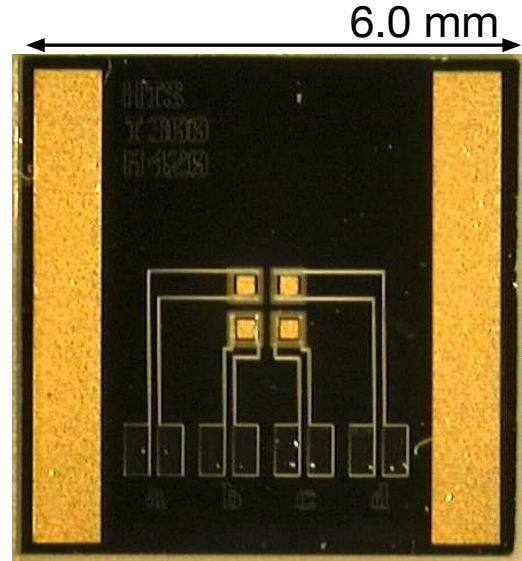
Fig. 6.8   Fabricated 2×2 TES arrays chip

We mounted the TES device and SQUID on the detector head and mounted RuOx for readout the temperature of the detector head (Figure 6.18) and then measured the $R - T$ relation and $I - V$ relation of the TES device using the dilution refrigerator at ISAS. In the $R - T$ measurement, we applied 10 μA as a bias current, which is the sum of the current of the TES and shunt resistance and calculated the resistance of the TES from the SQUID output voltage using Equation (4.156). The detailed parameters of SQUID amplifier is listed in B.1. We varied the stage temperature to obtain $R - T$ curve (Figure 6.9) and found the transition temperature was 164 mK. In order to obtain the $I - V$ relation, we measured the SQUID output voltage with decreasing the
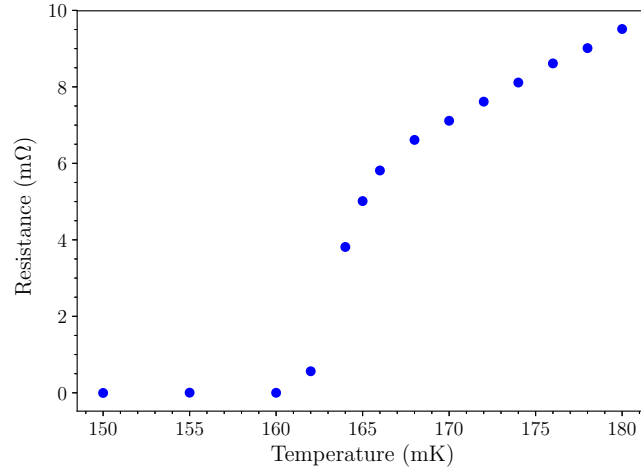
Fig. 6.9 $R - T$ curve of the TES device for Oarai test
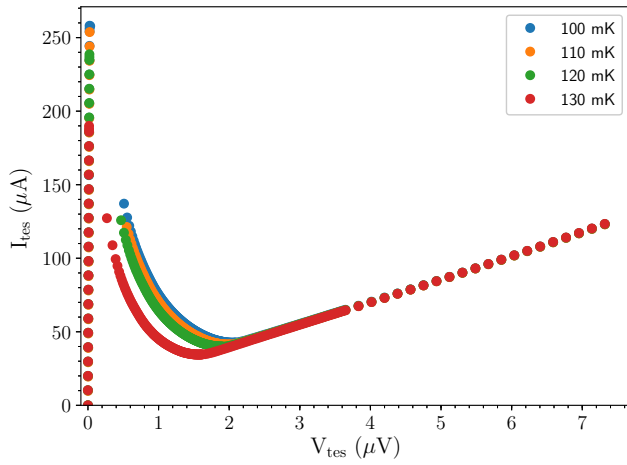
Fig. 6.10 V_{tes} vs I_{tes}
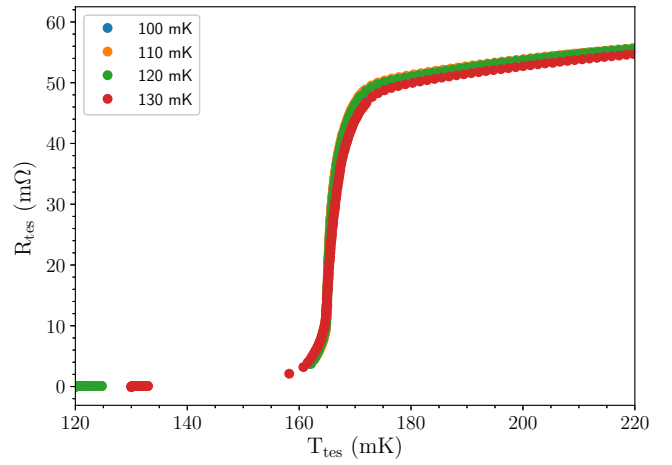
Fig. 6.11 R_{tes} vs T_{tes}
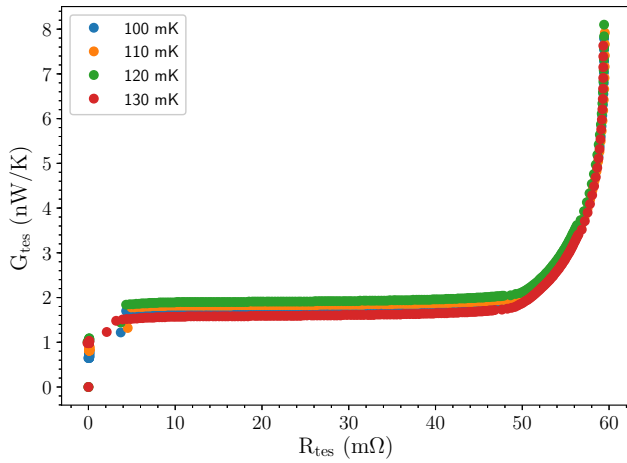
Fig. 6.12 R_{tes} vs G_{tes}
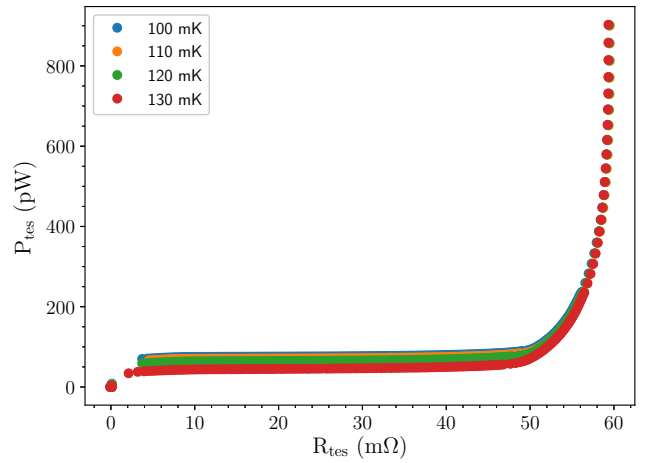
Fig. 6.13 R_{tes} vs P_{tes}
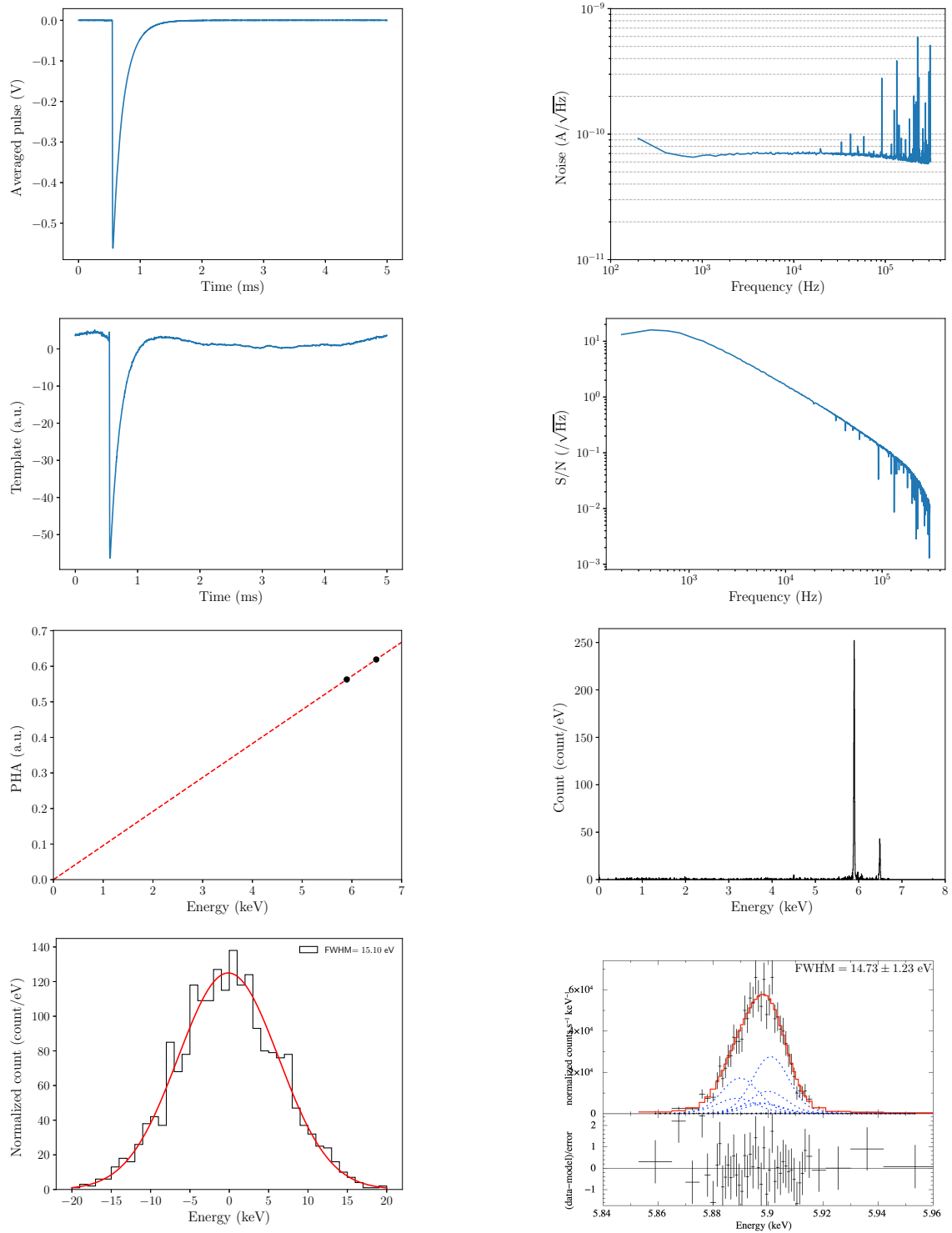
Fig. 6.14 Pulse collection results with ^{55}Fe isotope at 100 mK of bath temperature at ISAS: the averaged pulse (top left), the averaged noise (top right), the template (2nd top left), the S/N spectra (2nd top right), the relation between PHA and energy (2nd bottom left), the energy spectrum (2nd bottom right), the baseline energy resolution (bottom left), and the energy spectrum of MnKα (bottom right)

Table 6.4   Parameters of TES device during X-ray irradiation test with ^{55}Fe and with ^{241}Am isotopes

Item		Unit	Irradiation test with ^{55}Fe	Irradiation test with ^{241}Am
			Values	Values
Bias current	I_{bias}	μA	390	430
Current following TES	I_{tes}	μA	58.83	52.00
Resistance of TES	R_{tes}	mΩ	21.96	28.35
Resistance ration to normal resistance	R_{tes}/R_N	%	37	48
Temperature of TES	T_{tes}	mK	165.3	165.7
Thermal conductance	G	nW/K	1.77	1.78
Loop gain	$\mathcal{L}$		21.3	19.4
Temperature sensitivity	α		82	75

Table 6.5   Obtained energy resolution with ^{55}Fe isotope at ISAS

	Baseline (eV FWHM)	Energy resolution (eV FWHM)
ISAS test with ^{55}Fe isotope	14.24	$14.73^{+1.01}_{-1.12}$

Table 6.6   Obtained energy resolution with ^{241}Am isotope at ISAS and Oarai

	Baseline (eV FWHM)	Energy resolution (eV FWHM)
ISAS test with ^{241}Am isotope	17.77	$20.92^{+2.83}_{-2.24}$
Oarai test with ^{241}Am isotope	33.61	$41.25^{+0.88}_{-1.04}$

bias current from 2000 μA while the stage temperature was kept constant. Then we calculated the resistance of the TES R_{tes}, the power of the TES P_{tes}, and the thermal conductivity G_{tes} for each points on the $I - V$ curve using Equation (4.152), (4.155), (4.29), and parameters of SQUID (Table B.1). We show the relations among those parameters in Figure 6.10, 6.11, 6.12, and 6.13. The region from $V_{\text{tes}} = 2$ μV to $V_{\text{tes}} = 8$ μV in Figure 6.10 corresponds to normal state and the slope is the normal resistance ($R_{\text{N}} = 60$ mΩ), the region around $V_{\text{tes}} = 0$ corresponds to the superconducting state and the slope corresponds to the residual resistance of the TES ($R_{\text{s}} = 9.5 \times 10^{-5}$ mΩ), and the region between normal and super states corresponds to the transition edge. While the TES is on the transition edge, its resistance and the power dissipation is kept constant, which is clearly seen in Figure 6.12 and Figure 6.13. From the result of transition temperature, we estimated the heat capacity of the TES to be 3.97 pJ/K, the saturation energy to be 51 keV, and the ideal energy resolution to be 11 eV with $\alpha = 100$ (Table 6.3). We performed an X-ray irradiation test of the single pixel TES with a ^{55}Fe isotope at the 100 mK bath temperature ($T_{\text{bath}} = 100$ mK). The detailed parameters at the operation point are listed in Table 6.4. We collected 2016 pulses and noises records, generated the template from an average pulse of Mn K$_\alpha$ and noise spectrum, and performed optimal filtering to obtain the PHA. We model fitted the PHA spectrum using PHA model function (Equation (5.2)). Since we had only two lines, Mn K$_\alpha$ and Mn K$_\beta$, whose energies are close to each other, we used a quadratic function for the $PHA - PI$ relation with a constraint that it crosses the origin,

$$PHA = aPI^2 + bPI. \tag{6.2}$$

We converted the PHA spectrum to PI using the equation

$$PI(PHA) = \frac{-b + \sqrt{b^2 - 4 \cdot a \cdot PHA}}{2a}. \tag{6.3}$$

Table 6.7   Parameters of container of ^{233}U isotope

Material	Density of the the container material (g/cm^3)	Thickness of the container (mm)	Type of ^{233}U solution	Thickness of area within the ^{233}U (mm)
Fluoresion (C$_2$ClF$_3$)$_n$	2.1-2.2	0.5	Uranyl choride	3.0

Then the PI spectrum of Mn K$_\alpha$ line was fitted with the Voigt function including the fine structure

$$F(PI) = N \sum_{i=1}^{n} \sum_{j} G(PI - E_j, \sigma) r_i L(E_j, E_{c,i}, \Gamma_i),$$
(6.4)

where $L(E_i, E_{c,i}, \Gamma_i)$ is a Lorentz function for the natural width and $G(PI - E_i, \sigma)$ is a Gaussian function for the detector resolution. When we fitted the Mn K$_\alpha$ line, we know the natural widths, Γ_i, the centroid energies, $E_{c,i}$, and the relative intensities, r_i, from the literature. The free parameters were the energy resolution of the detector σ, the energy E and the normalization N. We also obtained the base line energy resolution by applying the template to noise records. Results are shown in Figure 6.14 and Table 6.5. The energy resolution at 5.9 keVwas $14.73^{+1.01}_{-1.12}$ eV. Then we performed irradiation test with ^{241}Am isotope to evaluate the TES performance at around 30 keV. In this test, we applied 430 μA to the TES bias and set the bath temperature to 100 mK. The detailed parameters of the TES during this irradiation test are listed in Table 6.4. We generated a template from an average pulse of Np L$_\alpha$ and noise spectrum. We applied the local linear relation to PHA spectrum temporary for each lines (see 5.3), and obtained PI to PHA relations of 5 lines Np L$_{\alpha 1}$, Np L$_{\beta_1}$, Np L$_{\gamma 1}$, 26 keV $\gamma - ray$, and 59 keV $\gamma - ray$. PHA values were converted by fitted polynomial function with fourth order. Then the energy resolution at 26 keV was $20.92^{+2.83}_{-2.24}$ eV.

6.2   Measurements in Oarai

6.2.1   Experiment setup

After the evaluation test at ISAS, we carried out irradiation test at JAEA in Oarai because JAEA in Oarai campus holds a ^{233}U source with 26 MBq intensity and we cannot move the ^{233}U source legally. We used a dilution-refrigerator which is property of Kyushu University and has been placed at JAEA at Oarai for research collaboration between Kyushu University and JAEA for γ-ray spectroscopy of nuclear matter (Figure 6.16 left). The refrigerator is pre-cooled by GM refrigerator from 300 K to 4 K then cooled by dilution under 100 mK. The refrigerator has an X-ray window with a Be film (thickness=1 mm) for optical blocking and has filters of aluminized mylar (Multilayer Insulation: MLI) on thermal shields through which we can irradiate the detector with X-ray or γ-ray photons. The ^{233}U source is in a form of liquid solution. Thus the size of the source can be controlled with its container design. Based on the diameter of the X-ray window, we selected the size of the container as 25 mm diameter. The container of the ^{233}U source was made by PCTEF resin ((C$_2$ClF$_3$)$_n$), the thickness of the container was 0.5 mm, and the ^{233}U source was included in the thickness of 3.0 mm (Table 6.7). The distance between the ^{233}U source and the TES device was 48.5 mm and the schematic layout is shown in Figure 6.17.   We installed the detector stage to the refrigerator in Oarai (Figure 6.18). We tried to readout 3 pixels TES by using each dc-SQUID, but partly due to problems in wirings from room-temperature to cryogenic stage in the refrigerator and also due to a problem in the room-temperature SQUID drive electronics, we could only read a single pixel of the TES device. During this campaign, the minimum attained temperature was 80 mK and we operated the TES device at 90 mK bath temperature. We used ^{133}Ba and ^{241}Am isotope as calibration
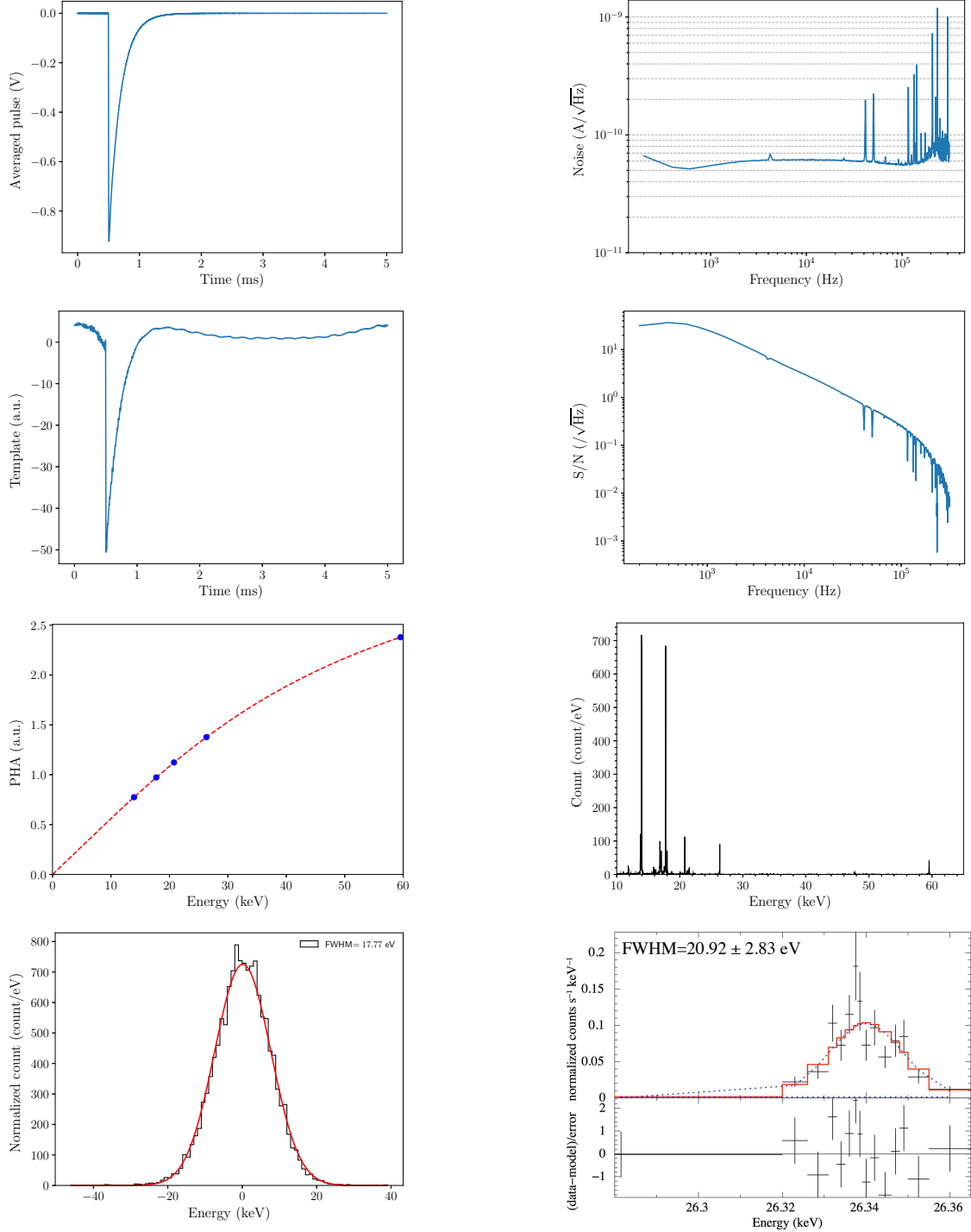
Fig. 6.15 Pulse collection results with ^{241}Am isotope at 100 mK of bath temperature at ISAS: the averaged pulse of Np Lα,Np Lβ, NpLγ, 26 keV, 59 keV (top left), the averaged noise (top right), the template generated by 26 keV (2nd top left), the S/N spectra (2nd top right), the relation between PHA and energy fitted by the spline function (2nd bottom left), the energy spectrum (2nd bottom right), the baseline energy resolution (bottom left), the energy spectrum at 26 keV (bottom right)
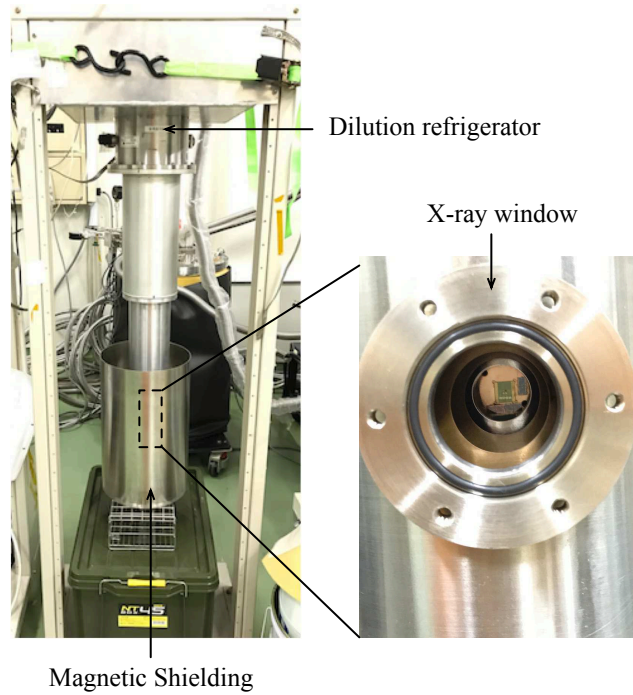
Fig. 6.16   Dilution refrigerator in Oarai (left) and photograph taken during the alignment check (right). We can see the detector chip through the holes of X-ray window and optical blocking filters.
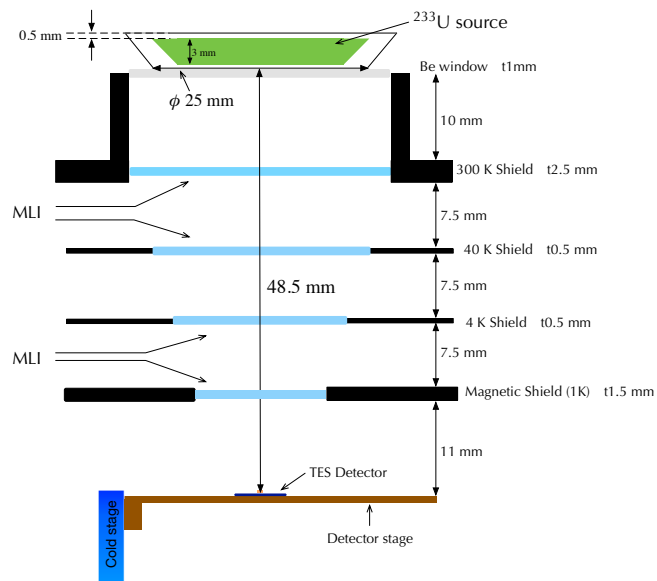
Fig. 6.17   Layout drawing of the ^{233}U source and detector in the refrigerator
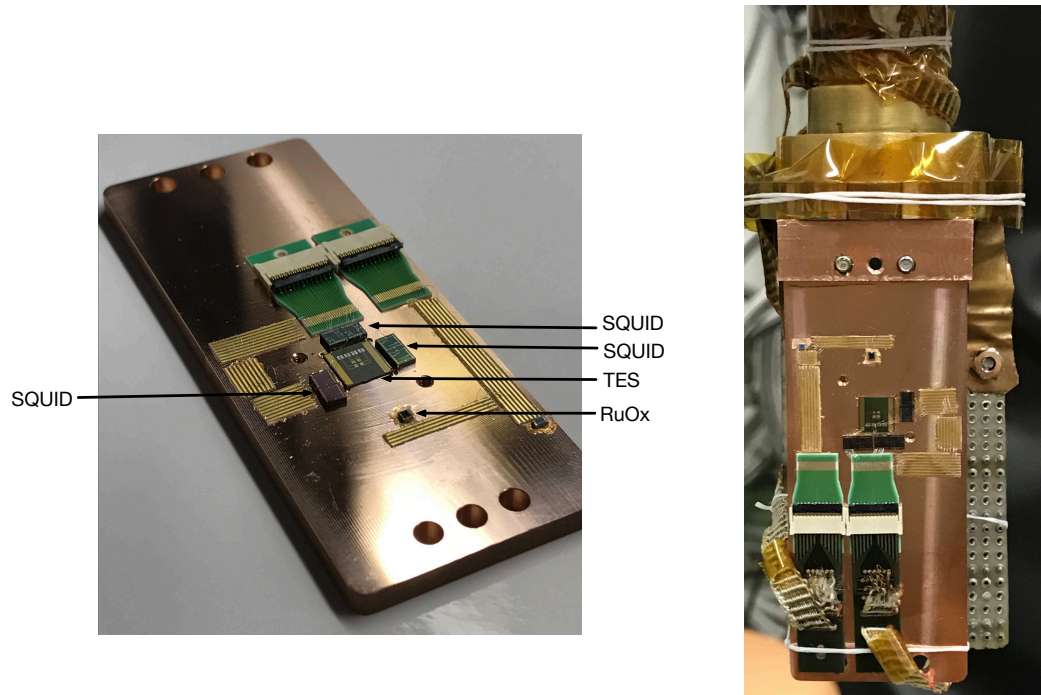
Fig. 6.18 Detector head (left) and detector head mounted on the 100 mK stage of the refrigerator in Oarai (right)
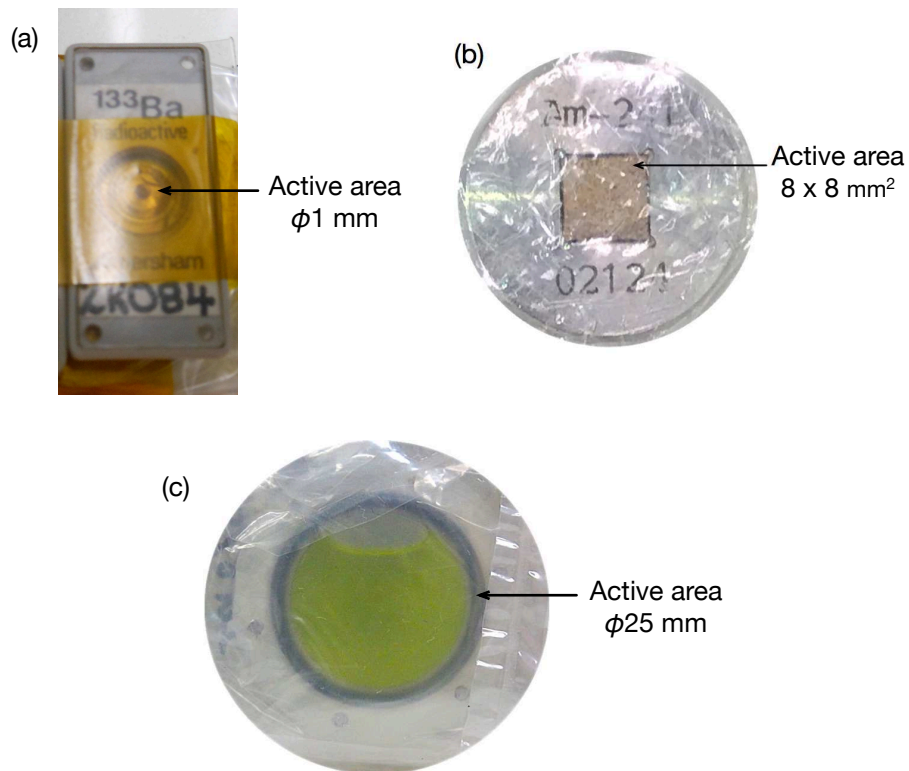
Fig. 6.19 Photograph of ^{133}Ba, ^{241}Am, and ^{233}U isotope. (a) ^{133}Ba isotope whose active area is ϕ 1 mm, (b) ^{241}Am isotope whose active area is 8×8 mm^2, and (c) ^{233}U isotope whose active area is ϕ 25 mm.

Table 6.8   Size and Intensity of ^{133}Ba, ^{241}Am, and ^{233}U isotope

	Size (mm)	Intensity (M Bq)
^{133}Ba	$\phi 1$	0.370
^{241}Am	8×8	2.5
^{233}U	$\phi 25$	26

Table 6.9   Parameters of TES device in measurement of lowest-energy of ^{229}Th isomeric state

Item		Values	Unit
Transition temperature	T_c	164	mK
Bias current	I_bias	410	μA
Current following TES	I_tes	42.7	μA
Resistance of TES	R_tes	48.5	mΩ
Resistance ration to normal resistance	R_tes/R_N	82	%
Temperature of TES	T_tes	171.8	mK
Thermal conductance	G	1.91	nW/K
Loop gain	$\mathcal{L}$	0.8	
Temperature sensitivity	α	3	

isotopes in this campaign. The intensity and size of ^{133}Ba, ^{241}Am, and ^{233}U isotope are summarized in Table 6.8 and those picture are shown in Figure 6.19. The detailed energies and natural widths of these standard isotope are summarized in A.1.

6.2.2   Evaluation of performances of the TES device under ^{233}U isotope irradiation environment

First, we evaluated the performances of the TES device at 26 keV under the ^{233}U isotope irradiation environment using ^{241}Am isotope.We collected 4174 pulses and noises records and generated template from average pulse of 26 keVγ-ray and noise records. We analyzed the datas in the same way of ISAS test (Subsection6.1.3). The results are shown in Figure 6.20 and Table 6.6. The energy resolution was 41.25 $^{+0.88}_{-1.04}$ eV at 26 keV and this value was twice bigger than that of ISAS test.

6.2.3   Measurements lowest-energy of ^{229}Th isomeric state

We set the ^{233}U isotope, the ^{133}Ba isotope, and the ^{241}Am isotope in this order from the detector and they were placed just outside the X-ray window. We applied 410 μA as a TES bias current and kept the system running for 18 days and got the total counts of 989014. The detailed parameter in the measurement are listed in Table 6.9. Before applying optimal filtering, we found a fluctuation of DC level of the pulses and removed pulse datas in which the fluctuation like the delta function and in which the DC level becomes decreasing (Figure 6.22). Then we divided all pulse datas into the 18 subsets separating by time series. In this measurements, we could not separate the 29.19 keV doublet due to not enough energy resolution and could only obtain the 24 pulse events of 29.39 keV, (② → ③) in Figure 6.21. So we could not apply the decay chain which Beck et al. used [3]. In stead, we utilized the decay chain starting from ① in Figure 6.21. In this decay chain, we could not separate two doublets starting from ③ and ④ and observed a line spectrum mixed with ③ → ⑤ and ③ → ⑥ and also observed a line spectrum mixed with ④ → ⑤ and ④ → ⑥. We represent these mixed lines as Equation (2.26) and (2.27) and calculate the lowest-energy of the ^{229}Th isomeric state as

$$E(^{229\mathrm{m}}\mathrm{Th}) = \frac{[E(① → ③) + E'(③ → ⑤, ③ → ⑥)] - [E(① → ②) + E(② → ④) + E'(④ → ⑥, ④ → ⑤)]}{1 - b_{29} - b_{42}}. \quad (6.5)$$
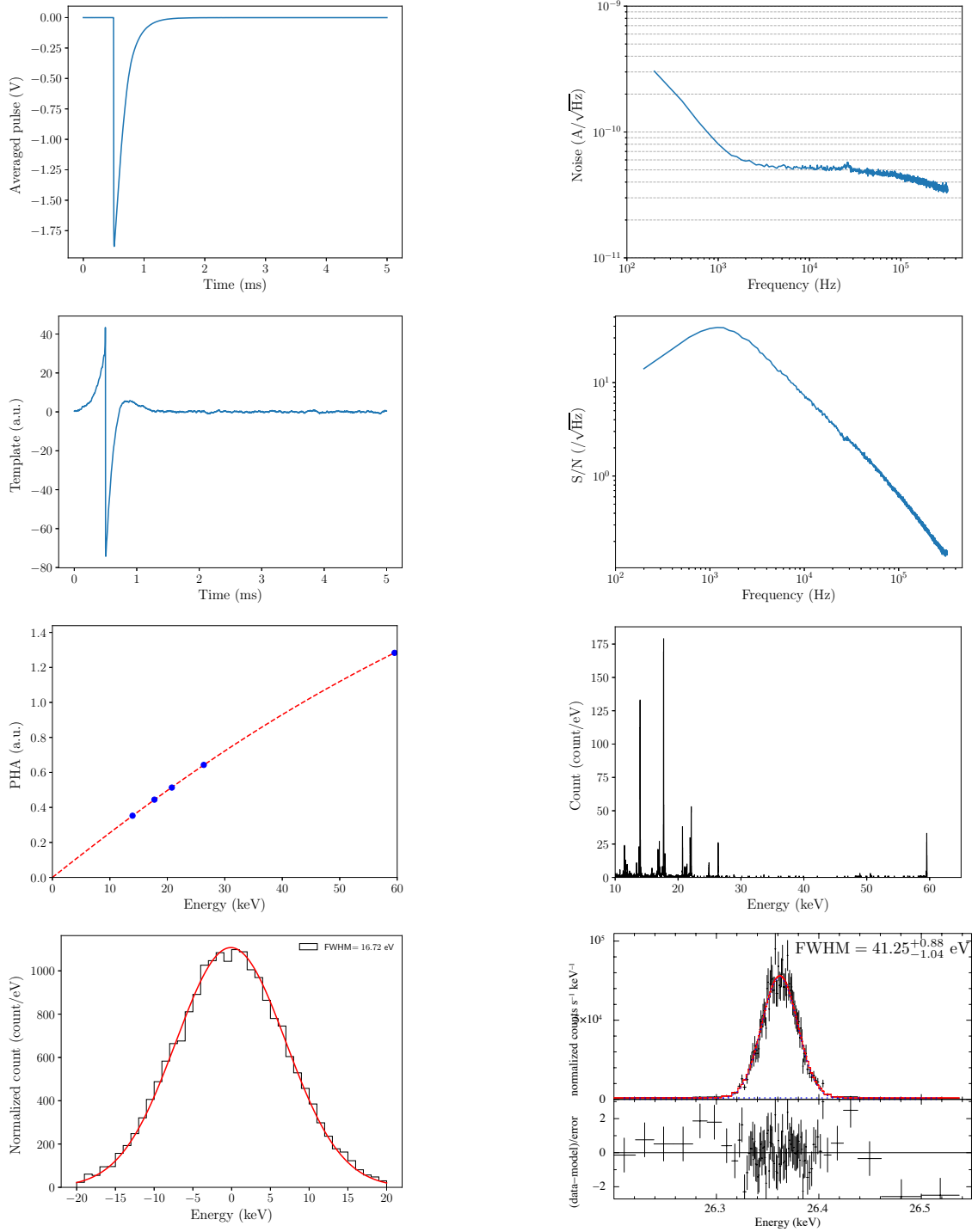
Fig. 6.20 Results of performances at 26 keV under ^{233}U isotope irradiation at 90 mK at Oarai: the averaged pulse of 26 keV, the averaged noise (top right), the template generated by 26 keV line and noise records (2nd top left), the S/N spectrum (2nd top right), the relation between PHA and energy fitted by the empirical model of $R-T$ (2nd bottom left), the energy spectrum (2nd bottom right), the baseline energy resolution (bottom left), and the energy resolution at 26 keV (bottom right)
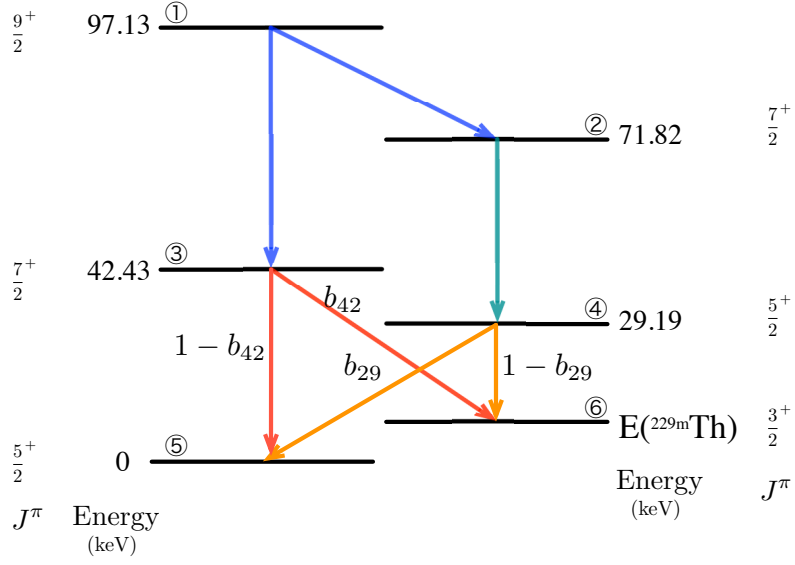
Fig. 6.21   A part of level schemes of the ^{229}Th with decay paths and energies which we used to obtain the lowest-energy of ^{229}Th isomeric state in Oarai
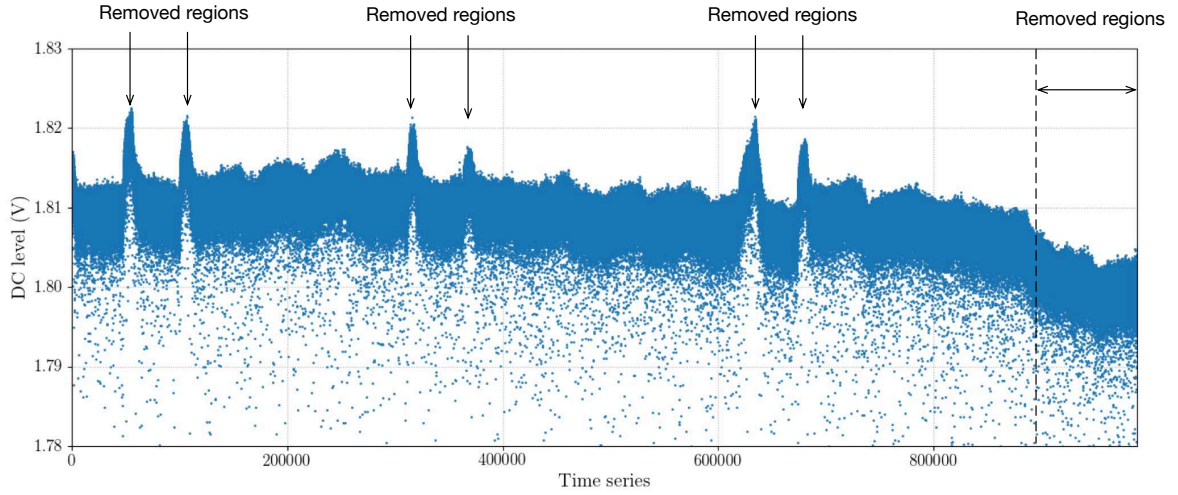
Fig. 6.22   DC level of all pulses in time series order

We run the following procedures for current pulses datas. (a) We calculated the center value of the all noise datas and the DC level of pulses was adjusted to 0 using that value. (b) Selection of normal pulses and elimination of unusual pulses by model fitting of pulses. We used this function as a model fit function,

$$f(t) = A \left[\exp\left(-\frac{t - t_0}{\tau_{\text{decay}}} \right) - \exp\left(-\frac{t - t_0}{\tau_{\text{rise}}} \right) \right], \tag{6.6}$$

where τ_{decay} and τ_{rise} are respectively the decay time constant and the rise time constant. A is a normalization parameter. We show the results of the rise time constant in one of the subsets in Figure 6.23. From the results of the rise time constant, we divided it into 6 regions between 0 and 3.0 μs and saw the pulse shapes of each region and number of pulses. We found that the pulses in the region 1($0 < \tau_{\text{rise}} < 0.36$ μs) included double pulses or more pulses (Figure 6.23 bottom left) and in the region 2 (0.36 μs $< \tau_{\text{rise}} < 1.30$ μs), the decay time
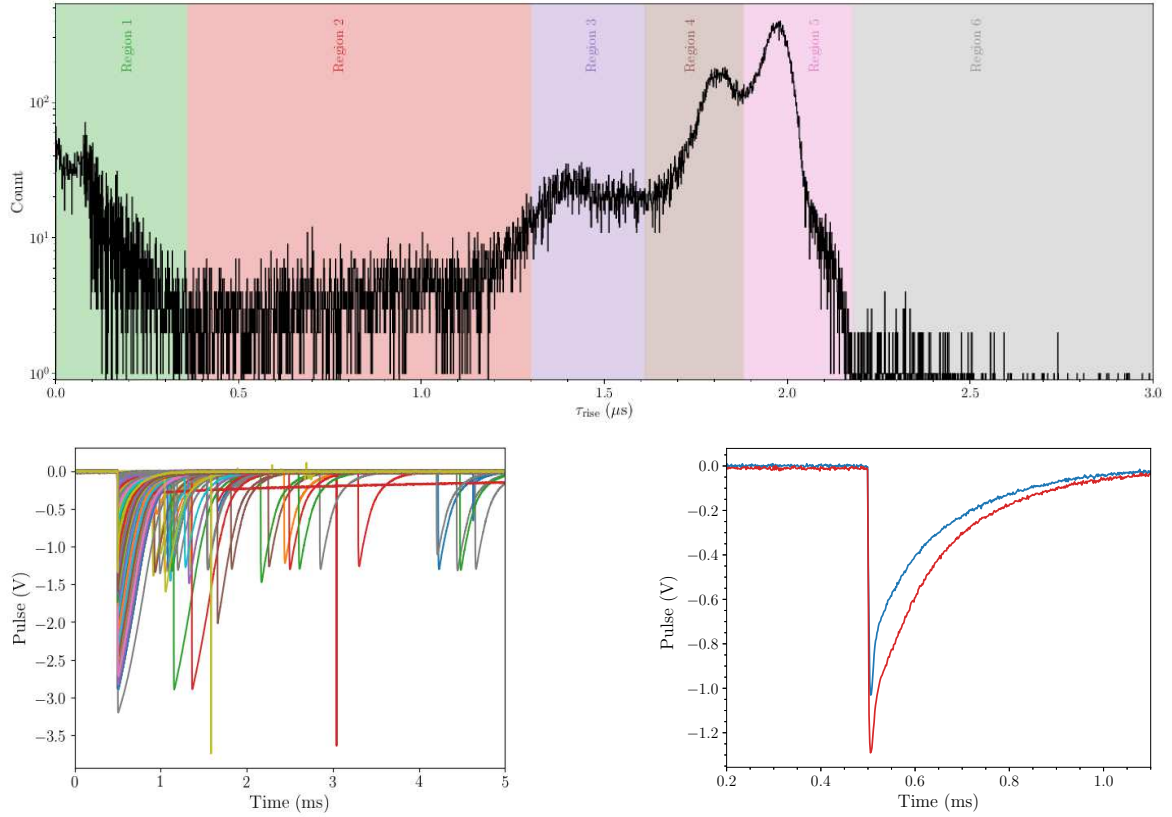
Fig. 6.23   Fitting results of rise time constant: rise time divided into 6 region (top), all pulses in region 1 (bottom left), and some pulses in region 2 (bottom right)

constant changed in two steps. Since these pulses did not match the template which is used in optimal filtering, we eliminated the pules in region 1 and 2 which account for about 10 % of one subset. We did not select the pulses using decay time constant because the difference in the decay time represents the difference in energy. (c) Generating a template using averaged pulse of 26 keV γ-ray and noise records (Figure 6.25). In the optimal filtering, we usually generate a template from line of interest to improve the signal to noise ration of that interested line. In this case, the most interested line was 29.19 keV but we did not know the exact pulse height value of 29.19 keV. We used the pulses of 26 keV γ-ray which are close to 29.19 keV and have a high intensity. (d) Applying the template to all pulses events and obtaining the PHA. We show the average pulse of 26 keV, noise spectra, template and signal to noise spectra of a single subset in Figure 6.25. (e) Model fitting of the PHA spectrum of Th L_α, Th L_β, Th L_γ using the Voigt function assuming linear local gain ($PHA = aE + b$, 5.3). Since the centroid energy, natural width, and relative intensity are known, we performed the model fitting of Th L_α, Th L_β, Th L_γ line complexes (Table 6.10) with free parameters of a, b, σ, and normalization. In this time we did not use the tail function because we could not see clearly the tail in the low energy side of the lines. Another calibration lines are far enough and separated so that we performed the model fitting of Ag $K_{\beta1}$, 26 keV, Cs $K_{\alpha2}$, Cs $K_{\alpha1}$, Au $L_{\alpha1}$ escape, and 59 keV lines separately with the Voigt function assuming by ($PHA = aE$). (f) Obtaining the relation between PHA and energy and then converting PHA to PI using a spline function (Figure 6.25). (g) We run the procedure from (a) to (f) for each subset separately and summed up all subsets here (Figure 6.26). We found the differences between the PI and energy (Figure 6.24 and Table 6.11). (h) We further continued calibration PI to energy in narrow region in which is interested line and calibration lines. For example line of interest is 29.19 keV ($E'(④ \rightarrow ⑥, ④ \rightarrow ⑤)$), we used 26 keV γ-ray, Cs $K_{\alpha1}$, and Cs $K_{\alpha2}$ as

Table 6.10   Line complexes in Th L lines that we used model fitting in PHA space

Line complex	Fine structures
Th Lα complex	Th Lα_1, Th Lα_2
Th Lβ complex	Th Lβ_1, Th Lβ_3
Th Lγ complex	Th Lγ_1, Th Lγ_2, Th Lγ_3, Th Lγ_6
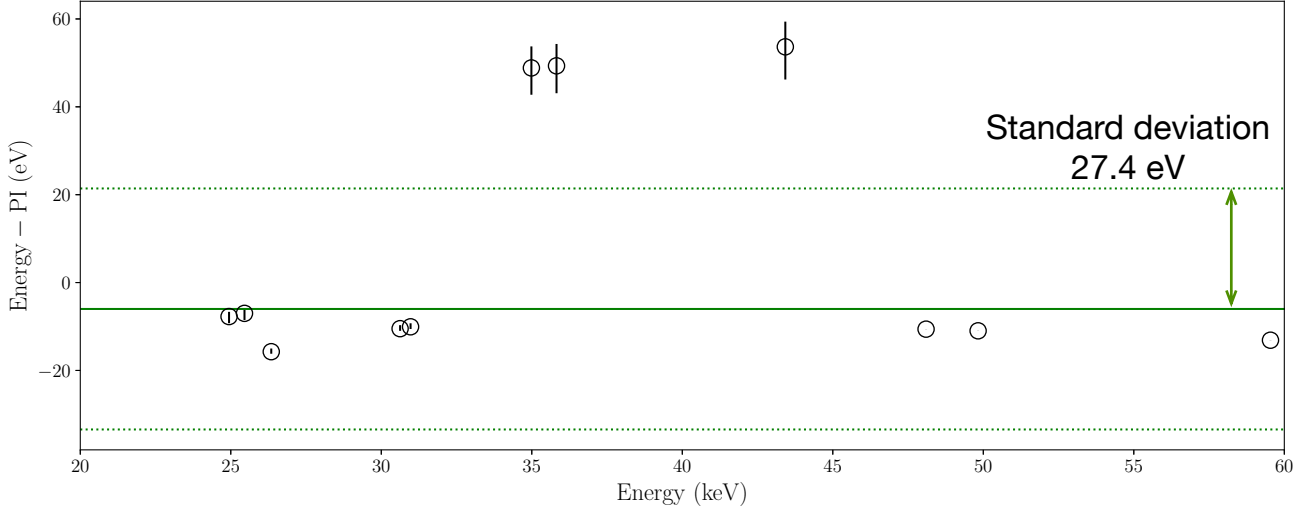
Fig. 6.24   Difference between PI and energy of calibration lines in current pulses

Table 6.11   Results of fitted PI spectra of the calibration lines by line model

Line	Main peak from literature [54](keV)	Main peak PI-E (eV)
Ag K$_{\beta1}$	24.94242	$7.87^{+1.05}_{-1.38}$
Am(26)	26.3448	$15.73^{+0.36}_{-0.46}$
Cs K$_{\alpha1}$	30.97313	$10.03^{+0.37}_{-0.46}$
Cs K$_{\beta1}$	34.9873	$-48.86^{+1.97}_{-2.74}$
Am(43)	43.423	$-53.65^{+1.97}_{-2.74}$
Au L$_{\beta1}$ escape	48.0988	$10.60^{+0.01}_{-0.01}$
Au L$_{\alpha1}$ escape	49.8278	$10.98^{+0.01}_{-0.01}$
Am(59)	59.5412	$13.12^{+0.01}_{-0.01}$

calibration lines. These calibration lines were fitted simultaneously by the Voigt function including $PI = cE + d$, where c and d are free parameters while $E'(\textcircled{4} \rightarrow \textcircled{6}, \textcircled{4} \rightarrow \textcircled{5})$ line was fitted by the Gaussian function. Then we corrected the $E'(\textcircled{4} \rightarrow \textcircled{6}, \textcircled{4} \rightarrow \textcircled{5})$ by the equation of $(PI - d)/c$. We performed this local PI calibration to $E(\textcircled{1} \rightarrow \textcircled{2})$, $E(\textcircled{1} \rightarrow \textcircled{3})$, $E(\textcircled{2} \rightarrow \textcircled{4})$, and $E'(\textcircled{3} \rightarrow \textcircled{5}, \textcircled{3} \rightarrow \textcircled{6})$. We used Ag K$_{\beta1}$ and Ag K$_{\beta2}$ as calibration lines for $E(\textcircled{1} \rightarrow \textcircled{2})$, Au L$_{\beta1}$, Au L$_{\beta2}$, Au L$_{\beta3}$, Au L$_{\beta4}$ escape lines, Au L$_{\alpha1}$, Au L$_{\alpha2}$ escape lines, and 59 keV as calibration lines for $E(\textcircled{1} \rightarrow \textcircled{3})$, and Cs K$_{\beta1}$, Cs K$_{\beta2}$, and 43.4 keV as calibration lines for $E(\textcircled{2} \rightarrow \textcircled{4})$, and $E'(\textcircled{3} \rightarrow \textcircled{5}, \textcircled{3} \rightarrow \textcircled{6})$ (Figure 6.27). The energy of 5 interested lines are listed in Table 6.12. (i) Finally, we calculated the lowest-energy of ^{229}Th isomeric state using Equation (6.5).The lowest energy of ^{229}Th isomeric state with statistical error was

$$E(^{229m}\text{Th}) = \frac{(54.744 + 42.429) - (25.320 + 42.630 + 29.183)}{1 - 1/13 - 1/50} \tag{6.7}$$

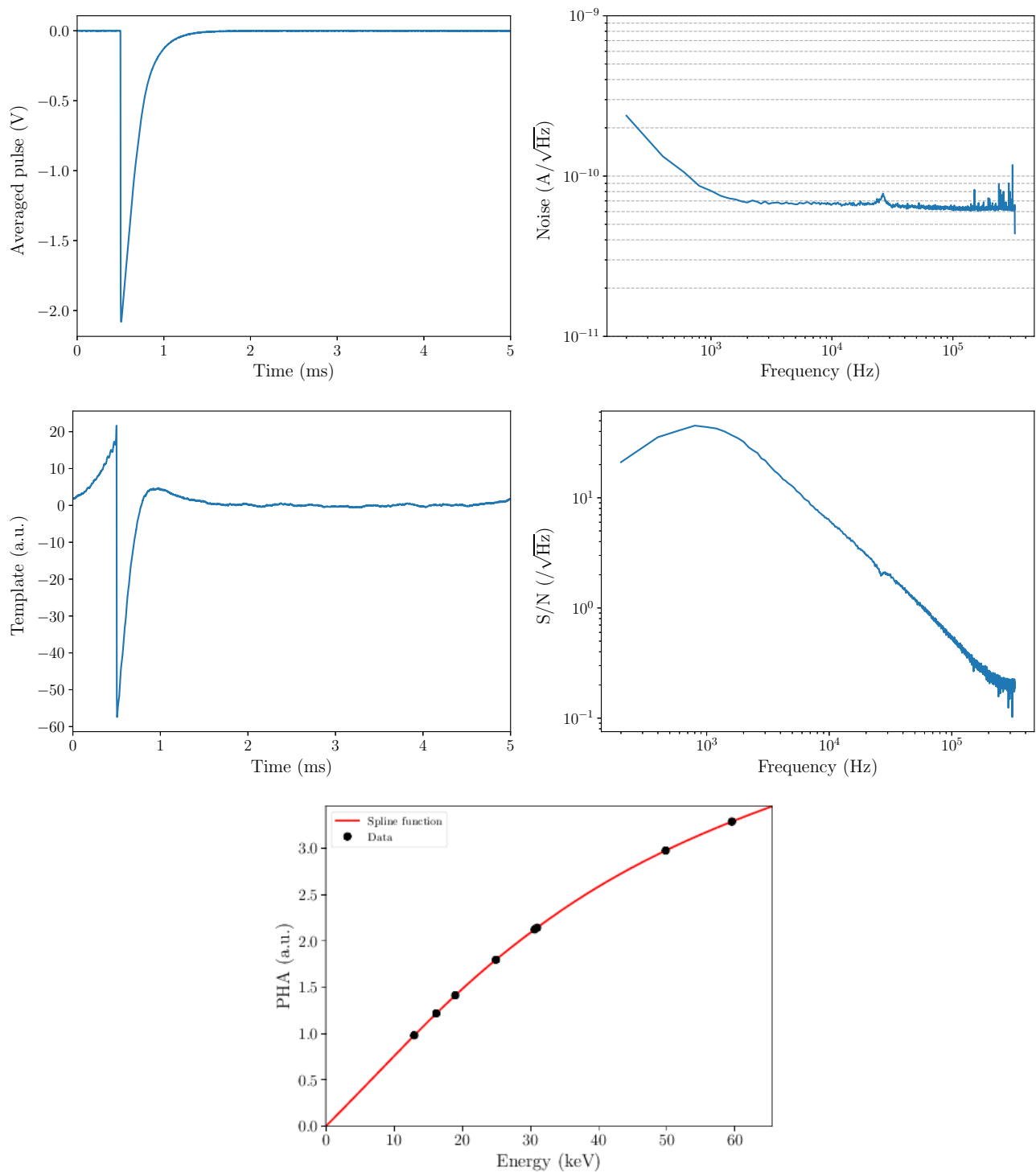$$= 44^{+13}_{-11} \text{ (eV)}. \tag{6.8}$$

Fig. 6.25 Pulse collection results with ^{133}Ba, ^{241}Am, ^{233}U isotope of a single subset: the average pulse of 26 keV line (top left), the average noise spectra (top right), the template generated by 26 keV line (2nd top left), the S/N spectra (2nd top right), and the relation between the PHA and energy fitted by the empirical $R - T$ model (bottom).
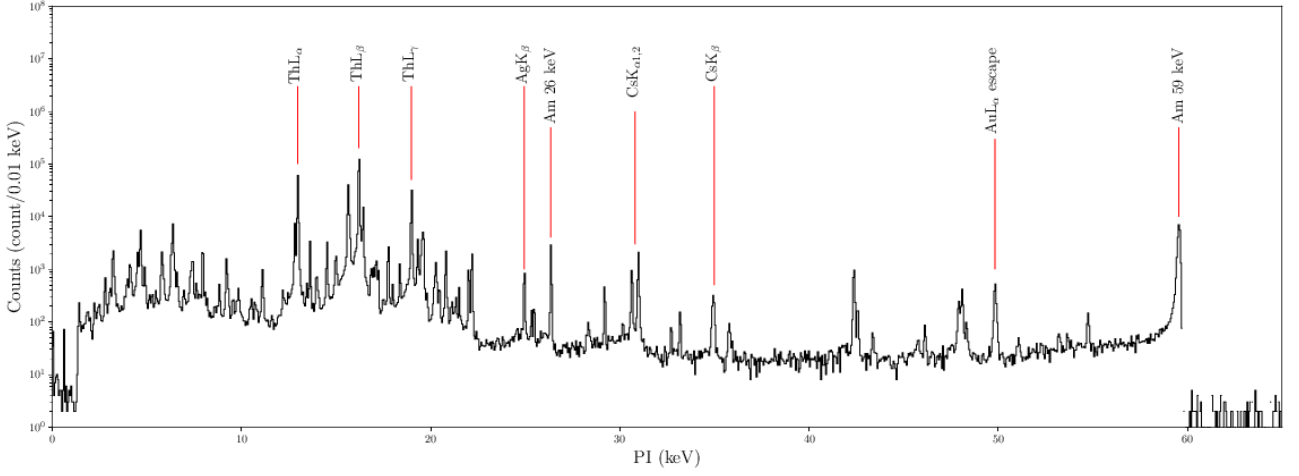
Fig. 6.26   *PI* spectrum after summing up all data sets. We labeled the lines which are used in *PHA*spectrum fit

Table 6.12   Measured energy, their counts, and the energy resolution of γ-ray decay from ^{229}Th of the current pulses

Decay level	Energy (keV)	Counts	FWHM (eV)
$E(①\rightarrow②)$	$25.320^{+0.004}_{-0.002}$	142^{+23}_{-24}	$35.01^{+7.40}_{-4.78}$
$E(①\rightarrow③)$	$54.744^{+0.007}_{-0.005}$	238^{+38}_{-25}	$98.56^{+0.03}_{-0.03}$
$E(②\rightarrow④)$	$42.630^{+0.006}_{-0.009}$	331^{+33}_{-32}	$88.30^{+3.31}_{-2.09}$
$E'(③\rightarrow⑤,③\rightarrow⑥)$	$42.429^{+0.006}_{-0.007}$	1923^{+72}_{-57}	$88.30^{+3.31}_{-2.09}$
$E'(④\rightarrow⑥,④\rightarrow⑤)$	$29.183^{+0.002}_{-0.002}$	644^{+46}_{-41}	$52.09^{+2.55}_{-3.79}$

We estimated the systematic error as following procedures using calibration lines. We assumed the centroid energy of *PI* spectrum $PI_{c,i}$ was represented

$$PI_{c,i} = E_c \pm \sigma_{i\text{sys}} \pm \sigma_{i\text{stat}}, \tag{6.9}$$

where $\sigma_{i\text{sys}}$ and $\sigma_{i\text{stat}}$ are systematic error and statistical error respectively for ith pulse. The expectation valued of difference between $PI_{c,i}$ and $E_{c,i}$ is

$$< \sum_{i=1}^{N}(PI_{c,i} - E_c)^2 > = < \sum_{i=1}^{N}(\sigma_{i\text{sys}} + \sigma_{i\text{stat}})^2 >, \tag{6.10}$$

$$= < \sum_{i=1}^{N}(\sigma_{i\text{sys}}^2 + 2\sigma_{i\text{sys}}\sigma_{i\text{stat}} + \sigma_{i\text{stat}}^2) >, \tag{6.11}$$

$$= < \sum_{i=1}^{N}\sigma_{i\text{sys}}^2 > + < \sum_{i=1}^{N}\sigma_{i\text{stat}}^2 >, \tag{6.12}$$

where we assume $< \sigma_{i\text{sys}}\sigma_{i\text{stat}} >= 0$. The dispersion for the systematic error of calibration lines is

$$\sigma_{\text{sys}}^2 = \frac{1}{N} < \sum_{i=1}^{N}\sigma_{i\text{sys}}^2 >, \tag{6.13}$$

$$= \frac{1}{N} < \sum_{i=1}^{N}(PI_{c,i} - E_c)^2 > - < \sum_{i=1}^{N}\sigma_{i\text{stat}}^2 >, \tag{6.14}$$
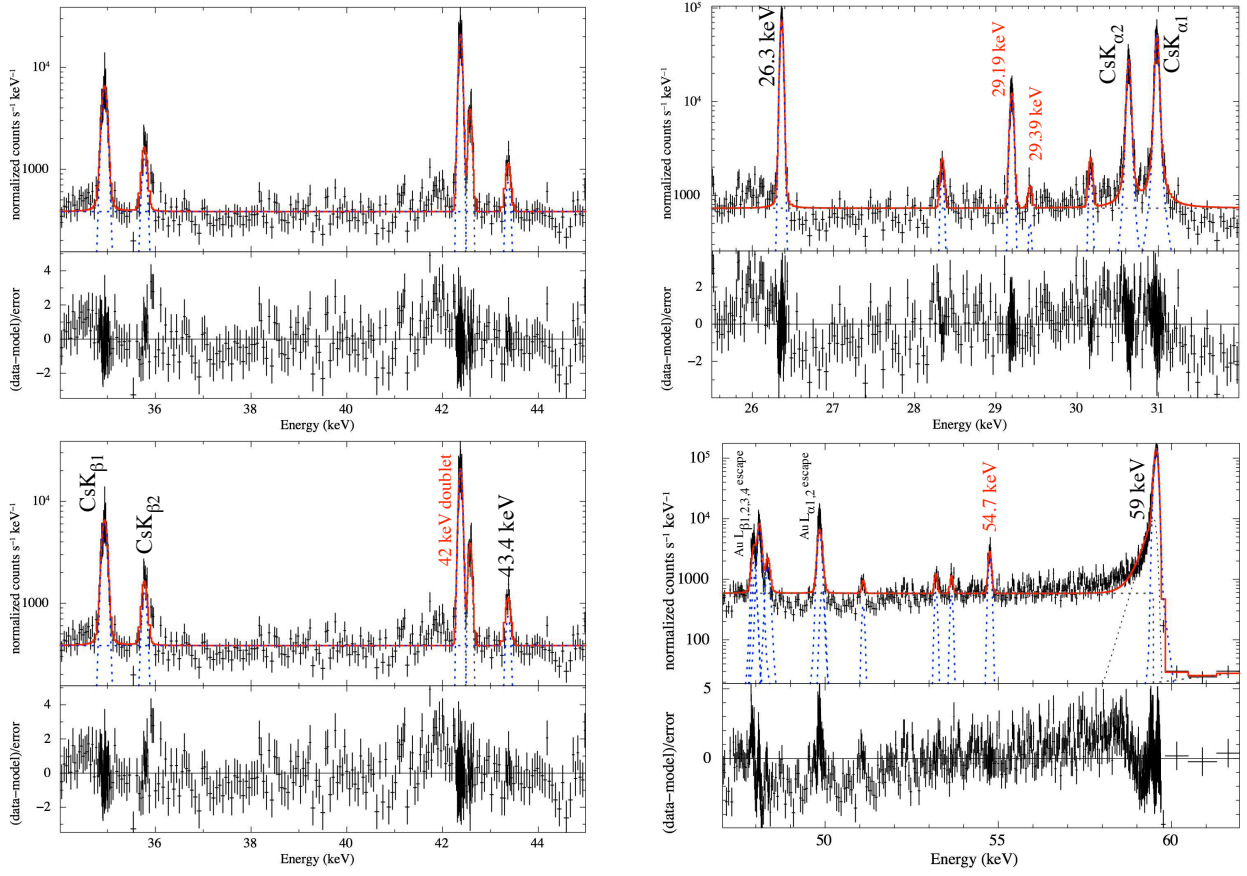
Fig. 6.27   Energy spectrum for each target lines of ^{229}Th by fitting line model : the energy spectra around 25 keV(top left), the energy spectra around 29 keV (top right), the energy spectra around 42 keV (bottom left), and the energy spectrum around 54 keV (bottom right)

and the standard deviation for the systematic error is

$$\sigma_{\rm sys} = \sqrt{\sigma_{\rm sys}^2}, \tag{6.15}$$

$$= \sqrt{\frac{1}{N} < \sum_{i=1}^{N} (PI_{c,i} - E_c)^2 > - < \sum_{i=1}^{N} \sigma_{i{\rm stat}}^2 >}. \tag{6.16}$$

We then calculated the standard deviation of the systematic error using $PI_c - E_c$ and $\sigma_{\rm stat}$, which were obtained by model fitting of PI spectrum. The standard deviation of the systematic error for the current pulses was

$$\sigma_{\rm sys}^2 = 7.52 \times 10^{-4} - 0.08 \times 10^{-4} = 7.44 \times 10^{-4} \ ({\rm keV})^2 \tag{6.17}$$

$$\sigma_{\rm sys} = 27.3 \ ({\rm eV}). \tag{6.18}$$

We assumed the systematic error occurs to $E(① \rightarrow ②)$, $E(① \rightarrow ③)$, $E(② \rightarrow ④)$, $E'(③ \rightarrow ⑤, ③ \rightarrow ⑥)$, and $E'(④ \rightarrow ⑥, ④ \rightarrow ⑤)$ independently and calculated the systematic error for the lowest-energy of ^{229}Th isomeric state as $\sigma_{\rm sys} \times \sqrt{5} = 61$ (eV). Thus the lowest energy of ^{229}Th state within the statistical error and the systematic error calculated by the current pulses was

$$E(^{229{\rm m}}{\rm Th}) = 44^{+13}_{-11} \pm 61 \ ({\rm eV}). \tag{6.19}$$
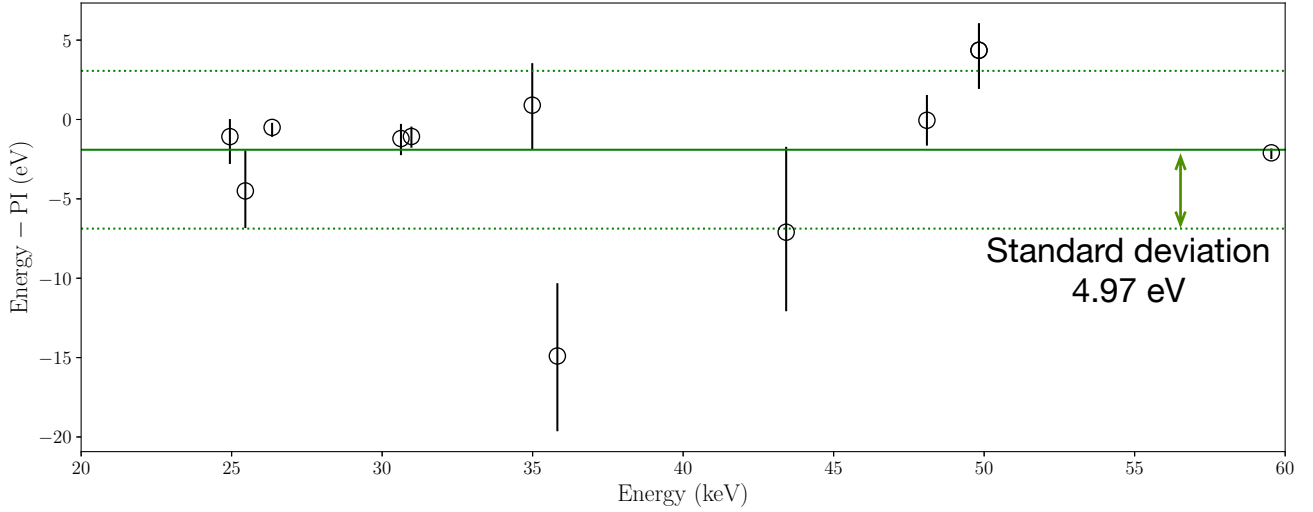
Fig. 6.28   Difference between PI and energy of calibration lines in resistance pulses

Table 6.13   Measured energy and the energy resolution of γ-ray decay from ^{229}Th of the resistance pulses

Decay level	Energy (keV)	FWHM (eV)
$E(\text{①} \rightarrow \text{②})$	$25.315^{+0.003}_{-0.002}$	$43.20^{+2.90}_{-4.83}$
$E(\text{①} \rightarrow \text{③})$	$54.701^{+0.005}_{-0.003}$	$76.34^{+7.93}_{-7.08}$
$E(\text{②} \rightarrow \text{④})$	$42.636^{+0.003}_{-0.004}$	$81.24^{+8.66}_{-5.05}$
$E'(\text{③} \rightarrow \text{⑤}, \text{③} \rightarrow \text{⑥})$	$42.439^{+0.002}_{-0.001}$	$80.75^{+2.63}_{-1.88}$
$E'(\text{④} \rightarrow \text{⑥}, \text{④} \rightarrow \text{⑤})$	$29.181^{+0.001}_{-0.002}$	$45.29^{+2.40}_{-2.97}$

We performed these procedures for the resistance pulses and calculated the lowest energy of ^{229}Th isomeric state. The current pulses are converted to resistance pulses using Equation (4.141) and we analyzed the datas following (a)-(i) procedures. In the resistance pulses, we also found the difference between PI and energy (Figure 6.28) and calculated the standard deviation for the systematic error and the result was

$$\sigma_{\text{sys}}^2 = 2.47 \times 10^{-5} - 0.67 \times 10^{-5} = 1.8 \times 10^{-5} \text{ (keV)}^2 \tag{6.20}$$

$$\sigma_{\text{sys}} = 4.2 \text{ (eV)}. \tag{6.21}$$

The systematic error for the lowest-energy of ^{229}Th isomeric state is calculated by $4.2 \times \sqrt{5} = 9.5$ (eV). Thus the lowest-energy of ^{229}Th isomeric state within the statistical error and the systematic error calculated by resistance pulses was

$$E(^{229\text{m}}\text{Th}) = 8.4^{+7.2}_{-5.8} \pm 9.5 \text{ (eV)}. \tag{6.22}$$

The detailed energy of 5 γ − ray are listed in Table 6.13.

6.3   Problems and Summary

We designed and fabricated the TES detector for measurement of the lowest-energy of ^{229}Th isomeric state. In this campaign, we found two problems; (1) the large statistical error. This was caused by not enough energy resolution at around 30 keV, i.e., the energy resolution was 21 eV at 26 keV in the ISAS test. Furthermore, the energy resolution degraded in the Oarai campaign by a factor of two (from 21 to 41 eV) from the ISAS experiment.
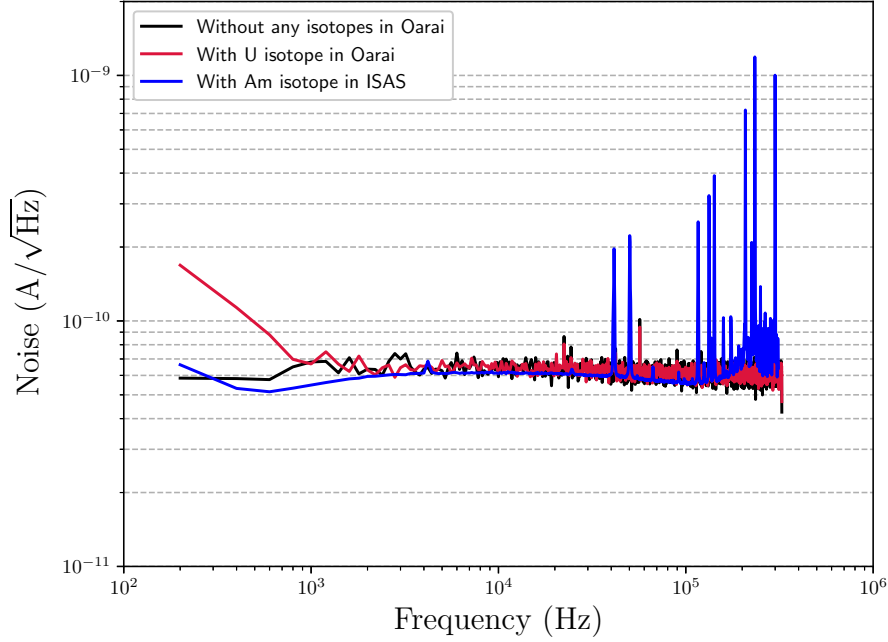
Fig. 6.29 Noise spectrum; compression of the noise level without any isotope (black) and with ^{233}U isotope at Oarai (red) and with ^{241}Am isotope at ISAS (blue).

We compared the noise spectra at Oarai with that at ISAS (Figure 6.29) and found that the noise spectrum at Oarai below 1 kHz was larger than that of ISAS, i.e., signal to noise ration (S/N) was decreased. By the fitting of averaged pulse of 26 keV $\gamma-$ray during irradiation test with ^{233}U, ^{241}Am, and ^{133}Ba isotope, we found the rise time was 1.86 μs and the decay time was 182 μs. Thus the pulses have power spectrum below 5.5 kHz. The degradation of the energy resolution could be caused by declining of S/N in the frequency range where the signal information exists. There are several reasons that increase low-frequency noise, for example, the thermal fluctuation of the TES, electronic noise, and vibration of the refrigerator. We measured the noise spectrum with and without the ^{233}U source to search the effect which is caused by Si substrate hits of γ-rays. From the result (Figure 6.29), we found the low-frequency noise with the ^{233}U source was 3 times larger without the source. We thus conclude the degradation was at least partly caused by thermal fluctuation of the Si substrate. We may be able to block those gamma-rays to hit the Si substrate. The other reason that made the statistical error large was less statistics. For example, the number of counts of $E(\textcircled{1} \rightarrow \textcircled{2})$ was only 142. (2) Second problem is the large systematic error and uncertainty of its estimation. The calibration lines are a few to several keV away from the lines of interest for calculation of lowest-energy of ^{229}Th isomeric state.

   In spite of those problems, we estimated the lowest-energy of ^{229}Th isomeric state from this experiment using the current pulses and resistance pulses. From the analysis using the resistance pulses, the value was $8.4^{+7.2}_{-5.8}\pm9.5$ eV within the statistical error and the systematic error assuming branching ratios of 1/13 and 1/50 for the transitions $\textcircled{3}$ to $\textcircled{5}$ and $\textcircled{4}$ to $\textcircled{6}$, respectively(Figure 6.21). This value consists with present limit (9.5 eV $< E(^{229m}$Th) $<$ 18.3 eV).

Chapter 7

Improvement and Evaluation of TES and Detector Stage

From the Oarai campaign, we found that we need to improve the energy resolution under ^{233}U irradiation environment, and to set more calibration lines near the interest lines for calibration of the lowest-energy of ^{229}Th isomeric state. For the former purpose we developed a new calorimeter array and a collimator system on the detector head. These will be described in this Chapter. We introduced new calibration sources, which will be described in the next Chapter

7.1 Redesign and Fabrication Results of Performance Parameters of TES

In the Oarai campaign, we used lines up to 59 keV, which was not expected. Even though the saturation energy was 51 keV, the energy resolution was not enough. Since there is no good solution to increase the saturation energy, we decided to improve the energy resolution at lower energy. This can be realized only by decreasing the temperature. We set the target saturation energy at 40 keV and decreased the transition temperature to 120 mK. Then the designed energy resolution at low energy is improved from 10 to 8 eV.

We fabricated the TES using in house as described in 6.1.2 (Figure 7.1). In this time, we selected the thickness of Ti/Au of the TES to 40/145 nm based on the last experiments that results is different from 6.3. The specific heat or the absorber decreases with the decrease of operating temperature. In order to keep the saturation energy at 40 keV, we did not decrease the thickness of the absorber and set it to 3.9 μm. The measured $R - T$ curve is shown Figure 7.2 and the transition temperature was 122 mK. We summarized the changed geometry parameters and the performance parameters of measured and calculated in Table 7.1 and 7.2.

Table 7.1   Changed geometry values of TES

	Material	Item	Measured values	Unit
TES	Ti/Au	Thickness	40/145	nm
Absorber	Au	Thickness	3.9	μm

Table 7.2   Measured and calculated the performance parameters of TES

Items		Values	Unit
Transition temperature	$T_{\rm c}$	122	mK
Heat capacity	C	3.57	pJ/K
Saturation energy	$E_{\rm sat}$	40	keV
Energy resolution	FWHM	8.0	eV
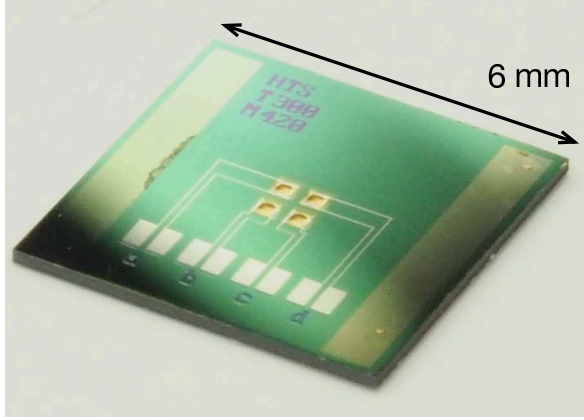
Fig. 7.1   Fabricated 2×2 TES arrays
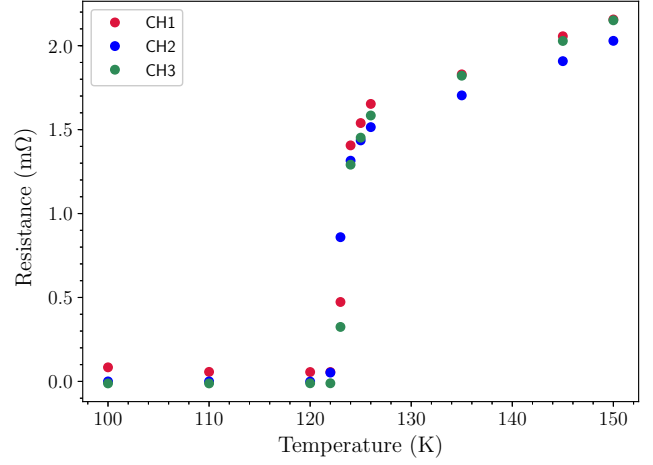
Fig. 7.2 $R - T$ curve of the TES device. The transition temperature was 122 mK

Table 7.3   TES bias values during ^{55}Fe irradiation test

		CH1	CH2	CH3
Bias current	$I_{\text{bias}}(\mu A)$	250	270	245

Table 7.4   Baseline energy resolution and energy resolution of 3 channels during ^{55}Fe irradiation test

		CH1	CH2	CH3
Baseline energy resolution	(eV)	8.72	10.24	9.98
Energy resolution @ 5.9 keV	(eV)	10.02 ± 1.07	10.03 ± 0.76	10.64 ± 0.99

7.2   Performance of TES with ^{55}Fe at ISAS

We performed the irradiation test with ^{55}Fe isotope (Table 5.1) to evaluate the performance of the TES at 5.9 keV. In this case, we read the 3 pixels limited by the room circuit. The bath temperature was set to be 60 mK and the pulses and noises were collected 1000 pulses for each. The operating points are shown in Table 7.3. We generated a template from average pulse of Mn K$_\alpha$(5.9 keV) and noise spectrum and applied the template to all pulse events. By using Mn K$_\alpha$ and Mn K$_\beta$, we obtained the PHA-to-energy relation and converted PHA to energy by the quadratic function. Then, we fitted Mn K$_\alpha$ spectra using Voight function Equation (6.4). The results of 3 channels are shown in Figure 7.3, 7.4, and 7.5. The energy resolutions of 3 channels were around 10 eV at 5.9 keV. From the noise spectrum, we found the noise that is remarkably increased in low frequency. In order to study the origin of this low frequency noise, we divided the noise spectra to components of noise; the Johnson noise of the TES δI_{J}^2, the phonon noise δI_{ph}^2, and the readout noise δI_{R}. The Johnson noise of the TES and the phonon noise were calculated by Equation (4.106) and (4.100). The readout noise which means the SQUID noise and the electric circuit in room temperature and was calculated by subtracting the Johnson noise of the TES when the TES was normal state from total measured noise. The measured noise δI_{m} is expressed

$$\delta I_{\text{m}}^2 = \delta I_{\text{J}}^2 + \delta I_{\text{ph}}^2 + \delta I_{\text{R}}^2. \tag{7.1}$$

Fig. 7.3 Pulse collection results in Channe 1 with ^{55}Fe isotope at 60 mK bath temperature: Mn Kα averaged pulse(top left), averaged noise spectra (top right), template (2nd top left), S/N (2nd top right), baseline spectra (bottom left), Mn Kα energy spectra (bottom right).
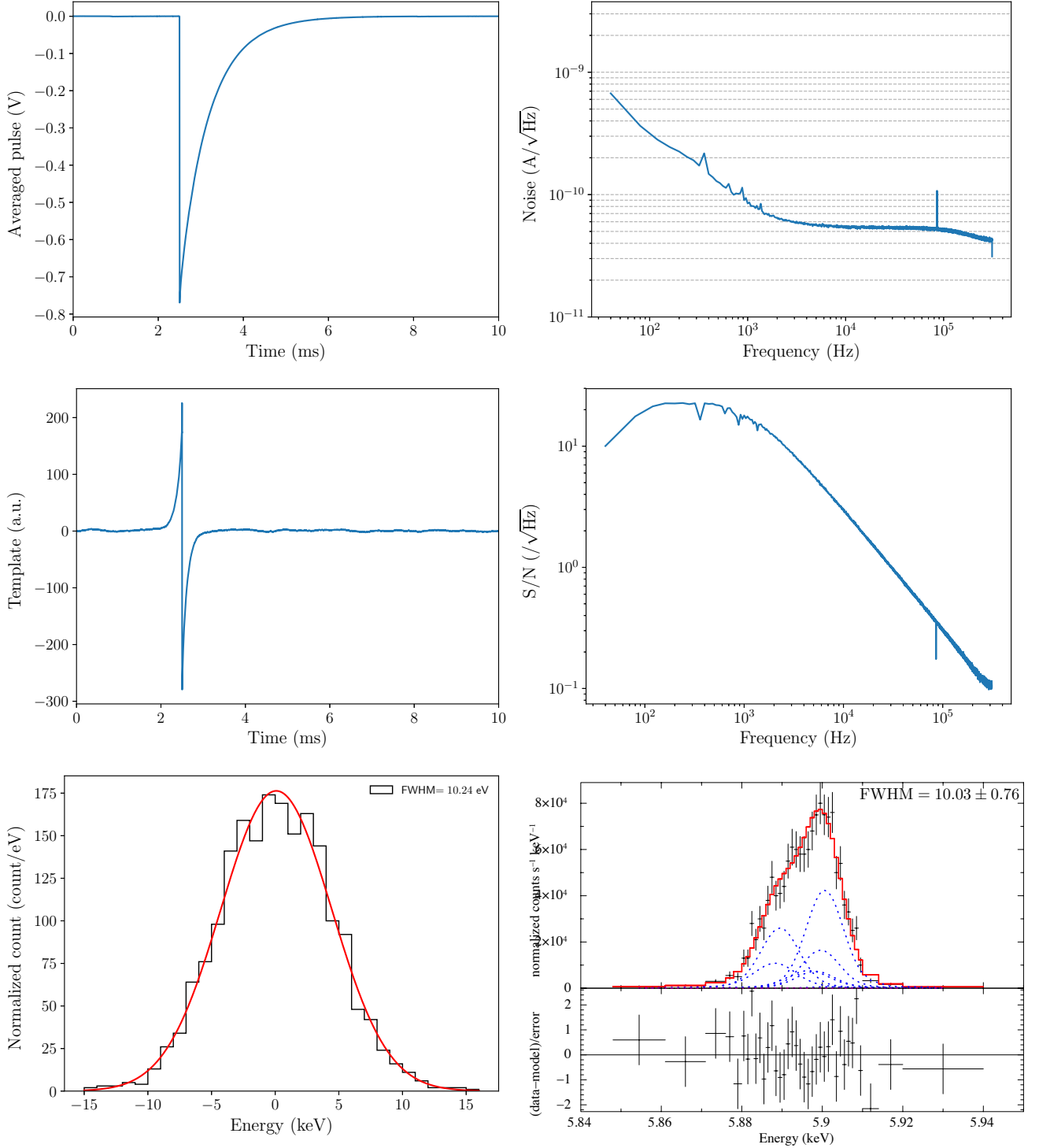
Fig. 7.4 Pulse collection results in Channe 2 with ^{55}Fe isotope at 60 mK bath temperature: Mn Kα averaged pulse (top left), averaged noise spectra (top right), template (2nd top left), S/N (2nd top right), baseline spectra (bottom left), Mn Kα energy spectra (bottom right).
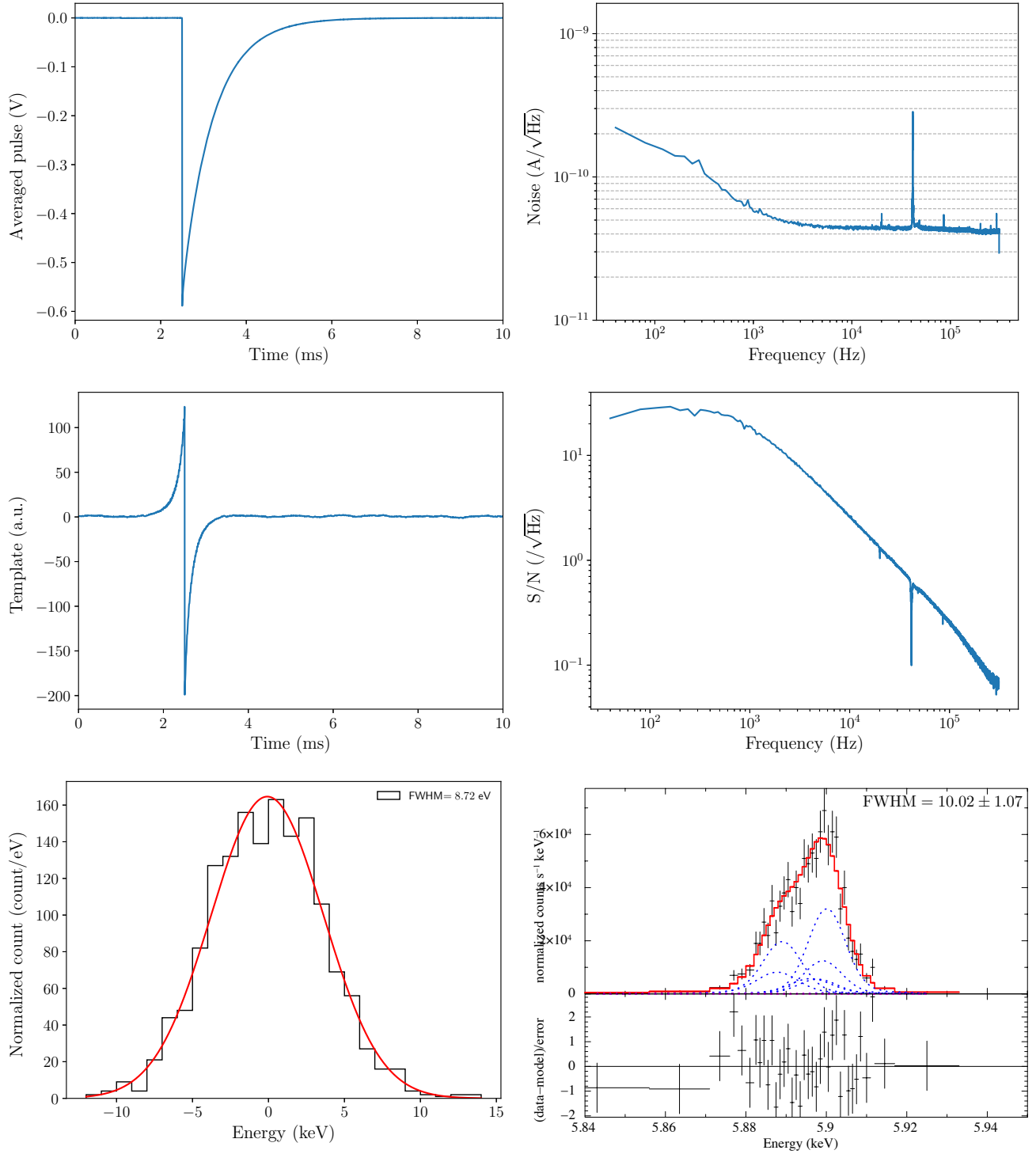
Fig. 7.5   Pulse collection results in Channe 3 with ^{55}Fe isotope at 60 mK bath temperature: Mn Kα averaged pulse (top left), averaged noise spectra (top right), template (2nd top left), S/N (2nd top right), baseline spectra (bottom left), Mn Kα energy spectra (bottom right).
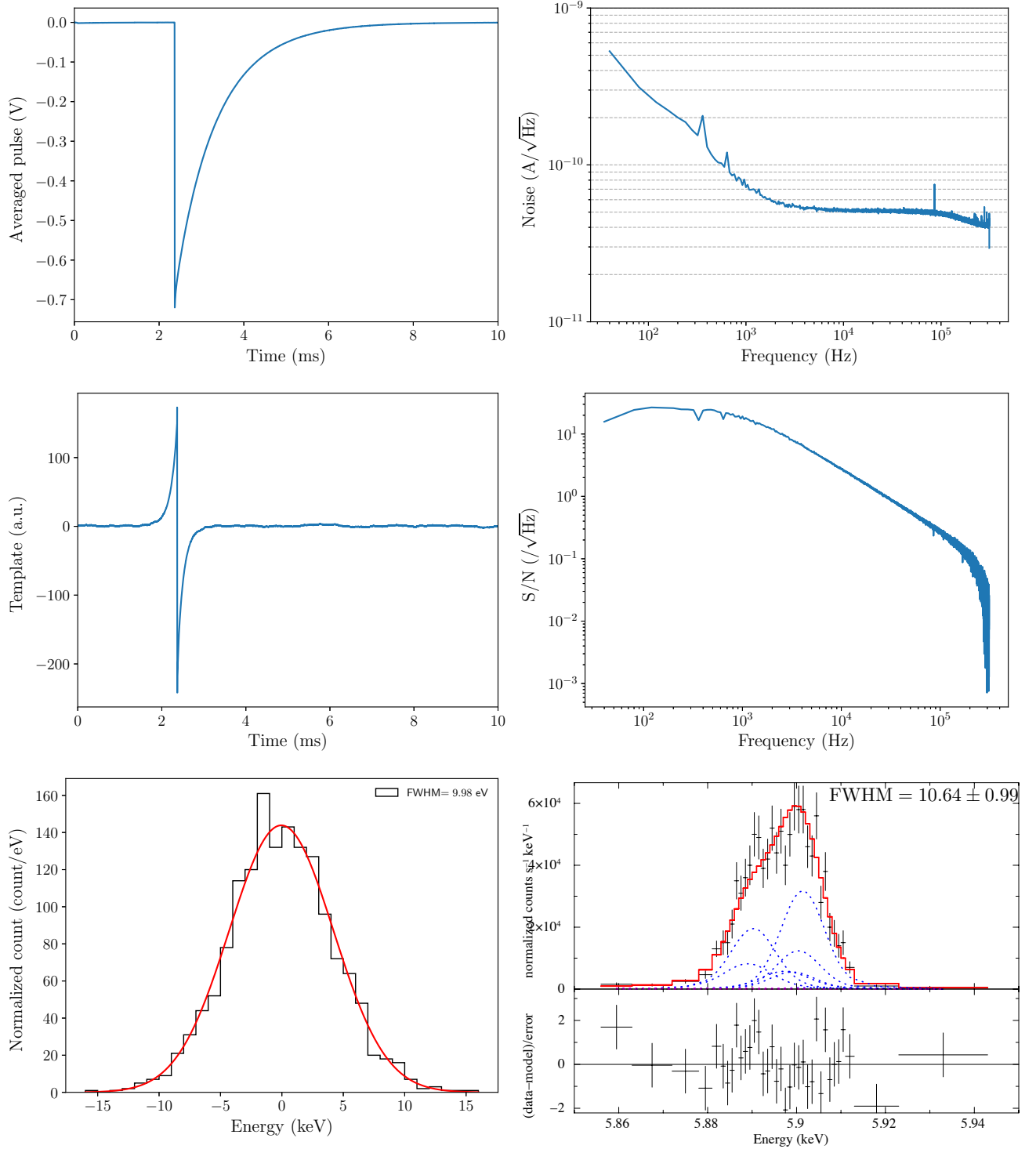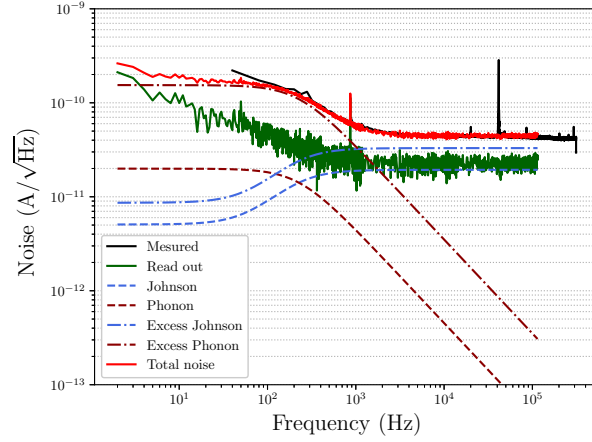
Fig. 7.6 Noise spectra and these components in Channel 1: measured noise (black), readout noise (green), Johnson noise (blue dashed), phonon noise (brown dashed), excess Johnson noise (blues dash-dot), excess phonon noise (brown dash-dot).
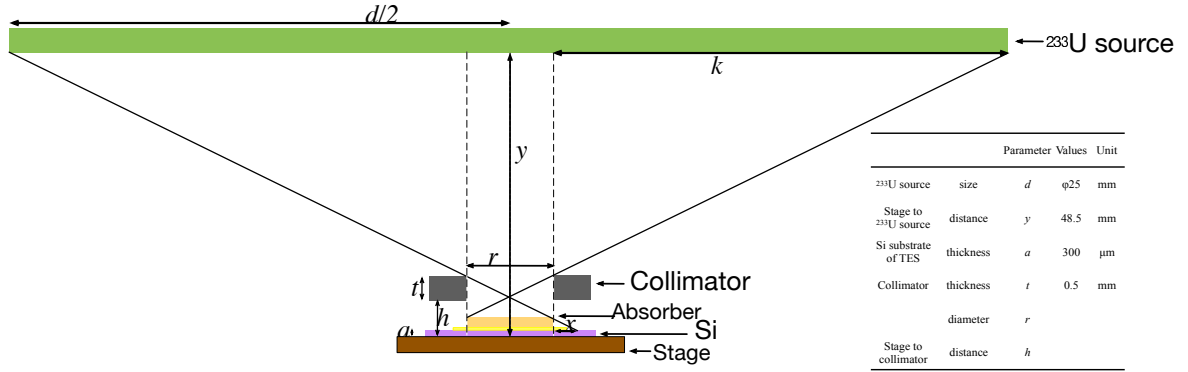
Fig. 7.7 Schematic layout of TES, collimator, and ^{233}U source: d is the diameter of ^{233}U source, y is the distance between the state to ^{233}U source, k is the expected area for the ^{233}U source from the absorber edge, r is the diameter of the collimator, t is the thickness of a collimator, h is the distance between the collimator and the stage, and a is the thickness of the silicon substrate.

However, in this measurement, we found the excess noises with the Johnson noise like distribution $\delta I_{\mathrm{exJ}}^2$ the phonon noise like distribution $\delta I_{\mathrm{exph}}^2$, thus we expressed the measured noise as

$$\delta I_{\mathrm{m}}^2 = \delta I_{\mathrm{J}}^2 + \delta I_{\mathrm{ph}}^2 + \delta I_{\mathrm{R}}^2 + \delta I_{\mathrm{exJ}}^2 + \delta I_{\mathrm{exph}}^2. \tag{7.2}$$

We found the excess phonon noise from TES itself increased the low-frequency noise. Thus the increase of the noise in low frequency was likely due to excess phonon noise and not due to the thermal fluctuation of the Si substrate.

7.3 Design and Fabrication Result of Collimator

In order to prevent the thermal fluctuation due to γ-ray absorption at the Si substrate of the TES device, we decided to install a collimator and designed it. The collimator was placed closely above the TES and mounted on the detector head (Figure 7.7) and also absorbed the photons decay from the ^{233}U source. We selected phosphor
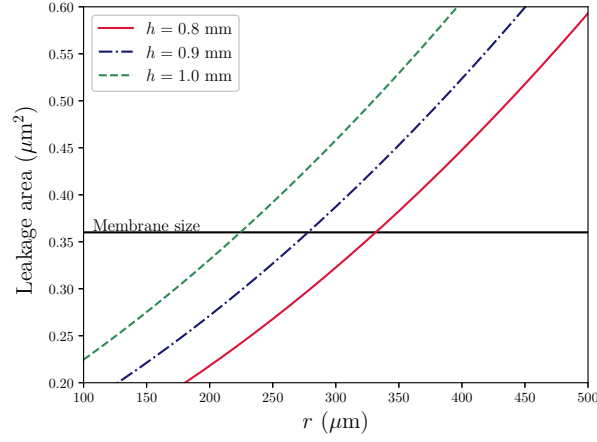
Fig. 7.8 Diameter of collimator r vs leakage area: the distance between the stage and the collimator is changed from 0.8 mm to 1.0 mm and black line shows the membrane size.
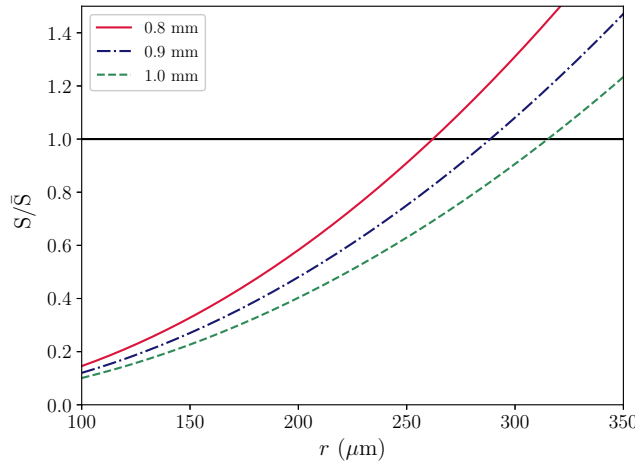
Fig. 7.9 Diameter of collimator, r, vs ration of area of ^{233}U source to expected area from the absorber edge: the distance between the stage and the collimator is changed from 0.8 mm to 1.0 mm

bronze as a material of the collimator which has similar linear expansion coefficient to copper, contains high Z atoms (^{50}Sn), and machine easily. First, we estimated the leakage area, x, through the collimator from the edge of the ^{233}U source (Figure 7.7). x is expressed as

$$x = \frac{h-a}{y-t-h} \cdot \left(\frac{d+r}{2}\right),\tag{7.3}$$

where y is the distance between the ^{233}U source and the TES, a is the thickness of silicon substrate of the TES, r is the diameter of the collimator, t is the thickness of the collimator, and d is the diameter of the ^{233}U source container. The parameters of y and d were limited by the refrigerator, and the values were 48.5 mm and 25 mm respectively. We used the Si wafer with the thickness (a) of 300 μm. We selected the thickness of the collimator as $t = 0.5$ mm and calculated the leakage area from the edge of the ^{233}U source through the collimator, which $(2x + r)^2$ and the result is shown in Figure 7.8. Next, we estimated whether the whole area of the ^{233}U source could be visible from the absorber through the collimator. We denoted the outer edge on the ^{233}U source which
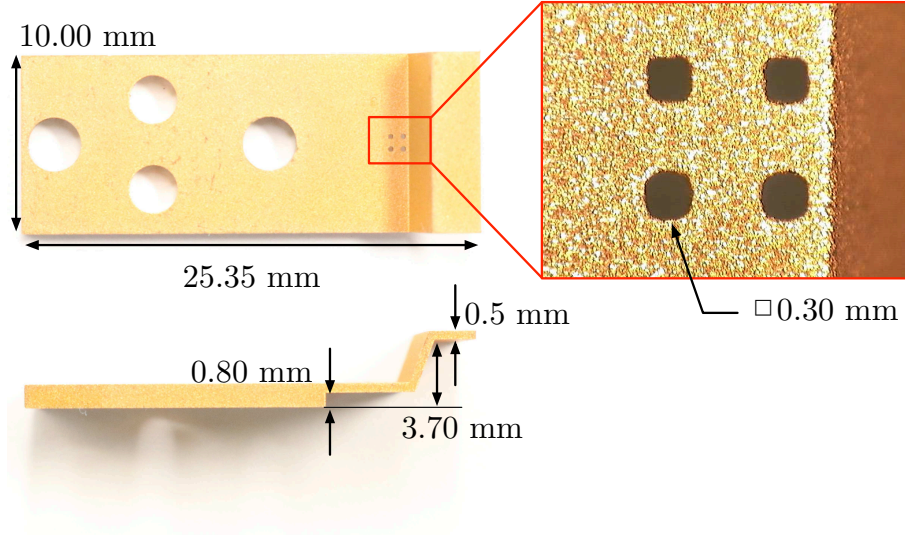
Fig. 7.10 Designed collimator: the thickness of the collimator is 0.5 mm, the diameter is 0.3 mm, and the distance between the collimator and the stage is 0.8 mm

Table 7.5 Design parameter of the collimator

	Values	Unit
Diameter	0.3	mm
Thickness	0.5	mm
Stage-to-collimator distance	0.8	mm

the absorber can see through the collimator by the length k as shown in Figure 7.7. Then the total area of the ^{233}U source which the absorber can see will be,

$$S = \pi \cdot \left(k + \frac{r}{2} \right)^2, \tag{7.4}$$

$$= \pi \cdot \left(\frac{y - a}{t + h - a} - \frac{1}{2} \right)^2 r^2. \tag{7.5}$$

Figure 7.9 shows the diameter of the collimator and the ration of the expected area S to the area of the ^{233}U source ($\bar{S} = \pi(d/2)^2 = 491$ mm^2). From both results (Figure 7.8, Figure 7.9), we selected the diameter of the collimator as 300 μm and the distance between the collimator and the stage as 0.8 mm to satisfy that the leakage area is below the membrane area and the absorber can see the whole area of the ^{233}U source through the collimator. We summarized the design parameter of the collimator in Table 7.5. This collimator was fabricated by the JAXA machine shop and the fabricated results are show in Figure 7.10.

7.4 Evaluation of the collimator at Tohoku University

We attached the collimator to the cryogenic detector stage and the picture of the detector head and the close-up view of the collimator are shown in Figure 7.11. We tried to read out 4 pixels of the TES and installed the cryogenic detector stage to the refrigerator at Tohoku University (Figure 7.12). However, due to the trouble of wirings in the refrigerator, we could read out 3 pixels which we call Channel 2, Channel 3, and Channel 4. Channel 4 is a device which we could not evaluate the performance at ISAS due to the absence of room wirings.
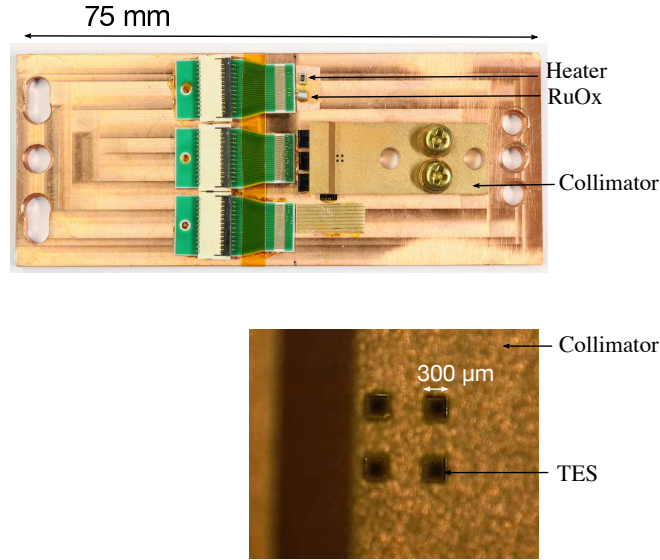
Fig. 7.11 Cryogenic detector stage (top) and close up view of the collimator (bottom)
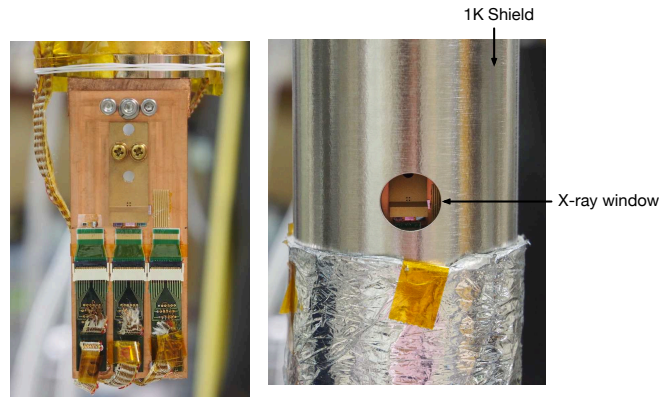
Fig. 7.12 Mounting to the refrigerator: the cryogenic detector stage mounted to the cold head of the refrigerator (left) and the cryogenic detector covered by the magnetic shield which we can see the collimator through the X-ray window (right)

In order to evaluate the effect of collimator, we measured the noise spectrum of the TES which channel number is 2, at the operating points at 65 mK with and without ^{233}U source which intensity was 110 MBq(Figure 7.13). When the ^{233}U source was irradiated, the low-frequency noise increased by a factor of 1.5 compared to that without the source, while the noise increased was by a factor of 3 with the ^{233}U source in Oarai test. We thus considered the increase of low frequency noise became small by the effect of the collimator.

7.5 Evaluation of TES-performance at Tohoku University

First, we checked the $R - T$ relation of 3 pixels and found the transition temperatures did not change from ISAS measurements, $T_c \sim 123$ mK (Figure 7.14). We evaluated the performance of all 3 pixels at 65 mK using the ^{241}Am source (Table 6.8) because the minimum achieved temperature in the refrigerator was 58 mK. The parameters during the ^{241}Am irradiation test are summarized in Table 7.6. We analyzed each channel separately. For example channel 3, we obtained the 452 pulses for 26 keV γ-ray and generated template by using average pulse of 26 keV γ-ray and noise records. Then, the template was applied to all pulse events and PHAs were
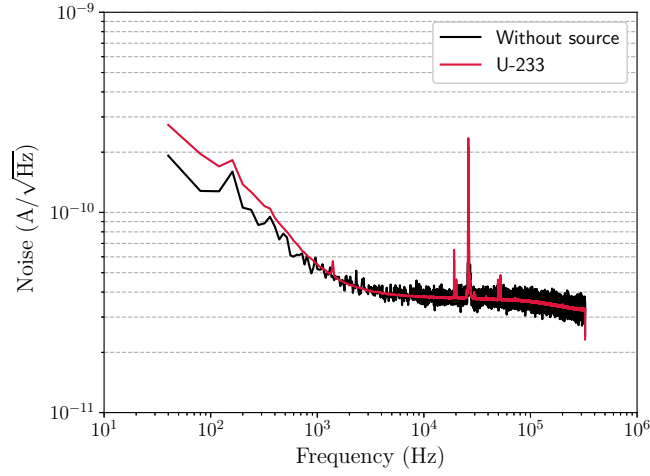
Fig. 7.13   Noise spectra of the TES in channel 2, with attached the collimator at 65 mK:the noise spectra without source(black) and the noise spectra with ^{233}U source (red). We found a only slight degradation even when ^{233}U and ^{133}Ba source was attached
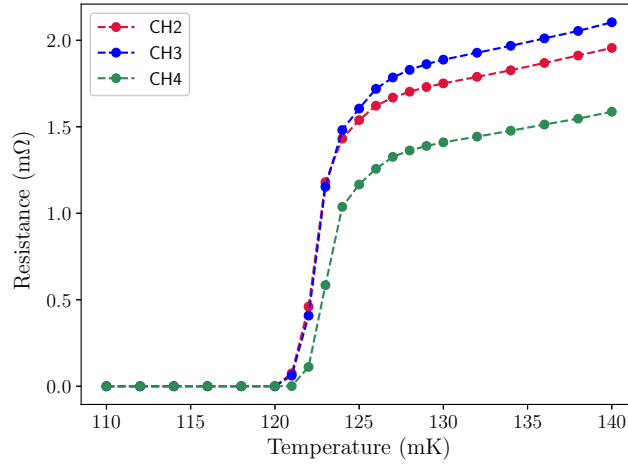
Fig. 7.14 $R - T$ results of 3 pixels

obtained. In this time, we used 5 lines, Np L$_{\alpha 1}$, Np L$_{\beta 1}$, Np L$_{\gamma_1}$, 26 keV, and 59 keV, for the calibration lines and fitted the relation between the PHA and the energy by the spline function. We converted the PHA to energy and fitted the energy spectrum of 26 keV with the gaussian function. Results of all 3 pixels are shown in Figure 7.15, 7.17, 7.16. The energy resolutions at 26 keV were 15 eV of channel 3 and channel 4 and the energy resolution of channel 2 was 18 eV. The energy resolutions almost satisfied the requirements (FWHM = 15 eV).
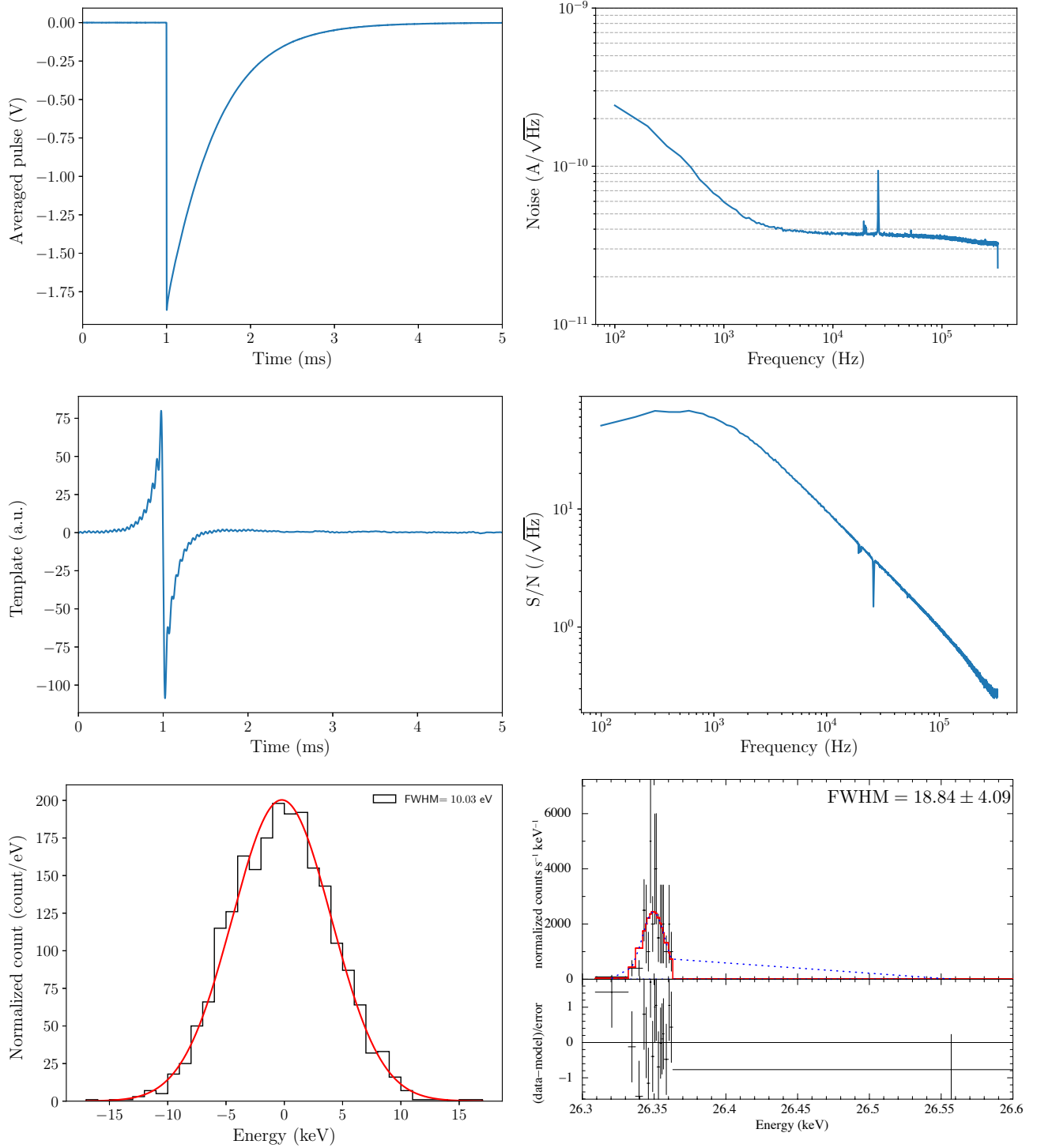
Fig. 7.15 Pulse collection results with ^{241}Am isotope in Channel 2 at 65 mK bath temperature at Tohoku Univ. :^{241}Am 26 keV averaged pulse(top left), averaged noise spectra (top right), template (2nd top left), S/N (2nd top right), baseline spectra (bottom left), ^{241}Am26 keV energy spectra (bottom right).
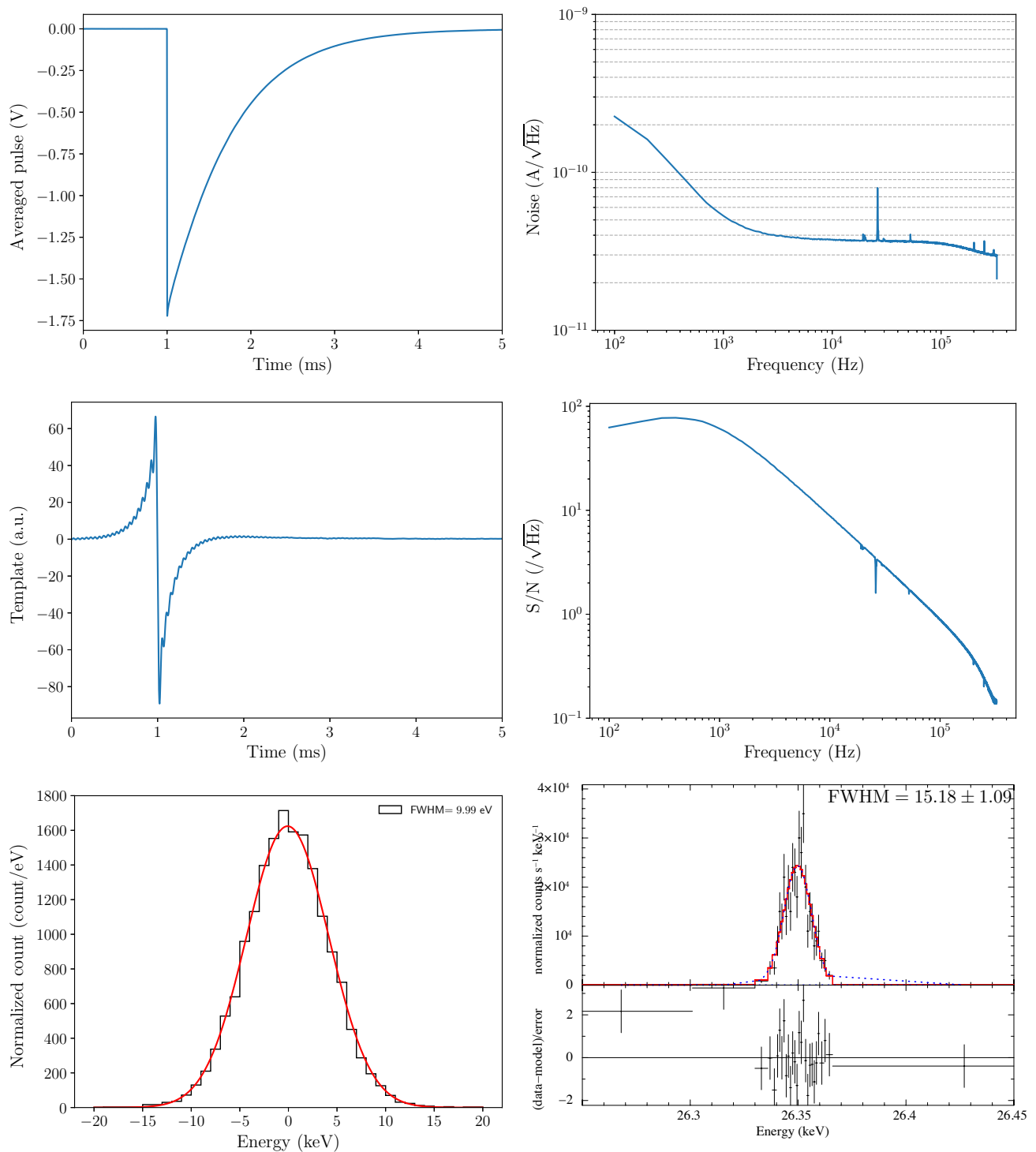
Fig. 7.16   Pulse collection results with ^{241}Am isotope in Channel 3 at 65 mK bath temperature at Tohoku Univ. :^{241}Am 26 keV averaged pulse(top left), averaged noise spectra (top right), template (2nd top left), S/N (2nd top right), baseline spectra (bottom left), ^{241}Am 26 keV energy spectra (bottom right).
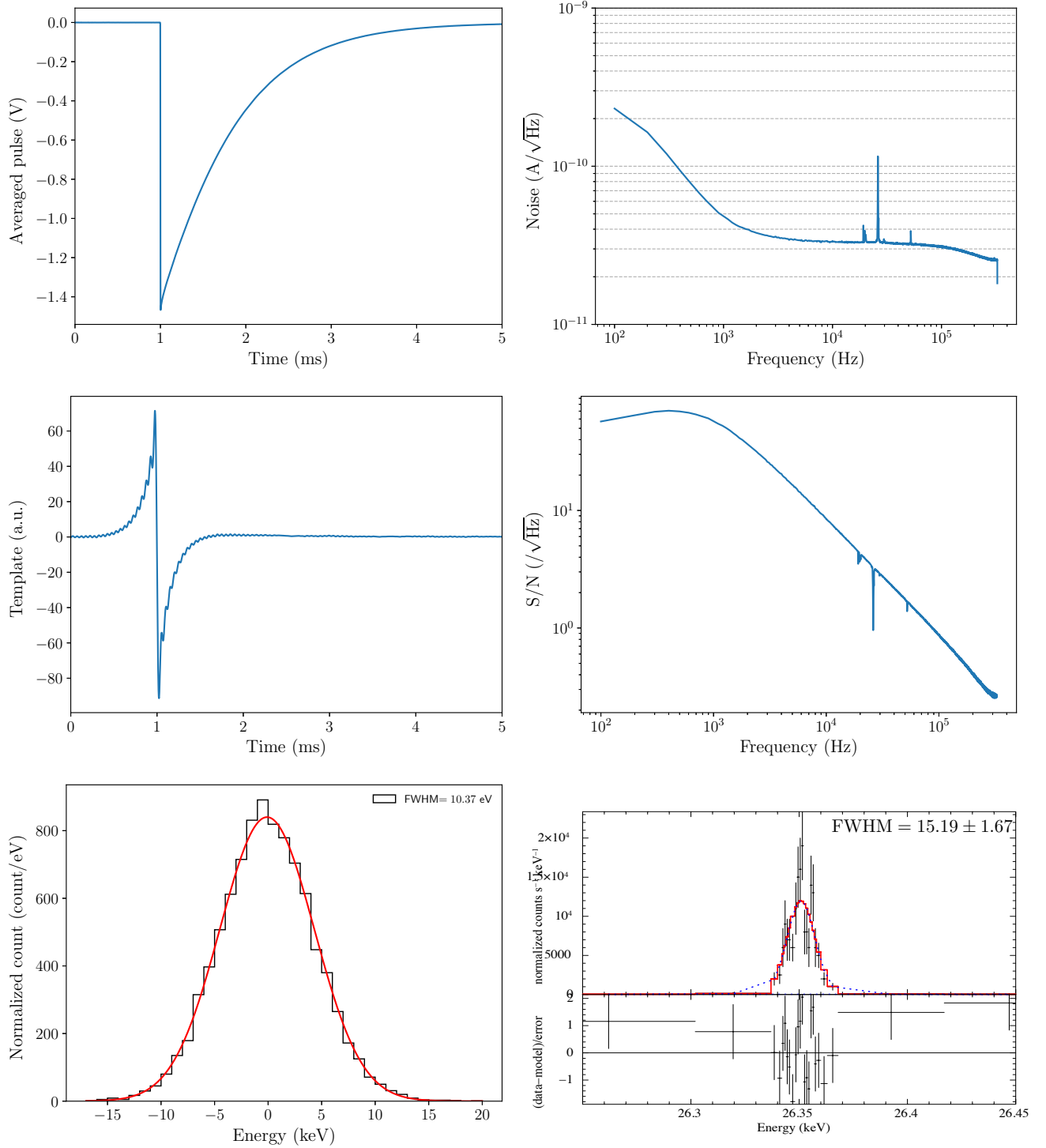
Fig. 7.17   Pulse collection results in channel 4 with ^{241}Am isotope at 65 mK bath temperature at Tohoku Univ. :^{241}Am 26 keV averaged pulse(top left), averaged noise spectra (top right), template (2nd top left), S/N (2nd top right), baseline spectra (bottom left), ^{241}Am 26 keV energy spectra (bottom right).

Table 7.6   Parameters of 3 pixels during ^{241}Am irradiation test at 65 mK

		Unit	CH2	CH3	CH4
Current following TES	I_{tes}	μA	77.0	69.5	63.8
Resistance of TES	R_{tes}	mΩ	9.75	10.4	11.2
Resistance ration to normal resistance	$R_{\text{tes}}/R_{\text{N}}$	%	33	31	36
Temperature of TES	T_{tes}	mK	149	130	131
Thermal conductance	G	nW/K	1.25	1.69	1.33
Loop gain	$\mathcal{L}$		4.9	4.1	3.6
Temperature sensitivity	α		15	18	13

Table 7.7   Baseline resolution and energy resolution at 26 keV of CH2, CH3, CH4 with ^{241}Am at 65 mK

	Unit	CH2	CH3	CH4
Baseline resolution @65 mK	(eV)	10.03	9.99	10.37
Energy resolution @65 mK	(eV)	18.84 ± 4.00	15.18 ± 1.09	15.19 ± 1.67

Chapter 8

Future Prospects

In the Tohoku University test, we could operate the refrigerator and obtain the energy resolution of the TES devices as to be 18 eV. However, the cooling power with the refrigerator degraded and we could not operate the refrigerator at 65 mK after the irradiation test using the ^{241}Am isotope. We suspected that the ^{3}He circulation line was partially clogged as the cause of the degradation. Thus, we changed the bath temperature to 90 mK to operate longer time and decided how to add the calibration lines. In addition to this, we estimated whether we could separate 29.19 keV doublet with the energy resolution as to be 18 eV.

8.1   Selection of Calibration Sources

In order to improve the systematic error, we added the calibration sources whose photon-energies are closely our interest energies. We selected the added calibration sources to Te K lines, I K lines, and Gd K lines. The energy are shown in Table A.2. We used an X-ray generator to excite the Te K and I K lines to control the count rate easily. Because the voltage range of this X-ray generator was limited below 50 kV, it was difficult to excite the Gd K lines whose energies are around 42 keV. Thus, we used the ^{241}Am source to excite the Gd K lines. The secondary targets, the Te powder, the CsI crystal, and the Gd thin film and the X-ray generator are shown in Figure 8.1. We obtained the energy spectra of the channel 2 from the CsI crystal and the Te sample excited by the X-ray generator respectively.

When we measured the I K lines and the Cs K lines energy spectrum from the CsI crystal, the X-ray generator was operated with 50 kV and 10 μA. We corrected 1500 pulses and noises and generated template using the I K$_\alpha$ average pulse and the noise records. The PHA centroid values of I K$_{\alpha 1}$, I K$_{\alpha 2}$, Cs K$_{\alpha 1}$, and Cs K$_{\alpha 2}$ were obtained by the model fitting in the PHA spectra and were converted to energy by the quadratic function. The whole energy spectra is shown in Figure 8.3 (top) and the I K$_\alpha$ and Cs K$_\alpha$ lines spectrum are shown in Figure 8.3 (bottom). Next, we measured Te K lines excited by the X-ray generator operated with 50 kVand 7 μA. We corrected 1140 pulses and noise records and generated template using the Te K$_\alpha$ average pulse and the noise records. By the model fitting ofPHA spectrum of Te K$_{\alpha 1}$, Te K$_{\alpha 2}$, Te K$_{\beta 1}$, we converted PHA to energy with the quadratic function. The whole energy spectrum of Te K lines and energy spectra of Te K$_{\alpha 1}$ and Te K$_{\alpha 2}$ are shown in Figure 8.4. We summarized the count rate for I K$_\alpha$, Cs K$_\alpha$, Te K$_\alpha$ in Table 8.1.

Table 8.1   Count rate of I K$_\alpha$,Cs K$_\alpha$, Te K$_\alpha$

Line	Count rate(/s)
I K$_\alpha$	0.07
Cs K$_\alpha$	0.04
Te K$_\alpha$	0.19
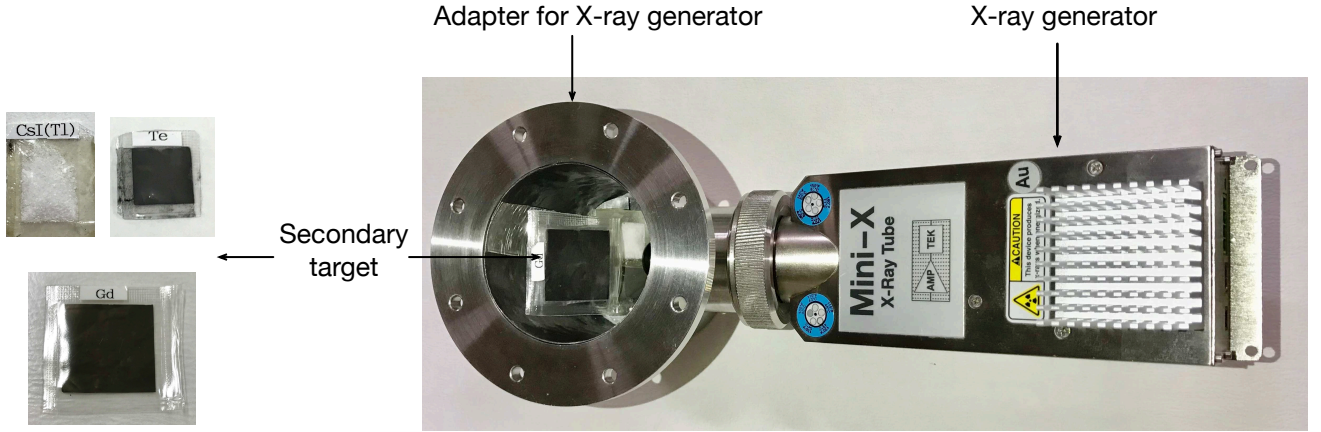
Fig. 8.1   X-ray generator and secondary targets for 29 keV and 42 keV calibration lines
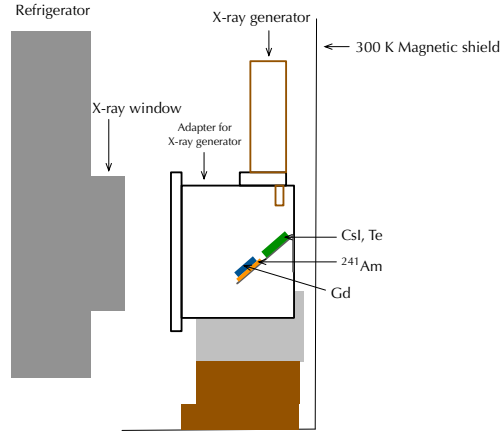
Fig. 8.2   Schematic layout view of refrigerator and the system of calibration lines

8.1.1   Consideration of X-ray generator usage

When we use an X-ray generator, we have to be careful about continuum components emitted by the X-ray generator. We estimated the impact of the continuum emission to the most important 29.19 keV line analytically. Here we assumed that the energy spectrum can be expressed as a gaussian distribution. The number of counts $\bar{S}$ of the line spectrum obtained by experiment is calculated as

$$\bar{S} = S + B - \bar{B}, \tag{8.1}$$

where $S + B$ is obtained photon counts from experiments and $\bar{B}$ is an estimated background level within the energy range of δE (Figure 8.5). $\bar{B}$ is calculated from an energy range. If the background level is constant, we calculate $\bar{B}$ using the spectrum from the nearby energy range of $k\delta E$. The statistical error $\sigma(S)$ by the Poisson statistics to the estimated value of $\bar{S}$ is

$$\sigma(S)^2 = S + B + \sigma(B)^2, \tag{8.2}$$
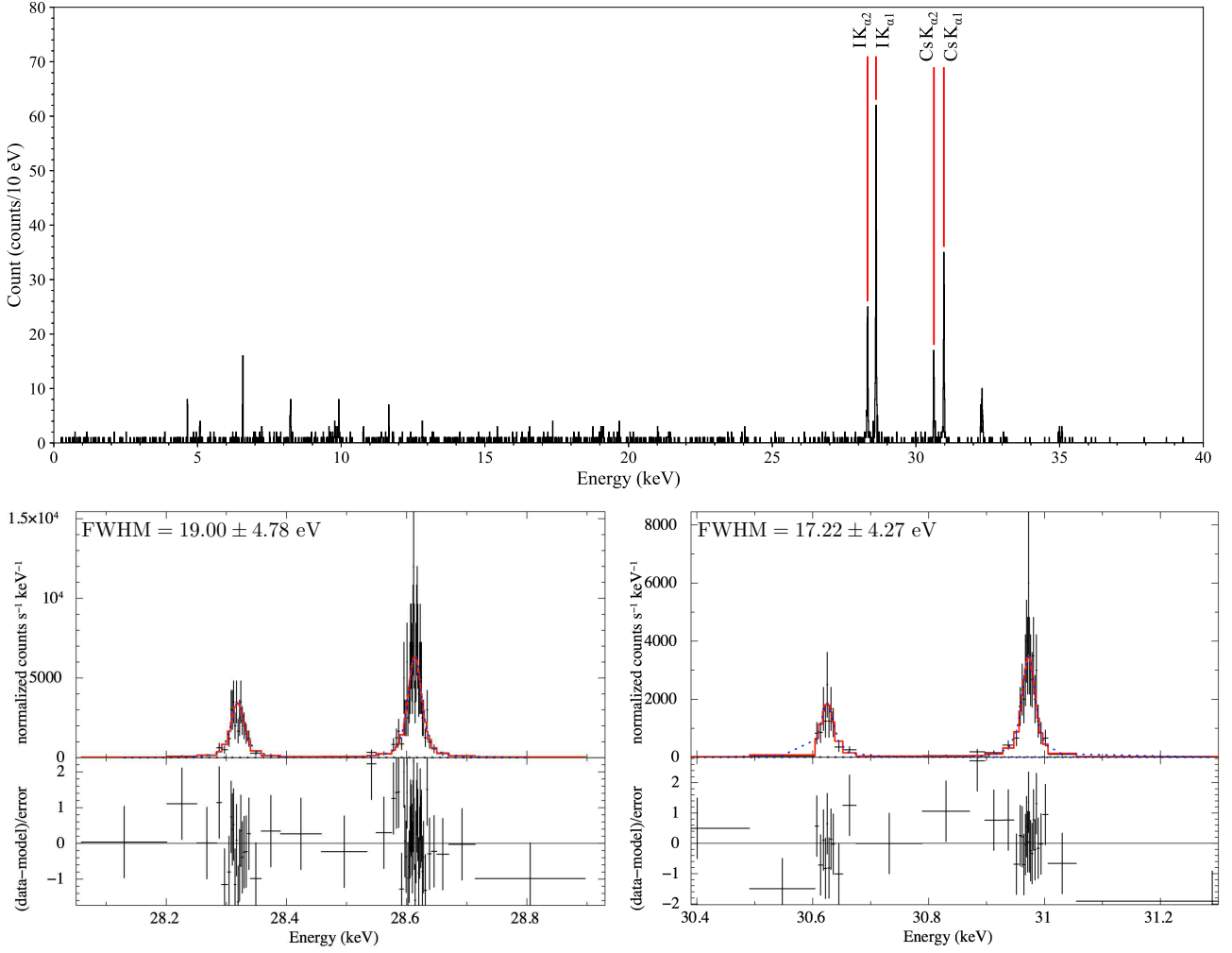
Fig. 8.3 Energy spectra of Cs K lines and I K lines which excited by X-ray generator: The energy spectra between I K$_\alpha$ and Cs K$_\beta$ (top), I K$_\alpha$ energy spectra that the energy resolution was 19 eV (bottom left) , Cs K$_\alpha$ energy spectra that the energy resolution was 17 eV (bottom right).

where $\sigma(B)$ is the Poisson error to estimated value of $\bar{B}$ and is denoted as

$$\sigma(B)^2 = \frac{B\delta E}{k\delta E} = \frac{B}{k}. \tag{8.3}$$

The signal to noise ration (S/N) is expressed as

$$S/N = \frac{S}{\sqrt{S + B(1 + \epsilon)}}, \tag{8.4}$$

$$= \frac{\sqrt{S}}{\sqrt{1 + \frac{\Delta E}{\delta W} a(1 + \epsilon)}}. \tag{8.5}$$

We defined δW using background level b (counts/keV) as

$$\delta W \equiv \frac{S}{b}. \tag{8.6}$$
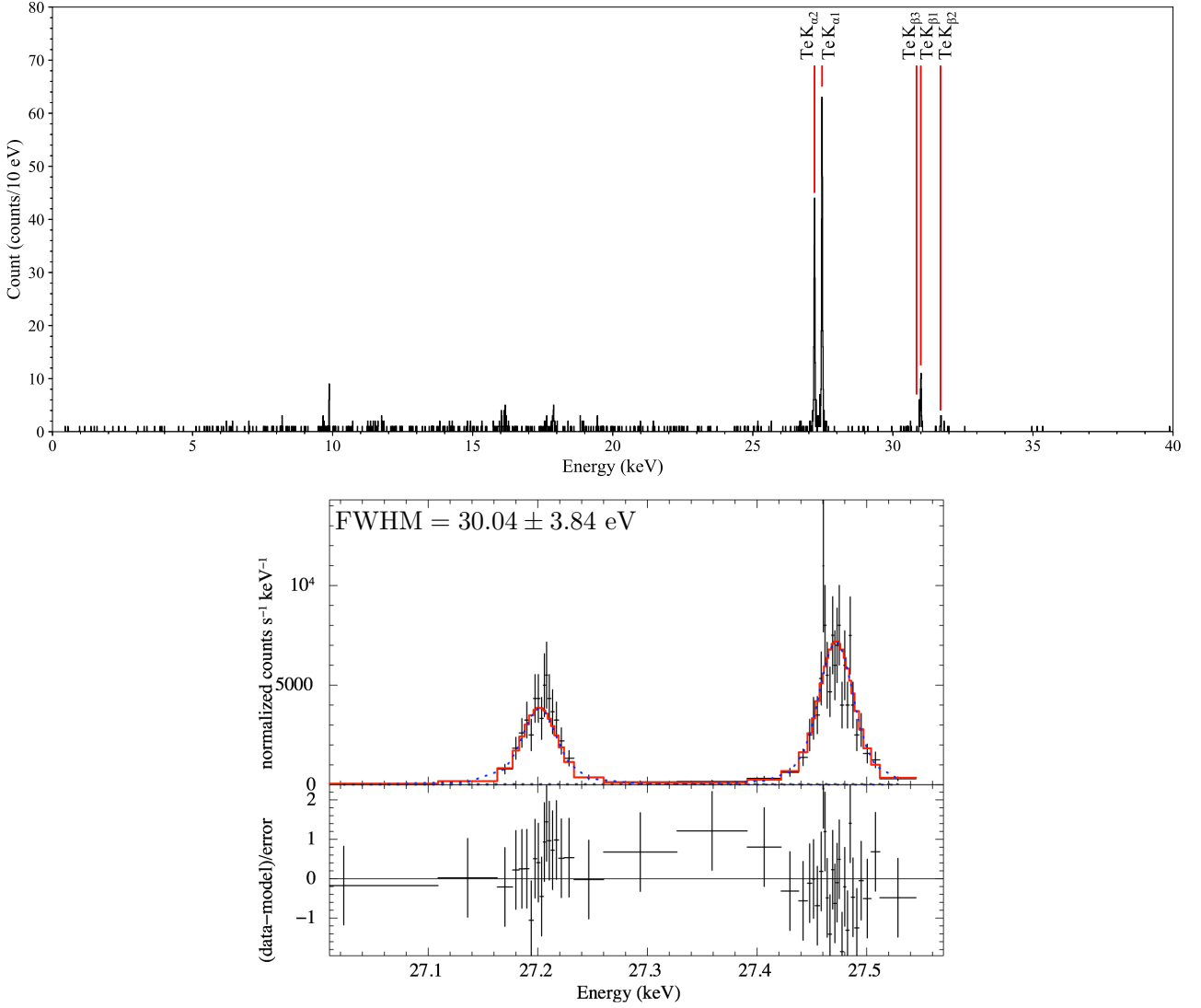
Fig. 8.4   Energy spectra of Te K lines which excited by X-ray generator: The energy spectra between Te K$_\alpha$ and Te K$_\beta$ (left) ,Te K$_\alpha$ energy spectra that the energy resolution was 19 eV(right)

This value is called an equivalent width and it expresses the energy width of background which equals to the area of line spectrum. We introduced the energy resolution ΔE of the detector, that is FWHM, and expressed as

$$\delta E = a\Delta E. \tag{8.7}$$

In this case, $a(1+\epsilon) \sim O(1)$ due to $a = 2\sqrt{2\ln 2} \sim 2.35$ and $1+\epsilon \sim 1$. If the equivalent width is larger than the energy resolution ($\delta W > \Delta E$) , the S/N becomes

$$S/N \sim \sqrt{S}, \tag{8.8}$$

and the background can be negligible. In contrast, if the equivalent width is smaller than the energy resolution, the S/N becomes

$$S/N \sim \frac{\sqrt{S}}{\sqrt{\frac{\Delta E}{\delta W}a(1+\epsilon)}}. \tag{8.9}$$
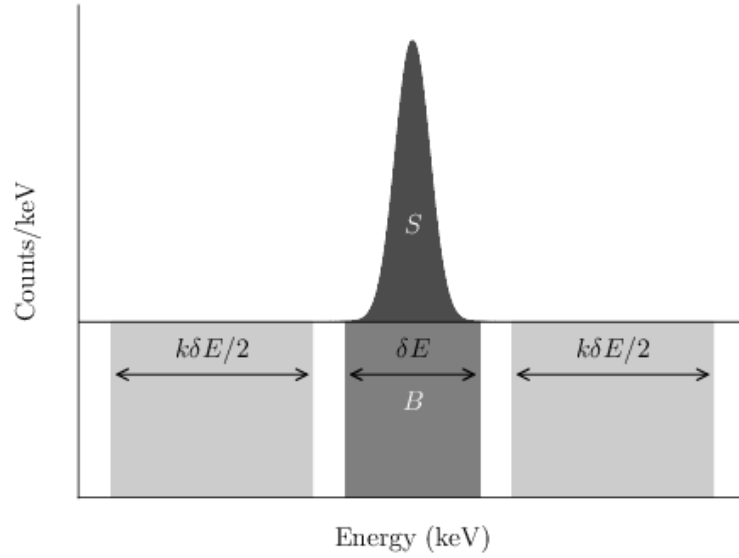
Fig. 8.5   Ideal spectra assuming the Poisson statistics

and the background can not be negligible because the denominator of the right hand side in Equation (8.9) larger than unity, and the S/N get worse. We set the ^{233}U source and the X-ray generator in this order from the X-ray window of the refrigerator and estimated the equivalent width of 29.19 keV when the X-ray generator also is operating. The background counts consisted of the background decay from the ^{233}U source ($B_U(29)$) and the background excited from the X-ray generator ($B_U(I\ K_{\alpha 1})$, however we cannot separate them. First, we obtained the signal $S_U(29)$ and background counts of 29.19 keV decay from the ^{233}U source. Next, to estimate the background counts excited from the X-ray generator, we measured the signal $S(I\ K_{\alpha 1})$ and background counts $B(I\ K_{\alpha 1})$ of I $K_{\alpha 1}$ when the X-ray generator is only operating and measured the signal counts $S_U(I\ K_{\alpha 1})$ with the ^{233}U source to consider the absorption by the ^{233}U source. Then, the $B_U(I\ K_{\alpha 1})$ is expressed as

$$B_U(I\ K_{\alpha 1}) = B(I\ K_{\alpha 1}) \cdot \frac{S_U(I\ K_{\alpha 1})}{S(I\ K_{\alpha 1})} \tag{8.10}$$

Thus the equivalent width is estimated to be

$$\delta W = \frac{S_U(29)}{B_U(29) + B(I\ K\alpha_1) \cdot \frac{S_U(I\ K_{\alpha 1})}{S(I\ K_{\alpha 1})}}. \tag{8.11}$$

We obtained the intensity and background of 29.19 keV from the irradiation test with the ^{233}U source for 540313 s. From the model fitting of the energy spectrum, we found the $S_U(29) = 22/540313 = 4.07 \times 10^{-5}$ (counts/s), $B_U(29) = 195/540313 = 3.6 \times 10^{-4}$ (counts/s/keV) and the equivalent width to 29.19 keV of the ^{233}U source was $\delta W_U = S_U(29)/B_U(29) = 0.113$ (keV) = 113 eV for the case without the X-ray generator. In the case, the equivalent width was larger than the energy resolution of 33 eV ($\delta W > \Delta E$) so the background dose not affect the signal. Then we estimated $S(I\ K_{\alpha 1})$ and $B(I\ K_{\alpha 1})$ from the irradiation test with the X-ray generator for 88472 s and the results were $S(I\ K\alpha_1) = 158/88472 = 1.79 \times 10^{-3}$ (counts/s) and $B(I\ K_{\alpha 1}) = 110/88472 = 1.24 \times 10^{-3}$ (counts/s/keV). We estimated the $S_U(I\ K_{\alpha 1})$ from the irradiation test with both the ^{233}U source and the X-ray generator for 67715 s and the results was $S_U(I\ K_{\alpha 1}) = 444/67715 = 6.56 \times 10^{-3}$ (counts/s). From Equation (8.11), the equivalent width of 29.19 keV was estimated to be 8.3 eV which was smaller than the energy resolution ($\delta W < \Delta E$). Thus, the continuum emission from the X-ray generator is not negligible and we decided
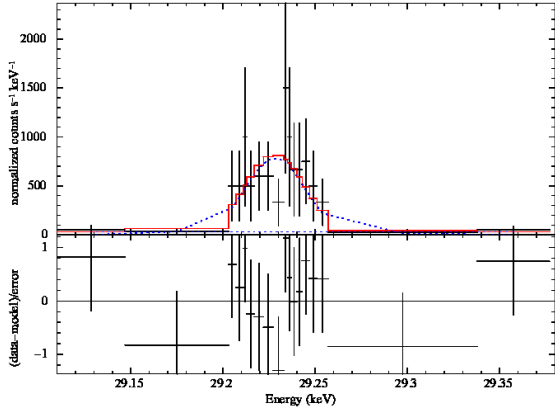
Fig. 8.6   Around 29.19 keV energy spectra with X-ray generator only
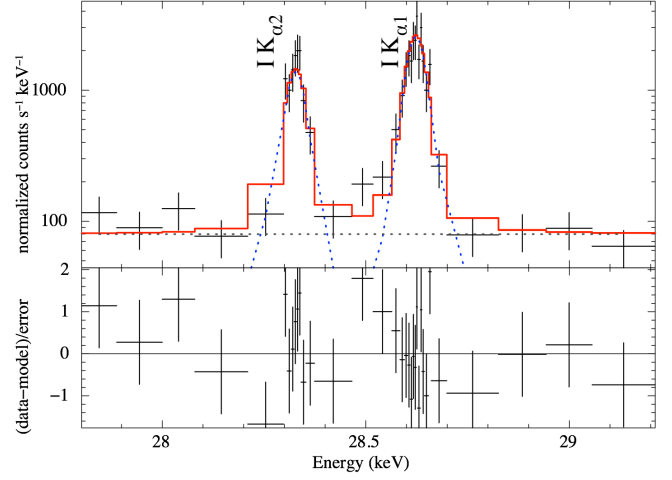
Fig. 8.7   I Kα_1 energy spectra with X-ray generator only
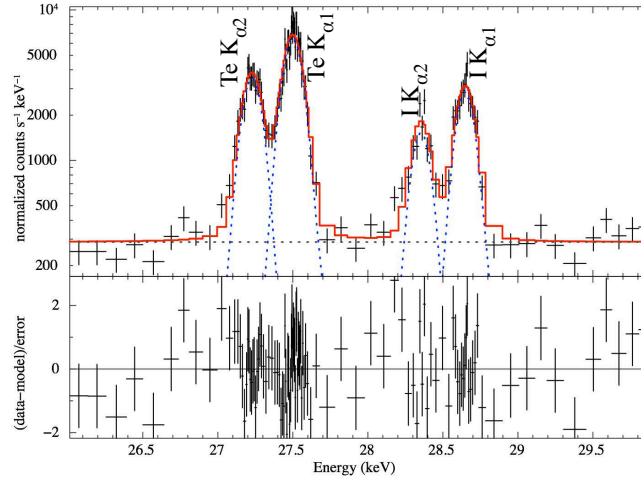
Fig. 8.8   I Kα_1 energy spectra with both ^{233}U source and X-ray generator

Table 8.2   Intensity and background of 29.19 keV and I Kα_1 with ^{233}U source and X-ray generator

	Unit	29.19 keV line with ^{233}U source irradiation	I Kα_1 with ^{233}U source and X-ray generator irradiation	I Kα_1 with X-ray generator irradiation
Intensity of signal	(counts/s)	4.07×10^{-5}	6.56×10^{-3}	1.79×10^{-3}
Intensity of background	(counts/s/keV)	3.6×10^{-4}	4.22×10^{-3}	1.24×10^{-3}

not to use X-ray generator when we performed the ^{233}U irradiation test and also to allocate calibration time during which the X-ray generator is used without the ^{233}U to obtain the calibration lines.

8.1.2   Calibration sources for regular use

Since we do not use the X-ray generator at all times, we selected the calibration lines for 29 keV and 42 keV for regular use. We selected the ^{133}Ba source that decays to Cs and emits Cs K$_\alpha$ and Cs K$_\beta$ as the 29 keV calibration line. To check how much the Cs K lines are absorber by the ^{233}U source in the case of set the ^{133}Ba source backwards the ^{233}U source, we calculated the absorption efficiency of U using a linear attenuation μ and
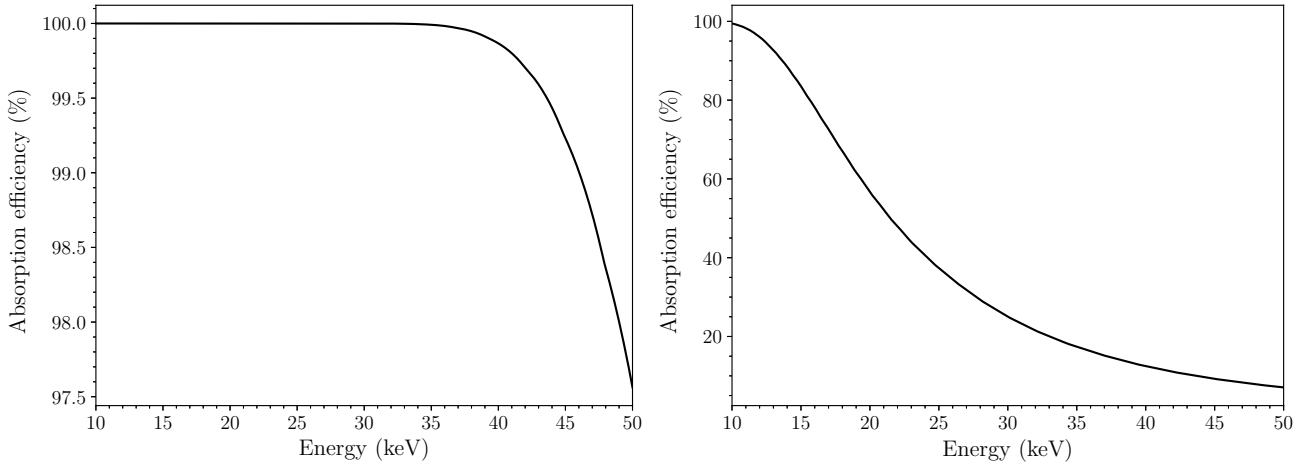
Fig. 8.9   Absorption efficiency vs energy : ^{233}U source with 1.145 g/cm^3 of density and 3 mm of thickness calculated by assuming ^{233}U is solid (left) and Gd with 7.9 g/cm^3 of density and 25 μm thickness
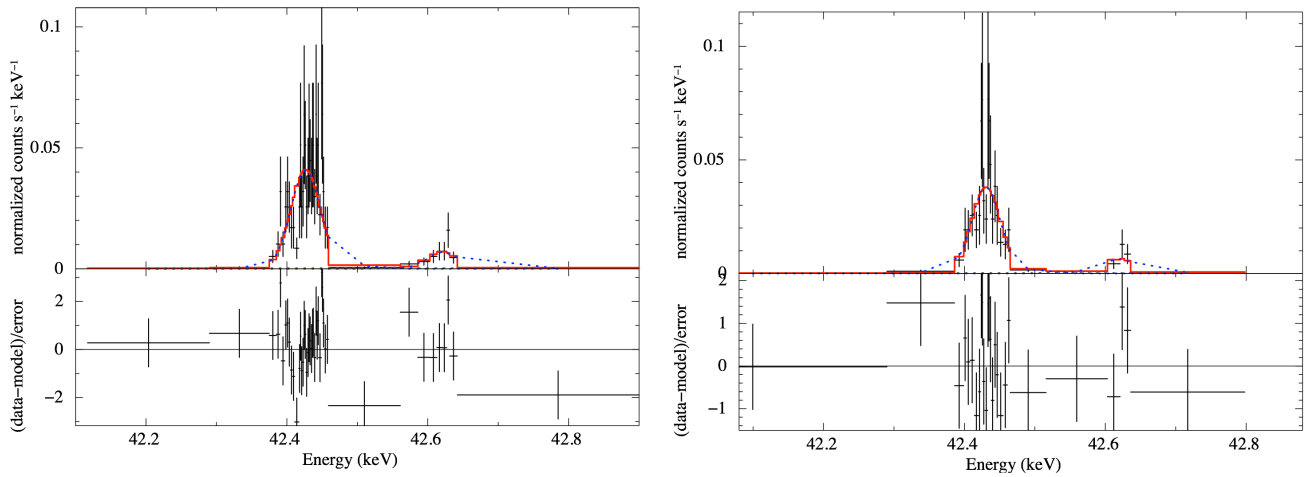
Fig. 8.10   42.43 keV and 42.63 keV energy spectrum: with ^{233}U source (left) and with ^{133}Ba source in front of ^{233}U source (right)

Table 8.3   Counts rate for usage calibration lines

Calibration line	Count rate (/s)	Count rate (/day)
Cs Kα_1	7.72×10^{-3}	667
Cs Kα_2	4.17×10^{-3}	361
Gd Kα_1	2.53×10^{-4}	22

a thickness of the source y

$$A = 100(1 - e^{-\mu y}) \ \%. \tag{8.12}$$

The linear attenuation was calculated by the density, 1.145 g/cm^3, and the thickness, 3 mm, of the ^{233}U source. Due to the absorption efficiency of the ^{233}U source (Figure 8.9), the 29 keV lines are absorbed almost 100 %. Thus we tried to set the ^{133}Ba source ahead of the ^{233}U source and checked whether 42 keV lines from the ^{233}U source were absorbed or not. The 42.43 keV line ($E'(\text{③} \rightarrow \text{⑤}, \text{③} \rightarrow \text{⑥})$) with the ^{233}U source was obtained 101 counts for 52149 s and the counts rate of 42.43 keV was 2 counts/s. On the other hand, in the case of the irradiation test with ^{133}Ba source in front of ^{233}U, the count rate was 2 counts/s (Figure 8.10). We found there
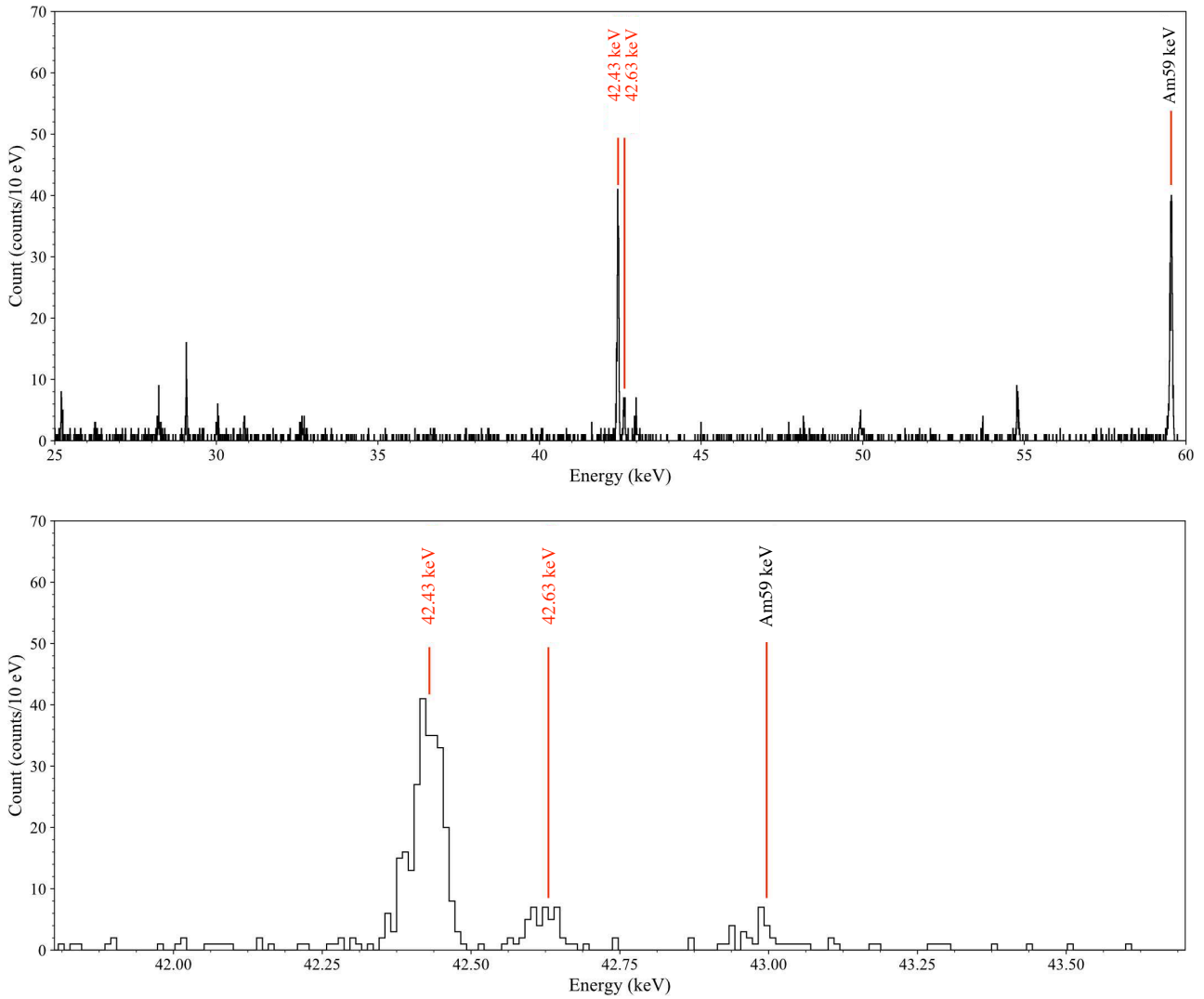
Fig. 8.11 Energy spectrum with ^{233}U, Gd, and ^{241}Am source : energy spectra between 25 keV and 60 keV (top), energy spectra close up around 42 keV (bottom)

is no absorption effect of the ^{133}Ba source and decided to set the^{133}Ba source in front of the ^{233}U source. We also calculated the count rate of Cs K$_{\alpha 1}$, and it was 667 counts/day (Table 8.3).

We used Gd metal as the 42 keV calibration line . From the calculation of absorption efficiency of Gd with 7.87 g/cm^3 density and 25 μm thickness, we found 29 keV lines are absorbed by 23 %. In order to avoid the decrease of counts rate of photons from the ^{233}U source, we set the Gd metal behind the ^{233}U source and in front of the ^{241}Am source to excite it. We measured the Gd K$_\alpha$ lines excited by the ^{241}Am source with the ^{233}U source and calculated the count rate of Gd K$_{\alpha 1}$. The energy spectrum is shown in Figure 8.11 and we found the 26 keV line from the ^{241}Am source is absorbed by the Gd metal. By the model fitting of the Gd K$_{\alpha 1}$, the counts rate of Gd K$_{\alpha 1}$ was 22 counts/day (Table 8.3). We confirmed the selected calibration sources emit the photons with the energy close to our target lines (29 keV and 42 keV).

Table 8.4 Count rate (/day) of 4 interested γ-ray of ^{229}Th

	Energy (keV)	Count rate (/day)			
		CH2	CH3	CH4	Total
$E'(③ \to ⑤, ③ \to ⑥)$	42.43	184	205	155	544
$E(② \to ④)$	42.63	45	42	18	105
$E'(④ \to ⑥, ④ \to ⑤)$	29.19	32	50	30	97
$E(② \to ③)$	29.39	3[*1]	4[*1]	2[*1]	9

8.2   Estimation of Distribution of the 29.19 keV Doublet

We measured the count rate for each channel of 29.19 keV, 29.39 keV, 42.43 keV, and 42.63 keV decay from the ^{233}U source at 90 mK bath temperature. We obtained the 19000 pulses and noises records for each channel and analyzed each channel separately in the same way. Template was generated by the Th Lα_1 average pulse and noise records, and then applied it to all pulses events. The PHA-to-energy relation was converted by the spline function and the energy spectrum was model fitted by the Gaussian function. The energy spectrum were shown in Figure 8.12, 8.13, and 8.14. From the fit, we obtained the counts rate (/day) of 29.19 keV, 42.43 keV, and 42.63 keV and calculated the count rate for lowest intensity line that is 29.39 keV. The results are summarized at Table 8.4 and we found that the total count rate per day of 42.43 keV was 544, it of 42.63 keV was 105, it of 29.19 keV was 97. The estimated counts rate per day of 29.39 keV was 9.

We simulated whether we could separate the 29.19 keV doublet if the energy resolution (FWHM) is 18 eV thinking the worst case. We used the two Gaussian functions with fixed the energy, branching ration $b_{29} = 1/13$, and the sigma $\sigma = 7.6$ eV. We assumed the lowest-energy of the ^{229}Th isomeric energy is 9.5 eV and 18.3 eV. First, we estimated how much counts we need to separate the 29.19 keV doublet. We generated spectra with the total counts of 3000, 4000 and, 5000 and fitted the generated spectra using a single Gaussian whose the sigma is fixed and the intensity and the energy are free. We found if we obtain the total count of 5000, we can separate the 29.19 keV doublet both the lowest-energy of the ^{229}Th isomeric state (Figure 8.15). Next, we estimated how much counts we need to obtain the statistical error of the lowest-energy of the ^{229}Th isomeric state below 0.5 eV. We used same analysis method in 3.2. We generated the 29.19 keV doublet spectra as mentioned earlier and fitted the spectra using two Gaussian functions whose energy and intensity were free. The statistical error was calculated using a contour of two energies and the contour was fitted with linear functions assuming $E(④ \to ⑤)_{\mathrm{max}} - E(④ \to ⑥)_{\mathrm{max}} = E(^{229\mathrm{m}}\mathrm{Th})$ and $E(④ \to ⑤)_{\mathrm{min}} - E(④ \to ⑥)_{\mathrm{min}} = E(^{229\mathrm{m}}\mathrm{Th})$. Figure 8.16 shows the contour and the fitted linear functions in the case of $E(^{229\mathrm{m}}\mathrm{Th})$ as to be 18.3 eV. We then calculated the statistical error with 1 σ both $E(^{229\mathrm{m}}\mathrm{Th}) = 9.5$ eV and $E(^{229\mathrm{m}}\mathrm{Th}) = 18.3$ eV with changing the total counts. From the results of this estimation (Figure 8.16right), we found in the case of $E(^{229\mathrm{m}}\mathrm{Th}) = 18.3$ eV, if we obtain the total counts of 30×10^3 which means 285 days observation, the statistical error can archive below 0.5 eV and in the case of $E(^{229\mathrm{m}}\mathrm{Th}) = 9.5$ eV, if we obtain the total counts of 45×10^3 which means 429 days observation, the statistical error can archive 1 eV. We need more than 10^5 counts to obtain the statistical error below 0.5 eV in the case of $E(^{229\mathrm{m}}\mathrm{Th}) = 9.5$ eV.

[*1] Calculated value using intensity
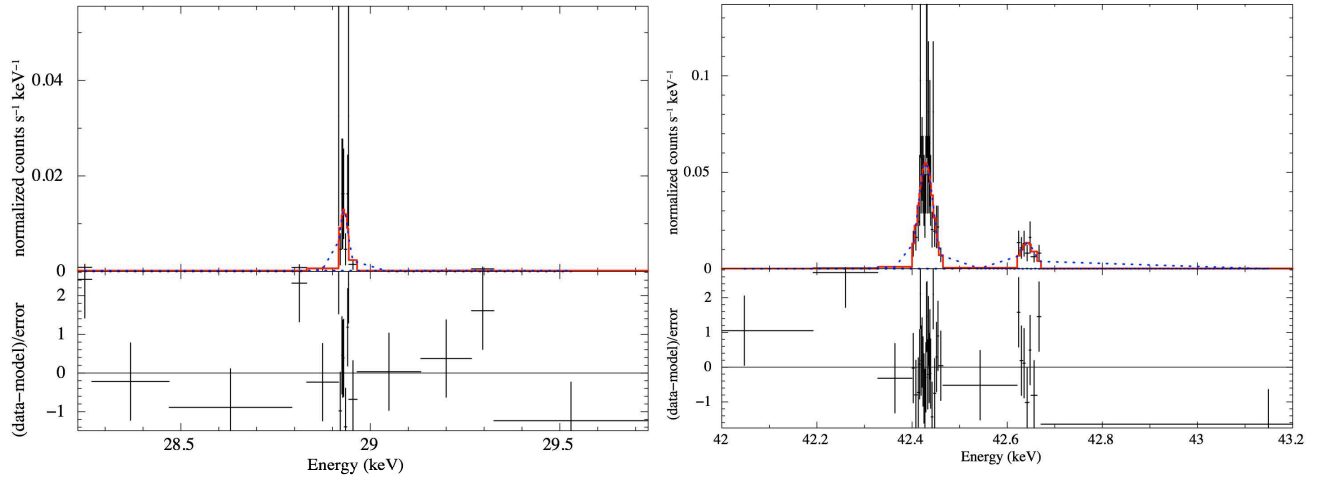
Fig. 8.12   Energy spectrum of channel 2 fitted by gaussian function: 29 keV doublet (left) and 42 keV doublet (right)
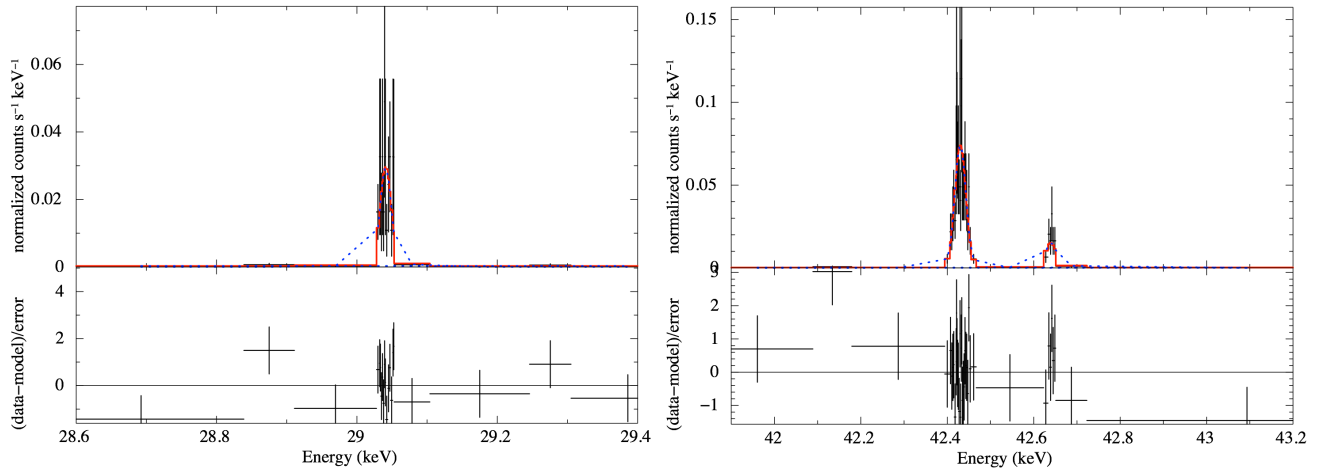
Fig. 8.13   Energy spectrum of channel 3 fitted by gaussian function: 29 keV doublet (left) and 42 keV doublet (right)
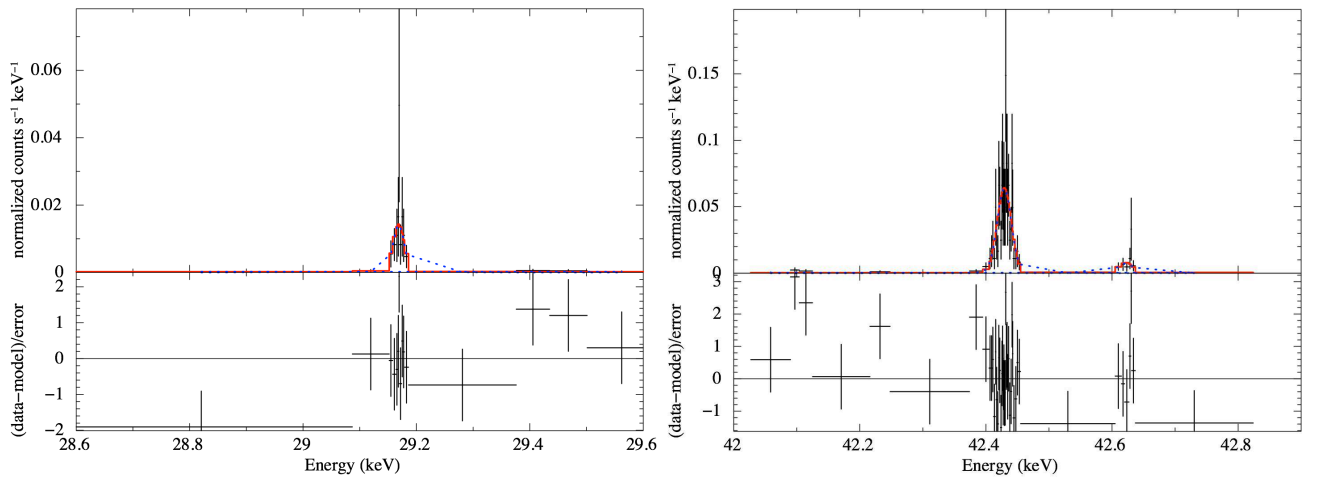
Fig. 8.14   Energy spectrum of channel 4 fitted by gaussian function: 29 keV doublet (left) and 42 keV doublet (right)
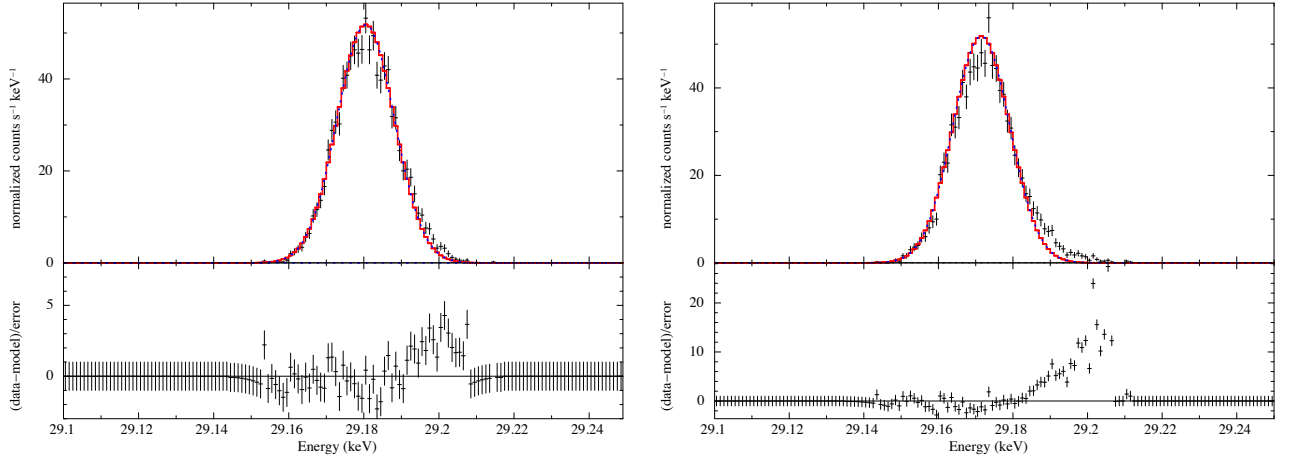
Fig. 8.15   Simulated data of 29.19 keV doublet with 5000 total counts and FWHM 18 eV: $E(^{229m}\text{Th})$ is 9.5 eV(left) and $E(^{229m}\text{Th})$ is 18.3 eV(right)
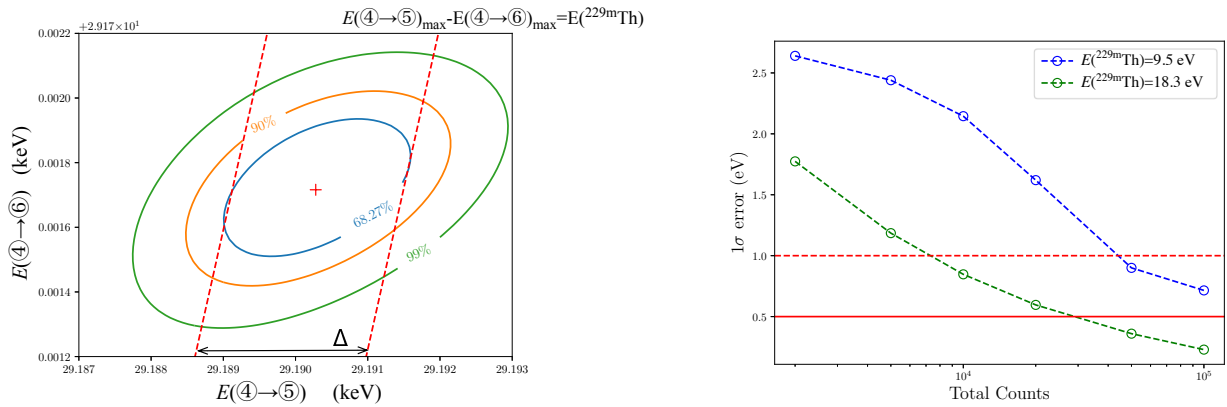
Fig. 8.16   Contour of 29.19 keV doublet whose $E(^{229m}\text{Th})$ is 18.3 eV and total counts are 5000 with the 18 eV energy resolution(left) and relation between total counts and statistical error (right)

Chapter 9

Conclusion

We have developed the TES microcalorimeters, the cryostage, and the new analysis method for measurement of the lowest-energy level of the ^{229}Th isomeric transition within 0.5 eV statistical error.

We carried out an experiment to find out energy scale calibration method when a TES microcalorimeter is operated in non-linear regime. We designed and fabricated a TES microcalorimeter array with a saturation energy of 7.5 keV, and irradiated with multiple monochromatic limes between 3.3 keV and 17.8 keV with three radio isotopes. Emission spectra from those radio isotopes (and from atoms) contain fine structures spreading 10 eV range. Because of the fine structure, a new method was necessary to correlate the pulse height (PHA) to the energy. We converted the line emission model in energy space to the PHA space assuming local linear relation $PHA = aE + b$ and performed the model fitted in the PHA space. From the fit we obtain a relation between PHA and E for a single E. Using multiple lines, we constructed PHA to E relation. After correcting for the nonlinearity we find the degradation of the energy resolution with energy: it is 16 eV at 13 keV while it was 5 eV at 6 keV. To fit the PHA spectrum within the fine structure, we reduced the nonlinear by converting the pulse events from the TES current to the TES resistance. This reduced the systematic errors of the $PHA - E$ conversion by 2 eV.

We designed and fabricated the new TES microcalorimeter with the sensitivity above 29 keV. The energy resolution of this device was 20 eV at 26 keV in our laboratory. We deployed the system in JAEA at Oarai to conduct an irradiation test with the ^{233}U source. We found degradation of the energy resolution to 40 eV due to increase low-frequency noise. We identified that the caused to be thermal fluctuation induced by γ-ray hits on the Si substrate of the device. In this experiment, the ^{133}Ba source and the ^{241}Am source were used as the calibration sources. We converted the TES current to the TES resistance and obtained the PHA, then the PHA was converted to the energy by the ten emission lines between 10 keV and 59 keV. We could not directly separate the doublet of 29.19 keV line because the energy resolution was not enough. We estimated the lowest energy level of the ^{229}Th isomeric state using energies of multiple lines in the decay chain and obtained $8.4^{+7.2}_{-5.8} \pm 9.5$ eV with the statistical and the systematic error.

Based on the results in Oarai experiment, we decided to install the collimator which blocks γ-rays to irradiate the Si substrate of the device. We also set the transition temperature lower to improve the energy resolution of the device. The new detector was deployed in Tohoku University. The energy resolution of all 3 pixels were $15 - 18$ eV at 26 keV when it is operated at 65 mK bath temperature. We confirmed reduction of the low frequency noise when the device was irradiated by the γ-ray of the ^{233}U source.

However, due to the trouble of the refrigerator, we could not continue to operate at 65 mK. We set the bath temperature to 90 mK, and decided to continue experiment to decide how we install calibration sources. We introduced new lines from Te, I, and Gd, spreading over 27 keV to 50 keV. We find out how to set and operate those calibration sources during the experiment. Finally, we simulated whether we can separate 29.19 keV into doublet with the 18 eV energy resolution. We found both $E(^{229m}\text{Th}) = 9.5$ eVand $E(^{229m}\text{Th}) = 18.3$ eV can be

separated if we obtain the total counts of 5000 which means 48 days observation. In addition to this, in the case of $E(^{229\mathrm{m}}\mathrm{Th}) = 18.3$ eV, the total counts of 30×10^3 that equal to 285 days observation are required to archive the statistical error below 0.5 eV and in the case of $E(^{229\mathrm{m}}\mathrm{Th}) = 9.5$ eV, the total counts of 45×10^3 that equal to 429 days observation are required.

A

Energy and uncertainty of calibration lines

The energy and uncertainty of calibration lines in Oarai campaign and in Tohoku campaign are summarized at Table A.1 and Table A.2.

Table A.1   Calibration $\gamma-$ and X- ray energy in Oarai campaign

Calibration line	Energy (eV)	uncertainties (eV)	Natural width (eV)
Th Lα_1[1]	12968.70	0.40	11.90
Th Lβ_1[1]	16202.00	0.20	12.40
Th Lγ_1[1]	18982.50	0.90	15.00
Ag Kβ_1[1,2]	24942.42	0.30	10.43
Ag Kβ_2[2]	25455.60	0.31	-
Am(26 keV)[1,2]	26344.8	0.2	-
Cs Kα_1[1,2]	30973.13	0.46	15.60
Cs Kα_2[1,2]	30625.40	0.45	15.80
Cs Kβ_1[2]	34987.3	1.0	17.79
Cs Kβ_2[2]	35821.7	3.1	-
Am(43 keV)[2]	43423	10	-
Am(59 keV) $-$ Au Lβ_1[2]	48098.8	0.5	8.50
Am(59 keV) $-$ Au Lβ_2[2]	47956.5	0.5	11.20
Am(59 keV) $-$ Au Lβ_3^2	47930.7	1.4	18.40
Am(59 keV) $-$ Au Lβ_5[2]	48336.4	0.5	20.70
Am(59 keV) $-$ Au Lα_1[1,2]	49827.8	0.4	8.60
Am(59 keV) $-$ Au Lα_2[1,2]	49913.1	0.4	7.61
Am(59 keV)[1,2]	59541.2	0.2	-

[1]Lines that were used in model fitting in PHA space [2]Lines that were used in model fitting in PI space at narrow range

Table A.2   Energy and uncertainty of added calibration lines in Tohoku campaign (reference are Handbook of X-ray data)

Calibration line	Energy (eV)	uncertainties (eV)	Natural width (eV)
Te Kα_2	27201.99	0.21	13.00
Te Kα_1	27472.57	0.27	12.80
I Kα_2	28317.00	0.67	13.80
I Kα_1	28612.00	0.49	13.70
Cs Kα_3	30270.5	1.3	15.42
Cs Kα_2	30625.00	0.45	15.80
Cs Kα_1	30973.13	0.46	15.60
Te Kβ_3	30944.60	0.46	12.30
Te Kβ_2	30995.97	0.34	13.30
Te Kβ_1	31700.76	0.72	-
I Kβ_3	32239.40	0.50	15.27
I Kβ_1	32294.70	0.50	15.69
I Kβ_2	33042.0	2.6	-
Cs Kβ_1	34987.3	1.0	17.79
Cs Kβ_2	35821.7	3.1	-
Cs Kβ_3	34919.68	0.58	16.89
Gd Kα_2	42308.90	0.43	26.70
Gd Kα_1	42996.20	0.44	26.40
Gd Kβ_3	48555.0	5.6	28.00
Gd Kβ_1	48697.0	5.7	29.37
Gd Kβ_2	49959.0	8.9	-

B

SQUID parameter

SQUID array amplifiers that we used in this study were designed in our laboratory [50] and fabricated in the Clean Room for Analog-digital superconductiVITY (CRAVITY) in National institute of Advanced Industrial Science and Technology (AIST).

Table B.1   Measured parameters of SQUID in Oarai campagin

Items		Values	Unit
Mutual inductance of feedback coil	M_{FB}	87.25	pH
Mutual inductance of input coil	M_{in}	100.87	pH
Feed back resistance	R_{FB}	100	kΩ
Resistance of shunt	R_{s}	3.90	mΩ

Bibliography

[1] E. Peik, B. Lipphardt, H. Schnatz, T. Schneider, Chr Tamm, and S. G. Karshenboim. Limit on the Present Temporal Variation of the Fine Structure Constant. *AIP Conference Proceedings*, 93, 2004.

[2] C. W. Reich and R. G. Helmer. Energy separation of the doublet of intrinsic states at the ground state of Th229. *Physical Review Letters*, 64(3):271–273, 1990.

[3] B R Beck, J A Becker, P Beiersdorfer, G V Brown, K J Moody, J B Wilhelmy, F S Porter, C A Kilbourne, and R L Kelley. Energy Splitting of the Ground-State Doublet in the Nucleus ^{229}Th. 142501(April):1–4, 2007.

[4] Justin Jeet, Christian Schneider, Scott T Sullivan, Wade G Rellergert, A Cassanho, H P Jenssen, Eugene V Tkalya, and Eric R Hudson. Results pf a dorect search using synchrotron radiation for the low-energy ^{229}Th nuclear isomeric transition. *arXiv*, pages 1–6, 2015.

[5] A. Yamaguchi, M. Kolbe, H. Kaser, T. Reichel, A. Gottwald, and E. Peik. Experimental search for the low-energy nuclear transition in ^{229}Th with undulator radiation. *New Journal of Physics*, 17(5):53053, 2015.

[6] Lars Von Der Wense, Benedict Seiferle, Mustapha Laatiaoui, Jürgen B. Neumayr, Hans Jörg Maier, Hans Friedrich Wirth, Christoph Mokry, Jörg Runke, Klaus Eberhardt, Christoph E. Düllmann, Norbert G. Trautmann, and Peter G. Thirolf. Direct detection of the ^{229} Th nuclear clock transition. *Nature*, (7601):47–51, 2016.

[7] Benedict Seiferle, Lars Von Der Wense, and Peter G Thirolf. Lifetime Measurement of the ^{229}Th Nuclear Isomer. *Physical Review Letters*, 118(042501):1–5, 2017.

[8] F Ponce. *High Accuracy Measurement of the Nuclear Decay of U-235m and Search for the Nuclear Decay of Th-229m*. PhD thesis, 2017.

[9] P.A.M.Dirac. A new basis for cosmology. *royal society pubishing*, pages 199–208, 1937.

[10] Edward Witten. STRING THEORY DYNAMICS IN VARIOUS DIMENSIONS. *arXiv*, 1995.

[11] A. I. Shlyakhter. Direct test of the constancy of fundamental nuclear constants. *Nature*, 264(5584):340, 1976.

[12] Thibault Damour and Freeman Dyson. The Oklo bound on the time variation of the fine-structure constant revisited. *Nuclear Physics B*, 480:37–54, 1996.

[13] Yasunori Fujii, Akira Iwamoto, Tokio Fukahori, Toshihiko Ohnuki, Masayuki Nakagawa, Hiroshi Hidaka, Yasuji Oura, and Peter Moller. The nuclear interaction at Oklo 2 billion years ago. *Nuclear Physics B*, pages 1–29, 2000.

[14] S. K. Lamoreaux and J. R. Torgerson. Neutron moderation in the Oklo natural reactor and the time variation of [Formula Presented]. *Physical Review D - Particles, Fields, Gravitation and Cosmology*, 69(12):1–5, 2004.

[15] Varshlovich D.A. Potekhin A.Y. Non-variability of the fine-structure constant over cosmological time scales. *Astronomy and Astrophysics*, 104:89–98, 1994.

[16] M. T. Murphy, J. K. Webb, V. V. Flambaum, V. A. Dzuba, C. W. Churchill, J. X. Prochaska, J. D. Barrow, and A. M. Wolfe. Possible evidence for a variable fine-structure constant from QSO absorption lines: Motivations, analysis and results. *Monthly Notices of the Royal Astronomical Society*, 327:1208–1222, 2001.

[17] M T Murphy, J K Webb, and V V Flambaum. Further evidence for a variable fine-structure constant from

Keck / HIRES QSO absorption spectra. *Monthly Notices of the Royal Astronomical Society*, 345:609–638, 2003.

[18] V A Dzuba, V V Flambaum, and J K Webb. Calculations of the relativistic effects in many-electron atoms and space-time variation of fundamental constants. *Phys. Rev. A*, 59(1):230–237, 1999.

[19] V. A. Dzuba, V. V. Flambaum, and M. V. Marchenko. Relativistic effects in Sr, Dy, Yb II, and Yb III and search for variation of the fine-structure constant. *Physical Review A - Atomic, Molecular, and Optical Physics*, 68:1–5, 2003.

[20] S. Bize, S. A. Diddams, U. Tanaka, C. E. Tanner, W. H. Oskay, R. E. Drullinger, T. E. Parker, T. P. Heavner, S. R. Jefferts, L. Hollberg, W. M. Itano, and J. C. Bergquist. Testing the Stability of Fundamental Constants with the [Formula presented] Single-Ion Optical Clock. *Physical Review Letters*, 90(15):4, 2003.

[21] M. Fischer, N. Kolachevsky, M. Zimmermann, R. Holzwarth, Th Udem, T. W. Hänsch, M. Abgrall, J. Grünert, I. Maksimovic, S. Bize, H. Marion, F. Pereira Dos Santos, P. Lemonde, G. Santarelli, P. Laurent, A. Clairon, C. Salomon, M. Haas, U. D. Jentschura, and C. H. Keitel. New Limits on the Drift of Fundamental Constants from Laboratory Measurements. *Physical Review Letters*, 92(23):1–4, 2004.

[22] S. Blatt, A. D. Ludlow, G. K. Campbell, J. W. Thomsen, T. Zelevinsky, M. M. Boyd, J. Ye, X. Baillard, M. Fouché, R. Le Targat, A. Brusch, P. Lemonde, M. Takamoto, F. L. Hong, H. Katori, and V. V. Flambaum. New limits on coupling of fundamental constants to gravity using Sr87 optical lattice clocks. *Physical Review Letters*, 100:1–4, 2008.

[23] Xiao Tao He and Zhong Zhou Ren. Enhanced sensitivity to variation of fundamental constants in the transitions of ^{229}Th and ^{249}Bk. *Journal of Physics G: Nuclear and Particle Physics*, 34:1611–1619, 2007.

[24] Xiao-tao He and Zhong-zhou Ren. Temporal variation of the fine structure constant and the strong interaction parameter in the ^{229} Th transition. *Nuclear Physics A*, 806:117–123, 2008.

[25] A. C. Hayes and J. L. Friar. Sensitivity of nuclear transition frequencies to temporal variation of the fine structure constant or the strong interaction. *Physics Letters, Section B: Nuclear, Elementary Particle and High-Energy Physics*, 650(4):229–232, 2007.

[26] Barci V, Ardisson G, B Weiss, O El Samad, De Nice, and F Nice Ce. Th from gamma-ray spectroscopy study of U233-particle decay. *Physical Review C - Nuclear Physics*, 68(034329), 2003.

[27] Laurent Ravera, Christophe Cara, María Teresa Ceballos, Xavier Barcons, Didier Barret, Rodolphe Clédassou, Antoine Clénet, Beatriz Cobo, Eric Doumayrou, Roland H den Hartog, Bert-Joost van Leeuwen, Dennis van Loon, José Miguel Mas-Hesse, Claude Pigot, and Etienne Pointecouteau. The DRE: the digital readout electronics for ATHENA X-IFU. In Tadayuki Takahashi, Jan-Willem A den Herder, and Mark Bautz, editors, *Proceedings of the SPIE*, pages 91445T–91445T–8. Observatoire Midi-Pyrénées, IRAP, CNRS, Univ. de Toulouse (France), SPIE, July 2014.

[28] B R Beck, C Y Wu, P Beiersdorfer, G V Brown, J A Becker, K J Moody, J B Wilhelmy, F S Porter, and R L Kelley. Improved Value for the Energy Splitting of the Ground-State Doublet in the Nucleus ^{229m}Th. *12th International Conference on Nuclear Reaction Mechanisms*, 2009.

[29] L. A. Kroger and C. W. Reich. Features of the low-energy level scheme of229Th as observed in the α-decay of233U. *Nuclear Physics, Section A*, 259(1):29–60, 1976.

[30] R.G Helmer and Reich C.W. An excited state of ^{229}Th at 3.5 eV. *Physical Review C*, 49(4):1845–1858, 1994.

[31] Z. O. Guimarães-Filho and O. Helene. Energy of the 3/2+ state of229Th reexamined. *Physical Review C - Nuclear Physics*, 71(4):1–4, 2005.

[32] Lars Swanberg Jr. Erik. *Searching for the Decay of ^{229m} Th*. PhD thesis, University of California, Berkeley, 2012.

[33] Francisco Ponse. *High Accuracy Measurement of the Nuclear Decay of U-235m and Search for the Nuclear Decay of Th-229m*. PhD thesis, University of California, 2017.

[34] S. J. Lee, J. S. Adams, S. R. Bandler, J. A. Chervenak, M. E. Eckart, F. M. Finkbeiner, R. L. Kelley, C. A. Kilbourne, F. S. Porter, J. E. Sadleir, S. J. Smith, and E. J. Wassell. Fine pitch transition-edge sensor X-ray microcalorimeters with sub-eV energy resolution at 1.5 keV. *Applied Physics Letters*, 107(22), 2015.

[35] S. R. Bandler, R.P. Brekosky, A.D. Brown, J.A. Chervenak, E. Figueroa-Feliciano, F.M. Finkbeiner, N. Iyomoto, R.L. Kelly, C A Kilbourne, F.S. Porter, J. Sadleir, and S.J. Smith. Performance of TES X-ray Microcalorimeters with a Novel Absorber Design. *Journal of Low Temperature Physics*, 151:400–405, 2008.

[36] D A Bennett, R D Horansky, D R Schmidt, A S Hoover, R Winkler, B K Alpert, J A Beall, W B Doriese, J W Fowler, C P Fitzgerald, G C Hilton, K D Irwin, V Kotsubo, J A B Mates, G C O'Neil, M W Rabin, C D Reintsema, F J Schima, D S Swetz, L R Vale, and J N Ullom. A high resolution gamma-ray spectrometer based on superconducting microcalorimeters. *Review of Scientific Instruments*, 83(093113):1–14, September 2012.

[37] R D Horansky, J N Ullom, J A Beall, W B Doriese, W D Duncan, L Ferreira, D M Tournear, D T Vo, and M W Rabin. Superconducting absorbers for use in ultra-high resolution gamma-ray spectrometers based on low temperature microcalorimeter arrays. *NUCLEAR INSTRUMENTS & METHODS IN PHYSICS RESEARCH SECTION A-ACCELERATORS SPECTROMETERS DETECTORS AND ASSOCIATED EQUIPMENT*, 579:169–172, 2007.

[38] John C.Mather. Bolometer noise: nonequilibrium theory. *Applied Optics*, pages 1125–1129, 1982.

[39] R.Clark Jones. The Ultimate Sensitivity of Radiation Detectors. *Journal of the Optical Society of America*, 37:879–890, 1947.

[40] D. McCammon. *Cryogenic Particle Detection.* Springer, 2005.

[41] K.D.Irwin and G.C.Hilton. *Cryogenic Particle Detection.* Springer, 2005.

[42] P.Debye. Zur Theorie der spezifischen Wärmen. *Annalen der Physik*, 344(14):789–839, 1912.

[43] Charles kittel. *Introduction to Solid State Physics, 7th ED.* Wiley, 1996.

[44] K. D. Irwin. An application of electrothermal feedback for high resolution cryogenic particle detection. *Applied Physics Letters*, 66(1):1998–2000, April 1995.

[45] A E Szymkowiak, R L Kelley, S H Moseley, and C K Stahle. Signal processing for microcalorimeters. *Journal of Low Temperature Physics*, 93(3):281–285, November 1993.

[46] Moseley S H, Mather J. C., and McCammon D. Thermal detectors as x-ray spectrometers. *Journal of Applied Physics*, 56(5):1257–1262, 1984.

[47] D J Fixsen, S H Moseley, B Cabrera, and E Figueroa-Feliciano. Pulse estimation in nonlinear detectors with nonstationary noise. *NUCLEAR INSTRUMENTS & METHODS IN PHYSICS RESEARCH SECTION A-ACCELERATORS SPECTROMETERS DETECTORS AND ASSOCIATED EQUIPMENT*, 520:555–558, 2004.

[48] S.R Bandler, E Figueroa-Feliciano, C.K Stahle, K Boyce, R Brekosky, J Chervenak, F Finkbeiner, R Kelley, M Lindeman, F.S Porter, and T Saab. Design of transition edge sensor microcalorimeters for optimal performance. *Nuclear Instruments and Methods in Physics Research Section A: Accelerators, Spectrometers, Detectors and Associated Equipment*, 520(1-3):285–288, 2004.

[49] John Clarke and Alex I. Braginski, editors. *The SQUID Handbook: Fundamentals and Technology of SQUIDs and SQUID Systems.* Wiley-VCH, 1 edition, August 2004.

[50] Kazuhiro Sakai. *A Frequency-Division Multiplexing Readout System for Large-Format TES X-ray Microcalorimeter Arrays towards Future Space Missions.* PhD thesis, University of Tokyo, 2014.

[51] Haruka Muramatsu, Tasuku Hayashi, Keisei Maehisa, Yuki Nakashima, Kazuhisa Mitsuda, Noriko Y. Yamasaki, Toru Hara, and Keisuke Maehata. A Study of X-Ray Response of the TES X-Ray Microcalorimeter for STEM. *IEEE Transactions on Applied Superconductivity*, 27(4), 2017.

[52] Haruka Muramatsu, K. Nagayoshi, T. Hayashi, K. Sakai, R. Yamamoto, K. Mitsuda, N.Y. Yamasaki, K. Mae-

hata, and T. Hara. Design and Performance of a TES X-ray Microcalorimeter Array for Energy Dispersive Spectroscopy on Scanning Transmission Electron Microscope. *Journal of Low Temperature Physics*, pages 1–8.

[53] Tasuku Hayashi. *A Development of a High-Energy-Resolution X-ray Spectrometer System Towards Microanalysis of Astromaterials.* PhD thesis, University of Tokyo, 2018.

[54] Günter Zschornak. *Handbook of X-Ray Data.* Springer, 2007.